SFERA

Proposal for a Spherical Gravitational Wave Detector

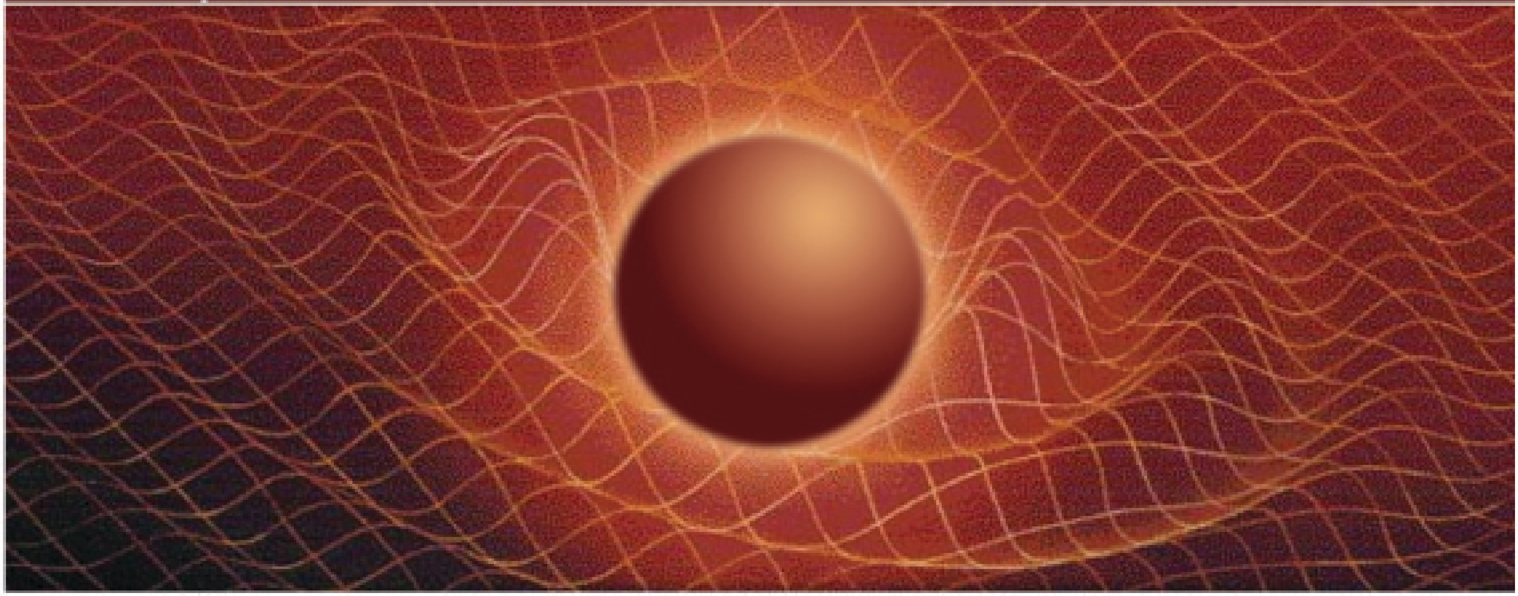

INFN
(Frascati, Genova, L'Aquila, Roma, Roma 2)

University of Geneva

University of Leiden

SEPTEMBER 2005

LABORATORI NAZIONALI DI FRASCATI
SIS – Pubblicazioni

LNF–06/ 08 (IR)
28 Febbraio 2006

SFERA
Proposal for a Spherical Gravitational Wave Detector

INFN – Frascati, Genova, L'Aquila, Roma, Roma2

University of Genova

University of Lieden

September 2005

Contents

1 Introduction **2**

2 Resonant spherical detectors: theory **7**
- 2.1 The normal modes of the sphere 7
- 2.2 The interaction of the normal modes with GWs 11
- 2.3 The spherical components of h_{ij} 13
- 2.4 The quadrupolar modes and signal reconstruction 14
- 2.5 Resonant transducers and the TIGA configuration 16
- 2.6 Properties of resonant spherical detectors: a summary 17

3 Experimental results **24**
- 3.1 Introduction 24
- 3.2 TIGA experiments 25
- 3.3 Ultra-low temperature experiments 25
- 3.4 MiniGRAIL 27

4 The SFERA detector **31**
- 4.1 Specification of the detector 31
- 4.2 Noises 32
- 4.3 Cosmic rays 32
- 4.4 Cryogenics for SFERA 36
- 4.5 Read-out 41
- 4.6 Data Acquisition System 56
- 4.7 Expected sensitivity 59

5 Astrophysics with a spherical gravitational wave detector **61**
- 5.1 Burst sources 61
- 5.2 Periodic sources 66
- 5.3 Stochastic backgrounds 69

6 Project Costs **72**

7 Schedule **73**

8 The collaboration **74**

A The TIGA configuration **75**

B Equations of motion **79**

1 Introduction

Physical motivations

The direct detection of gravitational waves (GWs) is one of the great challenges of contemporary experimental physics. Its aim is to open up a new window on the Universe, in astrophysics as well as in cosmology and in fundamental physics. Each time physicists have probed Nature with new tools, whether building accelerators reaching higher and higher energies, or exploring the sky using x- or γ-rays telescopes, new and often unexpected phenomena have been discovered. Gravitational waves are a potentially unique probe, which can carry fundamental informations, inaccessible by electromagnetic or other means. This can be traced to the following basic facts:

- In astrophysics, potentially detectable GWs carry informations on the bulk, coherent motion of large masses. By contrast, the electromagnetic waves observed in astrophysics are typically generated by the incoherent superposition of many emitters. Furthermore, due to their very small cross section, GWs carry direct informations on regions, such as the interior of neutron stars, that are opaque to electromagnetic radiation, "revealing features of their source which no one could ever learn by electromagnetic, cosmic ray, or neutrino studies" [1].

  In particular, GWs are a unique probe of compact objects such as neutron stars (NS) and black holes (BH). Their study, beside an evident astrophysical interest, has also a great potential importance from the point of view of "fundamental" physics. For example, the study of the interior of neutron stars can reveal important properties of quantum chromodynamics (QCD) at high density, while the detection of GWs produced in the coalescence of a BH-BH system can allow us to make unique explorations of gravity in a strong-field regime.

- In cosmology, their importance is due to the fact that, because of their very small cross-section, GWs decouple from the primordial plasma already at temperatures below the Planck scales, i.e. for $kT < 10^{19}$ GeV. This temperature is reached 10^{-43} sec after the Big Bang. This means that any stochastic background of GWs produced at a time $t > 10^{-43}$ sec after the Big Bang reaches us today without having suffered any modification in its spectral features (apart from the redshift due to the expansion of the Universe) and therefore carries a genuine "snapshot" of the Universe at the time of production. By contrast, the cosmic microwave background (CMB) is a snapshot of the Universe at the time when the electromagnetic waves decoupled from the primordial plasma, i.e. at about 300 000 yr after the Big Bang.

For this reason, the detection of a stochastic background of GWs of cosmological origin would carry extraordinary informations on early Universe cosmology, and therefore on physics at correspondingly high energies, which would be impossible to obtain by any other means (see Ref. [2] for review).

The experimental situation

Resonant-mass detectors have behind 40 years of work and development and have reached a duty cycle near 100%. They are now in the continuous observational mode with a burst sensitivity $h = 2 \times 10^{-19}$ or spectral amplitude of $\tilde{h} = 10^{-21}\mathrm{Hz}^{-1/2}$ in a bandwidth of tens of Hertz [3]. Such a sensitivity should allow the detection of the strongest sources in our Galaxy and in the Local group. The underlying non-gravitational physics associated with these detectors is understood and further improvements appear based on solid technological guidelines. *Resonant bars are reliable instruments.*

On the other hand, the large scale interferometer LIGO has almost reached its target sensitivity, while VIRGO is expected to reach it in the near future. In this context, we believe that resonant-mass experiments can remain at the forefront of gravitational-wave research if they are able to improve substantially their sensitivity so that, at least in some frequency range, they will be competitive with large-scale interferometers, while at the same time offering complementary features. As we will discuss in this proposal, this can be obtained in the classical scheme of a main resonator coupled to a secondary smaller resonant mass, by a combination of two factors: (1) the improvement in the readout system, and (2) building a spherical resonant-mass detector.

Concerning point (1), the successful cooldown [4] and the operation of NAUTILUS [5] at 0.1 K [6] and of AURIGA [7] at 0.2 K [8] demonstrates that thermal noise can be reduced to a level where it is no longer a dominant source of noise, and the main limitation of resonant detectors will be due to the noise temperature of the electronics. Efforts to improve the readout system, essential to bring us closer to the quantum limit (i.e. to the detection of a change in the vibrational status corresponding to a single phonon) are under way. The best performances obtained up to now in a double-SQUID system coupled with a resonant circuit give an energy resolution of $120\hbar$ [9], and even better noise figures, of the order of $20\hbar$ have been recently approached [10].

Concerning point (2), a spherical resonant-mass detector has a number of inherent properties that give it advantages over other types of detectors. In particular:

- Present resonant bars are thin cylinders, with a length $L \simeq 3$ m and a diameter $d \simeq 30$ cm. A sphere has the same frequency of a cylinder of the same material, if its diameter $2R$ is equal to the length L of the cylinder (apart from a numerical factor very close to one). However, such a sphere is much more massive than the corresponding thin cylinder, and therefore its cross-section for absorption of gravitational waves is much larger.

- A sphere is an omni-directional detector, since its sensitivity is the same independently of the direction of arrival of the wave. By contrast, cylindrical bars (and also interferometers) have an optimal sensitivity along some direction, and reduced sensitivity along the other directions (as well as blind directions).

As a consequence, the cross-section of a resonant sphere for absorption of GWs, compared to the cross-section of a bar with the same resonant frequency is larger by a factor $\simeq 18$ (for a resonance frequency $f \simeq 1$ kHz), for waves that hit the bar from optimal directions and with optimal polarization. Comparing instead the cross-sections averaged over the solid angle and polarization, this enhancement factor becomes $\simeq 67$, leading to a significant improvement in sensitivity. Combining this geometrical improvement factor with the improvement in the readout mentioned above, we will see that a resonant sfere with a radius $R = 1$ m can reach a sensitivity, in a bandwidth $\Delta f \sim 200$ Hz centered around a resonant frequency $f \simeq 1$ kHz, better than that of the first-generation of large-scale interferometers, and not far from the sensitivity projected for second-generation interferometers such as advanced LIGO and advanced VIRGO.

At the same time, a resonant sphere offers a number of remarkable features, that makes it an ideal complement to an interferometric detector. In fact, as we will discuss in more detail in the next section:

- A resonant bar has a single sensitive output, which is the oscillation amplitude of its fundamental longitudinal elastic mode. Similarly an interferometer has only one sensitive output, its differential mode. As a result, if a detector such as an interferometer or a bar is hit by a GW with amplitudes h_+ and $h_\times$ (where + and × label the two possible polarizations of a GW), coming from a direction given by polar angles θ, ϕ, from the single output of the detector we can read the combination

  $$h_+ F_+(\theta, \phi) + h_\times F_\times(\theta, \phi)\,, \tag{1}$$

  where $F_{+,\times}(\theta, \phi)$ are functions which depend on the detector geometry. From this single information we cannot disantangle, with a single bar or a single interferometer, the values of h_+, $h_\times$, θ and ϕ.

  By contrast, the normal modes of a sphere are identified, among other indices (see below) by the indices (l, m) that label the corresponding spherical harmonics. GWs interact with five quadrupolar modes with $l = 2$ and $m = -2, \ldots, +2$, which are degenerate (apart from small effects due to the suspension mechanisms that lift the degeneracy). Therefore a resonant sphere has five outputs. From this information, it is possible to read out separately the four quantities h_+, $h_\times$, θ and ϕ, so we measure separately the amplitudes of the two polarizations, as well as the direction of arrival of the wave.

- A fifth information contained in the five output channels is a veto that distinguishes a true GW signal from a spurious excitation due to noise, checking the transverse nature of the disturbances. This is of great importance, since all GW detectors, whether resonant masses or interferometers, are affected by many non-gaussian disturbances that simulate GW signals.

- If we include in our analysis the presence of noise, then the ability to reconstruct the arrival direction will depend on the signal-to-noise ratio. If we denote by SNR the signal-to-noise ratio in energy, it can be shown that the error made on the determination of the arrival direction is

  $$\Delta\Omega = \frac{2}{\mathrm{SNR}}\,, \tag{2}$$

  where $\Delta\Omega \equiv \left[(\Delta\theta)^2 + \sin^2\theta(\Delta\phi)^2\right]$. It can be shown that this resolution, which is obtained from a *single* spherical resonant-mass detector, is better than what can be achieved, with the same SNR, combining the outputs of *three* interferometers.

  From this we see that interferometers and resonant spheres are really complementary: interferometers, due to their larger bandwidth, are much better at reconstructing the waveform, while a sphere is much better at reconstructing the arrival direction. *Together, an interferometer and a sphere would be much more effective for opening up the field of GW astronomy.*

  Beside, the separate information that the sphere gives on h_+ and $h_\times$ can be very important for reconstructing the parameters of the source.

- As with resonant bars, the vibration modes of the sphere will be monitored and amplified by means of resonant transducers. For a sphere, monitoring the five quadrupole modes therefore requires at least five resonant transducers. However, a configuration of transducers which is expecially simple for deconvolving the output, the so-called TIGA configuration, includes a sixth transducer, and from the combined output of these six channels we can also monitor a possible scalar wave. In the standard theory of general relativity, GWs do not excite the quadrupolar mode with $m = 0$ and therefore we have a further veto that distinguishes spurious noises from real GWs. However, this mode is excited by scalar fields, as one typically has in scalar-tensor extensions of general relativity, and therefore one has the possibility of testing such theories. More generally, in a resonant sphere a field with spin s couples only to the modes labeled by (l, m), with $l = s$. Therefore a resonant sphere measures directly the spin content of the field by which it has been excited.

- Finally, we will see below that the overall cost of a spherical resonant-mass detector with a diameter of 2 meters, working at a resonance frequency of about 1 kHz, is a small fraction, of the order of a few per cent, of the cost of a large scale interferometer of first generation, and the natural and technologically straightforward extension of the techniques on which our collaboration has developed a unique know-out over the course of several decades.

These points will be elaborated below. In this proposal we first describe the main features of spherical detectors along with their advantages with respect to the present bar antennas and the interferometers, the target gravitational wave sources and the state of the art in the field of resonant-mass detectors.

In the second part of this proposal we describe the program necessary to realize a spherical detector, 33 tons of mass, competitive with large interferometers but with complementary features.

2 Resonant spherical detectors: theory

The response of a spherical resonant-mass detector to GWs has been studied in detail in the literature, and all theoretical aspects are very well understood. The advantages of a resonant sphere in terms of cross-section and its multi-mode capability were already realized in the 1970s, see Refs. [11, 12, 13]. More recent detailed discussions of the response of spherical resonant-mass detectors can be found in Refs. [14]–[20]. In this section we discuss some of the most relevant results, following the forthcoming textbook [21]. In Section 2.6 we provide a summary of the main results relevants for this proposal.

2.1 The normal modes of the sphere

Just as with resonant bars, the starting point for discussing the response of a sphere to an external force, such as that due to GWs, is the standard theory of elasticity. We consider an infinitesimal volume element of the elastic body, located at the position $\mathbf{x}$. Under the action of an external force, like that exerted by a GW, it will be displaced to a new position $\mathbf{x} + \mathbf{u}(\mathbf{x}, t)$. Within elasticity theory the equation governing the dynamics of $\mathbf{u}(\mathbf{x}, t)$ is

$$\rho \frac{\partial^2 u_i}{\partial t^2} = \frac{\partial \sigma_{ij}}{\partial x^j} + f_i \,, \tag{3}$$

where ρ is the density of the material, $\boldsymbol{f}$ is the force per unit volume acting on the elastic body, and σ_{ij} is the stress tensor. For homogeneous and isotropic media

$$\sigma_{ij} = \lambda(\boldsymbol{\nabla}\cdot\mathbf{u})\delta_{ij} + 2\mu\,\boldsymbol{\nabla}_i u_j \,, \tag{4}$$

where λ and μ are known as the Lamé coefficients. The equation of motion (3) then becomes

$$\rho \frac{\partial^2 \mathbf{u}}{\partial t^2} = (\lambda + \mu)\boldsymbol{\nabla}(\boldsymbol{\nabla} \cdot \mathbf{u}) + \mu \nabla^2 \mathbf{u} + \boldsymbol{f} \,. \tag{5}$$

The boundary condition (in the absence of external tractions on the surface of the body) is that, on the surface, $\sigma_{ij} n_j = 0$, where $\hat{\mathbf{n}}$ is the unit normal to the surface of the elastic body.

An elastic body is characterized by a set of normal modes $\boldsymbol{\psi}_N(\mathbf{x})$, where N denotes collectively all the indices that label them. The normal modes are found setting the external force $\boldsymbol{f} = 0$ in eq. (5) and searching for a solution of the form

$$\mathbf{u}(\mathbf{x}, t) = \boldsymbol{\psi}(\mathbf{x}) e^{-i\omega t} + c.c. \tag{6}$$

Imposing the boundary condition fixes the allowed solutions, labeled by N, and the corresponding values of the frequencies ω_N. Since the normal modes form a complete set, the most general displacement $\mathbf{u}(\mathbf{x}\,,t)$ can then be expanded as

$$\mathbf{u}(\mathbf{x}\,,t)=\sum_N \xi_N(t)\boldsymbol{\psi}_N(\mathbf{x}\,)\,. \tag{7}$$

The functions $\xi_N(t)$ are the oscillation amplitudes of the N-th mode.

The explicit computation of the normal modes $\boldsymbol{\psi}_N(\mathbf{x})$ for an elastic sphere is a classic textbook exercise in the theory of elasticity. The result is that there are two families of normal modes, called spheroidal and toroidal, respectively. To write them in a compact form, it is useful to introduce the spherical Bessel function $j_l(z)$ and to define the functions

$$\beta_0(z)\equiv\frac{j_l(z)}{z^2}\,,\quad \beta_1(z)\equiv\frac{d}{dz}\left(\frac{j_l(z)}{z}\right)\,,\quad \beta_2(z)\equiv\frac{d^2}{dz^2}j_l(z)\,, \tag{8}$$

$$\begin{aligned}\beta_3(z) &= \frac{1}{2}[\beta_2(z)+(l-1)(l+2)\beta_0(z)]\,, &(9)\\ \beta_4(z) &= \beta_2(z)-\frac{\lambda}{2\mu}z^2\beta_0(z)\,. &(10)\end{aligned}$$

The spheroidal and toroidal modes are then described as follows.

Spheroidal modes.

These modes are labeled as $\boldsymbol{\psi}^S_{nlm}(\mathbf{x}\,)$, where the label S stands for spheroidal, while l,m are the usual indices of the spherical harmonics, with $l\geq 0$ and $m=-l,\ldots,+l$, integers, and $n\geq 1$ is an integer that labels the higher harmonics with a given l,m, i.e. with a given angular dependence. The frequency associated to $\boldsymbol{\psi}^S_{nlm}(\mathbf{x}\,)$ is given by

$$\omega^S_{nl}=(\mu/\rho)^{1/2}\,k^S_{nl}\,, \tag{11}$$

where, as above, μ is a Lamé coefficient and ρ is the density of the material, while k^S_{nl} is the solution of an eigenvalue equation,

$$\beta_3(kR)\beta_4(qR)-l(l+1)\beta_1(kR)\beta_1(qR)=0\,, \tag{12}$$

where q is related to k by $q^2/k^2=\mu/(\lambda+2\mu)$, and R is the radius of the sphere. For each l this equation has an infinity of solutions, that we label by the index $n=1,2,\ldots$, and we denote by k^S_{nl}. Equation (12) however does not depend on m, so there is a $(2l+1)$-fold degeneracy. This equation is straightforward to solve numerically. In Table 1 we give the lowest n values computed for $l=0$ and for $l=2$, for a value of $\lambda/(2\mu)=1.05$, typical of the materials in which we are interested.

The explicit form of the spheroidal modes with $l\neq 0$ is

$$\boldsymbol{\psi}^S_{nlm}(r,\theta,\phi)=[a_{nl}(r)\hat{\mathbf{r}}+b_{nl}(r)R\boldsymbol{\nabla}]\,Y_{lm}(\theta,\phi)\,, \tag{13}$$

l	n	$(kR)^S$	l	n	$(kR)^S$
0	1	5.579950	2	1	2.650650
	2	12.39403		2	5.110612
	3	18.87013		3	8.639054
	4	24.28610		4	11.10026

Table 1: The values of k^S_{nl} for $l = 0$ and $l = 2$ and $n = 1, \dots 4$, taking $\lambda/(2\mu) = 1.05$. In a real detector, these values change by O(10%) because of the effect of the suspension system.

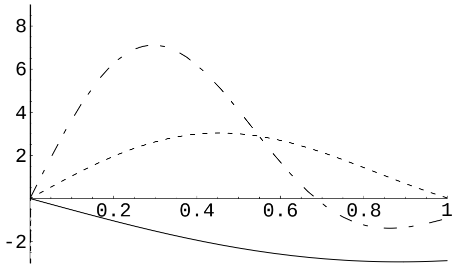

Figure 1: The function $a_{nl}(r)$, for $l = 2$ and $n = 1$ (solid line), $n = 2$ (dashed line), and $n = 3$ (dot-dashed), plotted against r/R, for $\lambda/(2\mu) = 1.05$. The functions $a_{nl}(r)$ are normalized according to eq. (16).

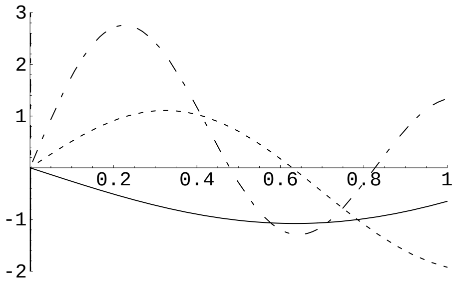

Figure 2: The same as Fig. 1, for the functions $b_{nl}(r)$.

where

$$\begin{aligned} a_{nl}(r) &= c_{nl}\left[\alpha_{nl}\frac{dj_l(z)}{dz}|_{z=q^S_{nl}r} - \beta_{nl}\; l(l+1)\frac{j_l(z)}{z}|_{z=k^S_{nl}r}\right], \\ b_{nl}(r) &= c_{nl}\,\frac{r}{R}\,\left[\alpha_{nl}\frac{j_l(z)}{z}|_{z=q^S_{nl}r} - \beta_{nl}\left(\frac{j_l(z)}{z} + \frac{dj_l(z)}{dz}\right)|_{z=k^S_{nl}r}\right]. \end{aligned} \qquad (14)$$

The constants α_{nl} and β_{nl} are given by

$$\alpha_{nl} = \beta_3(k^S_{nl}R)\,, \qquad \beta_{nl} = \frac{q}{k}\beta_1(q^S_{nl}R)\,. \qquad (15)$$

The constants c_{nl} are normalization factors, which are usually fixed requiring

$$\int_V d^3x\,\rho\,(\boldsymbol{\psi}^S_{nlm})^* \cdot \boldsymbol{\psi}^S_{nlm} = M\,, \qquad (16)$$

where M is the mass of the sphere and V its volume.

Despite the apparent intricacy of the analytic expressions, once the wavenumbers k^S_{nl} have been computed numerically, the radial functions $a_{nl}(r)$ and $b_{nl}(r)$ are obtained straightforwardly. In Figs. 1 and 2 we plot them for $l = 2$ and $n = 1, 2, 3$.

For $l = 0$, instead, the allowed values of k are the solution of the equation

$$\beta_4(qR) = 0\,, \qquad (17)$$

where again $q^2/k^2 = \mu/(\lambda + 2\mu)$, and the spheroidal modes are given by

$$\boldsymbol{\psi}^S_{n00}(r, \theta, \phi) = a_{n0}(r)\hat{\mathbf{r}}\,, \qquad a_{n0}(r) = c_{n0}\frac{dj_0}{dz}|_{z=q^S_{n0}r}\,. \qquad (18)$$

Therefore the spheroidal modes with $l = 0$ are purely radial.

The deformation of the five spheroidal modes with $l = 2$ and $n = 1$ is shown in Fig. 3. As we will see below, these modes are the most interesting for GW detection, and we will often loosely refer to them as “the” quadrupolar modes of the sphere.

Toroidal modes.

These modes are purely transverse and exist only for $l \geq 1$. The eigenvalues k^T_{nl} are determined by the equation $\beta_1(kR) = 0$ and the modes themselves have the form

$$\boldsymbol{\psi}^T_{nlm}(r, \theta, \phi) = c'_{nl}\, j_l(k^T_{nl}r)\, \mathbf{r} \times \boldsymbol{\nabla} Y_{lm}\,, \qquad (19)$$

with c'_{nl} the normalization constant. Observe that $\mathbf{r} \times \boldsymbol{\nabla} Y_{lm}$ is orthogonal both to $Y_{lm}\hat{\mathbf{r}}$ and to $\boldsymbol{\nabla} Y_{lm}$, i.e. to the displacements due to the spheroidal modes.

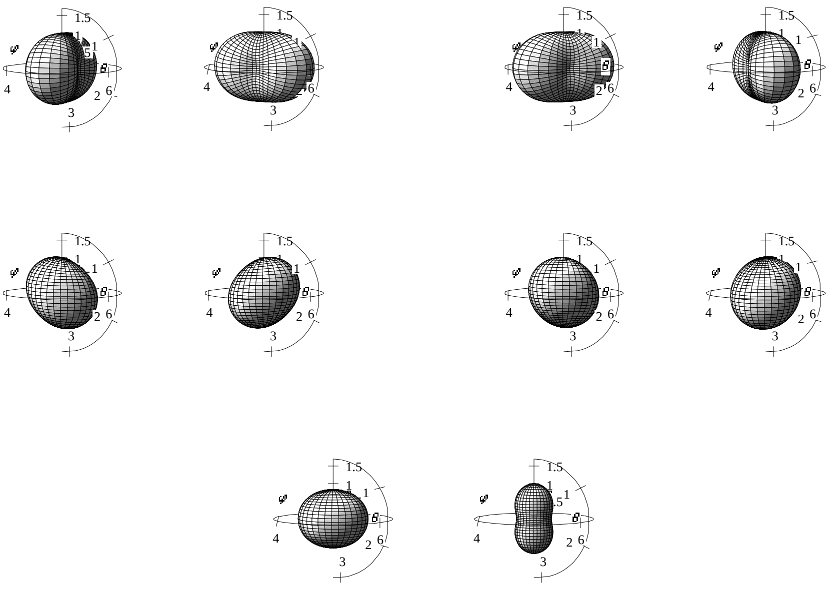

Figure 3: The deformations of the 5 quadrupole modes of a sphere (more precisely, the five spheroidal modes with $l = 2$ and $n = 1$) Two deformations, differing by half a period, are shown for each mode.

2.2 The interaction of the normal modes with GWs

The time evolution of the amplitudes $\xi_N(t)$ under the action of an external force $\boldsymbol{f}$ is found inserting the expansion of the displacement $\mathbf{u}(\mathbf{x}\,, t)$ in terms of normal modes, eq. (7), into the equation of motion eq. (5) and using the orthogonality relation (16). This gives

$$\ddot{\xi}_N + \omega_N^2 \xi_N = \frac{1}{M} \int d^3x\, \boldsymbol{f} \cdot \boldsymbol{\psi}_N^* \,, \tag{20}$$

or, if we include also the dissipation term,

$$\ddot{\xi}_N + \gamma_N \dot{\xi}_N + \omega_N^2 \xi_N = \frac{1}{M} \int d^3x\, \boldsymbol{f} \cdot \boldsymbol{\psi}_N^* \,, \tag{21}$$

where γ_N describes the dissipation in the N-th mode.

Let us recall, from standard textbooks on general relativity, that in a flat background a GW is a small perturbation of the flat-space metric, $g_{\mu\nu} = \eta_{\mu\nu} + h_{\mu\nu}$. Using the diffeomorfism invariance of general relativity, it is possible to choose a gauge, the so-called transverse-traceless gauge or TT-gauge, where $h_{0\mu} = 0$ and only the spatial components h_{ij} are non-vanishing. Furthermore, h_{ij} is transverse, $\partial_j h_{ij} = 0$, and traceless, $h_{ii} = 0$ (and of course symmetric, since $g_{\mu\nu}$ is symmetric). For a GW propagating in the direction $\hat{\mathbf{n}}$ the transversality condition translates into $n^i h_{ij} = 0$. If for definiteness we consider a wave propagating along $\hat{\mathbf{z}}$, the most general form of a GW is therefore

$$h_{ij} = \begin{pmatrix} h_+ & h_\times & 0 \\ h_\times & -h_+ & 0 \\ 0 & 0 & 0 \end{pmatrix}_{ij} \tag{22}$$

Again from standard textbooks (see e.g. Ref. [22]) we recall that, as long as the reduced wavelength $\lambdabar = \lambda/(2\pi)$ of the gravitational wave is much larger than the size of the detector, the interaction of the GW with the detector can be described in terms of a Newtonian force, without making further reference to any general relativistic concept. More precisely, from the equation of the geodesic deviation one finds that the force exerted by GWs on a unit volume of the detector, located at the position x^i (measured from the detector center-of-mass), is given by

$$f_i = \frac{\rho}{2}\ddot{h}_{ij}x^j\,, \tag{23}$$

where h_{ij} is the GW metric in the TT gauge and ρ is the density of the material. As we will see below, a resonant mass detector of diameter 2 meters has a frequency $f = O(1)$ kHz, so the reduced wavelength is $\lambdabar = c/f = O(50)$ km, which is much larger than the size of the detector. The Newtonian approximation is therefore excellent. Plugging eq. (23) into eq. (21) (and taking ρ constant) we get

$$\ddot{\xi}_N + \gamma_N\dot{\xi}_N + \omega_N^2\xi_N = \frac{1}{2V}\ddot{h}_{ij}\int_V d^3x\,(\boldsymbol{\psi}_N^*)^i x^j\,. \tag{24}$$

This is the basic equation that governs the response to a GW of the oscillation amplitudes $\xi_N(t)$ of the normal mode $\boldsymbol{\psi}_N$. Inserting the explicit expression of the modes $\boldsymbol{\psi}_N(\mathbf{x})$ discussed in the previous section and carrying out the integral in eq. (24), one finds the following results.

- For the toroidal modes $\boldsymbol{\psi}^T_{nlm}$, the integral vanishes for all values of n, l, m. Therefore toroidal modes do not couple to GWs. This means that monitoring them provides in principle a veto that distinguishes a true GW from a noise.

- The spheroidal modes $\boldsymbol{\psi}^S_{nlm}$ couple to GW only if $l = 2$. All other modes provide again a veto.

From now on we therefore concentrate on the spheroidal modes with $l = 2$. To simplify the notation, we denote the corresponding amplitude $\xi^S_{n,l=2,m}(t)$ just by $\xi_{nm}(t)$. The interaction of GWs with the $l = 2$ spheroidal modes can be described in a very simple way writing the tensor h_{ij} in terms of its *spherical components* h_m, that we introduce in the next subsection.

2.3 The spherical components of h_{ij}

In order to appreciate all the information that can be extracted from a resonant sphere, it is very convenient to think in terms of the spherical components of the metric tensor h_{ij}. In this section we therefore very briefly recall the notion of spherical components of a tensor.

We consider a traceless symmetric tensor with two spatial indices, that we denote generically by $Q_{ij}(\mathbf{x})$. Such a tensor has five independent components (in a mathematical language, it is a spin-2 tensor representation of the rotation group, and $5 = 2j + 1$ with $j = 2$). These five components can be rewritten in terms of objects related to the five spherical harmonics Y_{lm} with $l = 2$ observing that, if $\hat{x}$ is the unit vector in the radial direction, $Q_{ij}(\mathbf{x})\hat{x}^i\hat{x}^j$ is a scalar and theferore can be expanded in spherical harmonics,

$$Q_{ij}(\mathbf{x})\hat{x}^i\hat{x}^j = \sum_{l=0}^{\infty} \sum_{m=-l}^{l} q_{lm}(r) Y_{lm}(\theta, \phi)\,, \tag{25}$$

where q_{lm} are the coefficients of the expansion. However, from the fact that Q_{ij} is traceless and symmetric (i.e., is a spin-2 operator) it follows that in the above expansion only the term $l = 2$ contributes, so we really have

$$Q_{ij}(\mathbf{x})\hat{x}^i\hat{x}^j = \sum_{m=-2}^{2} Q_m(r) Y_{2m}(\theta, \phi)\,, \tag{26}$$

where $Q_m \equiv q_{2m}$. The five independent components of Q_{ij} can therefore be expressed in terms of the five quantities Q_m, with $m = -2, \ldots, 2$, which are called the spherical components of Q_{ij}.

A more direct relation between Q_{ij} and Q_m can be obtained introducing the five tensors $\mathcal{Y}_{ij}^{2m}$, with $m = -2, \ldots, 2$, defined by

$$\begin{aligned}
\mathcal{Y}_{ij}^{22} &= \sqrt{\frac{15}{32\pi}} \begin{pmatrix} 1 & i & 0 \\ i & -1 & 0 \\ 0 & 0 & 0 \end{pmatrix}_{ij}\,, \\
\mathcal{Y}_{ij}^{21} &= -\sqrt{\frac{15}{32\pi}} \begin{pmatrix} 0 & 0 & 1 \\ 0 & 0 & i \\ 1 & i & 0 \end{pmatrix}_{ij}\,, \\
\mathcal{Y}_{ij}^{20} &= \sqrt{\frac{5}{16\pi}} \begin{pmatrix} -1 & 0 & 0 \\ 0 & -1 & 0 \\ 0 & 0 & 2 \end{pmatrix}_{ij}\,,
\end{aligned} \tag{27}$$

together with $\mathcal{Y}_{ij}^{2,-m} = (-1)^m (\mathcal{Y}_{ij}^{2m})^*$. These five tensors are a basis in the space of 3×3 traceless symmetric matrices and are related to the $l = 2$ spherical harmonics by

$$Y^{2m}(\theta, \phi) = \mathcal{Y}_{ij}^{2m} \hat{x}_i \hat{x}_j\,, \tag{28}$$

as one verifies immediately writing the unit radial vector in polar coordinates, $\hat{x}_1 = \sin\theta\cos\phi$, $\hat{x}_2 = \sin\theta\sin\phi$, $\hat{x}_3 = \cos\theta$, and comparing with the explicit expression of the $l = 2$ spherical harmonics,

$$\begin{aligned} Y^{22}(\theta,\phi) &= \left(\frac{15}{32\pi}\right)^{1/2} (e^{i\phi}\sin\theta)^2\,, && (29)\\ Y^{21}(\theta,\phi) &= -\left(\frac{15}{8\pi}\right)^{1/2} e^{i\phi}\sin\theta\cos\theta\,, && (30)\\ Y^{20}(\theta,\phi) &= \left(\frac{5}{16\pi}\right)^{1/2} (3\cos^2\theta - 1)\,, && (31) \end{aligned}$$

together with $Y^{l,-m} = (-1)^m Y^{lm*}$. In terms of these tensors, the relation between the cartesian components Q_{ij} and the spherical components Q_m is

$$Q_{ij} = \sum_{m=-2}^{2} Q_m \mathcal{Y}_{ij}^{2m}\,. \tag{32}$$

which can be inverted to give

$$Q_m = \frac{8\pi}{15}\, Q_{ij} (\mathcal{Y}_{ij}^{2m})^*\,, \tag{33}$$

or, explicitly,

$$\begin{aligned} Q_{\pm 2} &= \left(\frac{2\pi}{15}\right)^{1/2} (Q_{11} - Q_{22} \mp 2iQ_{12})\,,\\ Q_{\pm 1} &= \mp\left(\frac{8\pi}{15}\right)^{1/2} (Q_{13} \mp iQ_{23})\,, \\ Q_0 &= -\left(\frac{4\pi}{5}\right)^{1/2} (Q_{11} + Q_{22})\,. \end{aligned} \tag{34}$$

Since a GW is described by a tensor h_{ij} which is symmetric and traceless, its spherical components h_m can be defined as above. However h_{ij}, beside being symmetric and traceless, is also transverse, a further property that will be exploited below.

2.4 The quadrupolar modes and signal reconstruction

The reason why, in our context, the spherical components h_m of h_{ij}, are especially useful is that, carrying out the integral in eq. (24), one finds that the dynamics of $\xi_{nm}(t)$ is governed by the equation

$$\ddot{\xi}_{nm} + \gamma_n \dot{\xi}_{nm} + \omega_n^2 \xi_{nm} = \frac{1}{2}\, R \chi_n \ddot{h}_m\,, \tag{35}$$

where χ_n is a constant which can be evaluated numerically. The remarkable point is that the dynamics of the m-th quadrupole spheroidal mode is determined uniquely by the corresponding spherical component h_m, with the same m. Therefore each of the five quadrupolar modes of the sphere allows us to measure separately one of the h_m. From this, we can then reconstruct h_{ij}, using eq. (32),

$$h_{ij} = \sum_{m=-2}^{2} h_m \mathcal{Y}_{ij}^{2m} \, . \tag{36}$$

(More precisely, we measure the Fourier components $\tilde{h}_m(\omega)$ in a bandwidth around the resonance frequency ω_n). Having obtained h_{ij} in this way, we can extract the following informations.

- In the frame where the GW is propagating along the $\hat{\mathbf{z}}$ direction, h_{ij} has the form (22). The matrix (22) has the property that the eigenvalue in the propagation direction is zero (as a consequence of the fact that h_{ij} is transverse). Therefore $\det h_{ij} = 0$. Since the determinant of a matrix is invariant under rotations, it must vanish in any frame. Therefore, monitoring the five quantities ξ_{mn} we can measure the five quantities h_m (more precisely, their Fourier modes around the frequency ω_n) and we can reconstruct h_{ij} through eq. (36); then we can immediately check whether its determinant vanishes or not (with a precision that will depend on the signal-to-noise ratio). If it does not, the resulting excitation is a spurious noise, and can be discarded. If it does vanish, the excitation of the detector is a candidate GW signal. The check $\det h_{ij} = 0$ can be performed efficiently on-line, allowing us to discard most of the spurious noises that always affect GW detectors. We therefore have a powerful veto that distinguishes GWs from noises.

- If the check is passed, we can put the matrix h_{ij} in the form (22) with a rotation. The new $\hat{\mathbf{z}}$ axis after the rotation is the propagation direction of the GW and therefore we have reconstructed the arrival direction of the wave (modulo a two-fold ambiguity $\hat{\mathbf{z}} \to -\hat{\mathbf{z}}$).

- By comparing with eq. (22), we can now read off the two amplitudes h_+ and $h_\times$.

We therefore see that the five quadrupole modes of the sphere give us sufficient informations to reconstruct the arrival direction of the wave, (modulo a two-fold ambiguity $\hat{\mathbf{z}} \to -\hat{\mathbf{z}}$; however, in a two-detector coincidence, this ambiguity will be removed measuring the delay time of the signal between the two detectors), the two polarization amplitudes, and to impose a powerful veto that discriminates GW signals from noises.

Finally, eq. (35) is formally the equation of a harmonic damped oscillator subject to an external force and can be solved straightforwardly. This allows us to determine the cross section for GW absorption of the modes ξ_{nm}, basically repeating the standard computations performed for resonant bars.

2.5 Resonant transducers and the TIGA configuration

The idea of a spherical resonant-mass gravitational wave antenna was first proposed by Forward in 1971 [11]. While the potential of a spherical antenna was known for some time [12, 13], what probably deterred people from constructing resonant spheres was the fact that, just as with resonant bars, to amplify and read the signal one needs to introduces resonant transducers, one for each modes that one wishes to monitor. Thus, we must now deal with a system of at least ten harmonic oscillators, the five quadrupolar modes of the sphere and the five secondary resonators which act as resonant transducers. For a generic configuration of transducers, the normal mode structure of the system will be very complicated and all these ten degrees of freedom will couple among themselves. We can then expect that the nice property expressed by eq. (35), that there is a one-to-one correspondence between the quadrupolar modes ξ_m and the components h_m of the GW, will be spoiled. The excitation of any mode of the sphere would produce excitations in all other modes, through the common interaction with the transducers, and in practice it might be quite involved to deconvolve the output in order to read the values of the h_m.

In 1993 Merkowitz and Johnson proposed a configuration of motion sensors that solved the major practical problems in deconvolving a gravitational wave signal [23]. They derived a set of equations to describe the mechanics of a spherical antenna coupled to an arbitrary number of mechanical resonators [24]. A special arrangement of 6 resonators was proposed, which they termed the truncated icosahedral (TI) arrangement. They proposed using a truncated icosahedron as an approximation to a sphere, however the only requirement for the TI arrangement is that the transducers be placed at positions on the surface of the sphere at the center of six non-antipodal pentagon faces of an imaginary truncated icosahedron concentric to the sphere, as shown in Fig. 4. An analytic solution to the equations of motion was found for the TI arrangement and they found that direct deconvolution of the gravitational tensor components could be accomplished in principle with what they called "mode channels", a specified set of fixed linear combinations of the resonator outputs. From the mode channels, the direction and polarization information of an incident gravitational wave could be determined.

The original TIGA (Truncated Icosahedral Gravitational Antenna) model [25] assumed perfect symmetry of the sphere as well as the tuning and placement of the resonant transducers. Recently, more general models have been developed that account for any deviations from perfect symmetry [26, 27]. However, Merkowitz and Johnson found that small deviations from the ideal case (of the order of 1%) do not have a significant effect on the ability to deconvolve a gravitational wave signal [27]. Further, they have developed an *in situ* measurement technique that can be used to account for any small

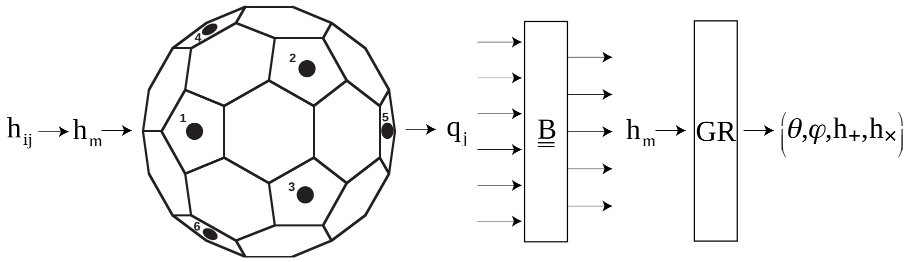

Figure 4: The TIGA technique for detecting gravitational waves. By transforming to a 5 dimensional abstract vector space, based upon the 5 spherical harmonics of order 2, a one-to-one relationship is found between the force of a gravitational wave, the 5 quadrupole modes of a sphere, and a special linear combination of the resonant transducer responses. Through these relationships and a theory of gravitation, the direction, polarization, and amplitude of a gravitational wave can be found with linear algebra using the observable transducers responses.

deviations from perfect symmetry.

The beauty of the TIGA technique is that, except for some bandpass filtering, it is simply linear algebra. This makes its implementation simple in an automated data analysis system. The *in situ* measurement technique takes into account any deviations from perfect symmetry and provides transformation matrices that enable the data to be transformed to a space where the frequency complications can be easily handled. This technique was shown to be feasible on the LSU prototype TIGA, as described below, thus its usefulness appears realistic.

Given the importance of the TIGA configuration of resonant transducers, we give in Appendix A a detailed presentation of the method, including a derivation of all relevant equations.

2.6 Properties of resonant spherical detectors: a summary

We now summarize the main results that we have discussed, or that can be obtained using the formalism presented in this section. All theoretical aspects concerning the modelization of the detector, and its response to GWs are very well understood. The main features that emerge are the followings.

2.6.1 Multi-mode capability

A resonant sphere equipped with six resonant transducers in the TIGA configurations has 6 outputs, from which one can obtain, with straightforward algebra, the two polarization amplitude h_+ and $h_\times$ of the GW and its propagation direction $\hat{\mathbf{n}}$ (modulo a sign ambiguity $\hat{\mathbf{n}} \to -\hat{\mathbf{n}}$).

For comparison, a resonant bar (or an interferometer) has only one output channel,[1] which measures a combination of the form

$$h_+ F_+(\theta,\phi) + h_\times F_\times(\theta,\phi)\,, \tag{37}$$

where $F_{+,\times}(\theta,\phi)$ are functions which depend on the detector geometry. Therefore a resonant bar or a single interferometer are unable to disantagle from their output the amplitudes h_+ and $h_\times$, and the arrival direction.

From the six outputs of the sphere we have also a veto that helps to discriminate true GW signals from spurios noises, checking that the matrix h_{ij} is transverse (i.e., it has a zero eigenvalue in the direction of propagation). This veto is of great importance, since all GW detectors are affected by spurious and non-gaussian noises, that simulate GW signals.

If we include in our analysis the presence of noise, then the ability to reconstruct the arrival direction depends on the signal-to-noise ratio. If we denote by SNR the signal-to-noise ratio in energy, it can be shown [14, 20] that, for large values of the SNR, the error made on the determination of the arrival direction is [2]

$$\Delta\Omega = \frac{2}{\mathrm{SNR}}\,, \tag{38}$$

where $\Delta\Omega \equiv \left[(\Delta\theta)^2 + \sin^2\theta(\Delta\phi)^2\right]$. It can be shown that this resolution, which is obtained from a *single* spherical resonant-mass detector, is better than what can be achieved, with the same SNR, combining the outputs of *three* interferometers [29]. Fig. 5 shows the results of a numerical simulation similar to that of Zhou and Michelson describing the error on a source direction estimate due to a finite signal-to-noise ratio.

2.6.2 Omnidirectionality

Conventional gravitational wave detectors respond to only a single tensor component of the gravitational field. Thus one of these detectors can provide an estimate for only one of the five independent components in h_{ij}. This deficiency can be overcome only by constructing 6 antennas with different orientations, which is the minimum needed to recover all components of the field with isotropic sensitivity [28].

From Eq. (35) we see that instead a spherical antenna is equally sensitive to all the tensor components of a gravitational wave. This fact demonstrates that a sphere is equally sensitive to gravitational waves of all polarizations and directions. A spherical detector is thus a truly omnidirectional antenna.

---

[1] Actually, in an interferometer, beside the differential mode one can monitor also the common mode, but this is affected by larger noises.

[2] A factor of 2 in Ref. [14] coming from an unconventional definition of SNR was corrected in Ref. [20]. Observe furthermore that here we define $\Delta\Omega \equiv \left[(\Delta\theta)^2 + \sin^2\theta(\Delta\phi)^2\right]$, rather than $\Delta\Omega \equiv \pi\left[(\Delta\theta)^2 + \sin^2\theta(\Delta\phi)^2\right]$ as done in [14, 20].

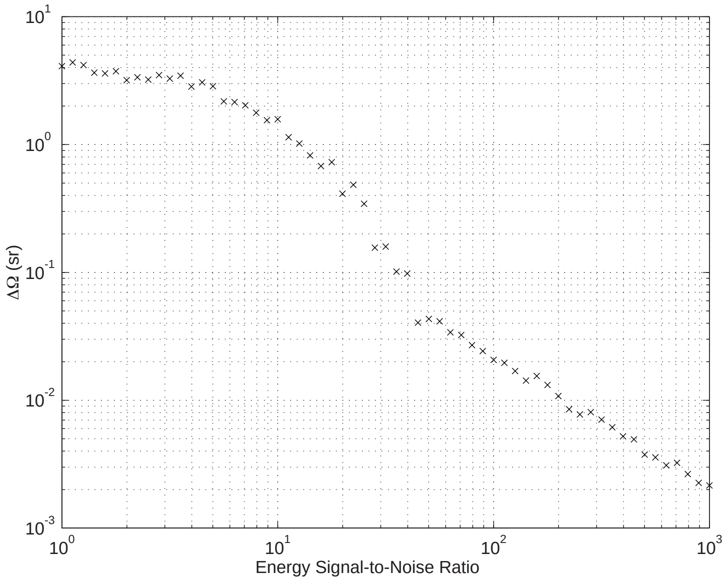

Figure 5: The results of a numerical simulation similar to that of Zhou and Michelson [14] describing the solid angle direction estimation error $\Delta\Omega$ on a source direction measurement due to a finite signal-to-noise ratio. Each point represents the results of a 200 trial Monte Carlo simulation of a direction measurement with the corresponding signal-to-noise ratio.

One might suppose that this omnidirectionality would be lost once a sphere is equipped with motion sensors to monitor the quadrupole modes. However, Merkowitz and Johnson have shown that a sphere equipped with 6 resonant transducers in the TI arrangement maintains omnidirectionality. In addition, they showed that not only could one understand the data from a spherical antenna coupled to six resonant mass motion sensors, but that there was no increase in noise compared to a bar antenna due to the additional sensors [24].

2.6.3 Large cross-section

The gravitational wave energy absorbed by a resonant detector can be

expressed in terms of the total cross section Σ_n (integrated over the frequency, around the resonant frequency ω_n), which for the quadrupole modes of a spherical detector can be written as [15]

$$\Sigma_n = F_n \frac{G}{c^3} M_s v_s^2 \,, \tag{39}$$

where n is the order of the quadrupole mode, M_s is the sphere mass, v_s is the speed of sound and F_n is a dimensionless coefficient which is characteristic of each quadrupole mode, found numerically to be $F_1 = 2.98$, $F_2 = 1.14$, and $F_3 = 0.107$.

This cross-section is larger by a factor 18 compared to that of a resonant bar working at the same resonance frequency (taking $f = 1$ kHz), simply because the mass of the sphere is much larger than that of the corresponding bar. Furthermore, this figure refers to the case when the GW hits the bar with optimal direction and polarization. Averaging over solid angle and polarization, the sensitivity of a resonant bar decreases by a factor $15/4 \simeq 3.7$, while the sensitivity of the sphere is independent of the arrival direction and polarization of the GW. Overall, the cross-section of the sphere is larger than the corresponding cross-section of a bar, averaged over solid angle and polarization, by a factor $(15/4) \times 18 \simeq 67$.

2.6.4 Multi-frequency capability

It is remarkable that, for a resonant sphere, the second-order ($n = 2$) quadrupole mode cross-section is only a factor 2.61 lower than that of the first order ($n = 1$) quadrupole mode. By comparison, in a resonant bar the harmonic $n = 2$ is not coupled to GWs [3], while the cross-section of the harmonics with $n = 3$ is suppressed, with respect to the fundamental mode $n = 1$, by a factor $n^2 = 9$.

For resonant bars, considering their present sensitivity, it is generally not considered worthwhile to afford the extra layer of complexity due to the introduction of a new transducer, to monitor the $n = 3$ harmonics, which has a cross-section 9 times smaller than that of the fundamental mode.

For a sphere this changes, both because of the improved sensitivity of the sphere in its fundamental mode, and because the $n = 2$ harmonics has a cross-section smaller only by a factor 2.61. This means that this detector can potentially be used at two frequencies [15]. A comparison of the cross-section for the first few harmonics of a sphere to those of a bar, made of the same material and resonating at the same frequency, are shown in Fig. 6.

The sphere quadrupole eigenfrequencies are found to be [16, 17]

$$\omega_n = \frac{c_n}{R_s} v_s \tag{40}$$

The dimensionless coefficients c_n are numerically found to be $c_1 = 1.62$ and $c_2 = 3.12$. A Poisson ratio value of 1/3, common to most materials including the ones we are interested in, was assumed in the reported numerical results. Values of the first and second quadrupole resonant frequencies for spheres of CuAl of different diameter are reported in Table 2. We show for comparison the resonance frequencies of Al 5056 (the high mechanical

---

[3] This follows from the fact that in a bar, for the harmonics modes with n even, the integral in eq. (24) vanishes for symmetry reasons, and is analogous to the fact that, for the sphere, the toroidal modes do not couple to GWs.

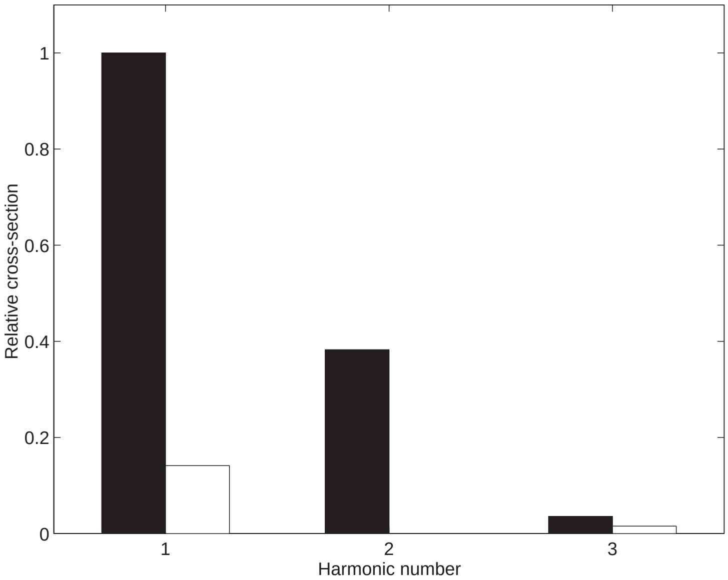

Figure 6: A comparison of the cross-section for the first few harmonics of a sphere to those of an equivalent bar. All values are relative to the cross-section of the first quadrupole modes of a sphere.

quality factor material used for the present bars) spheres. CuAl, a copper aluminum alloy, is a material widely investigated [18], chosen for the two small spherical detectors MiniGRAIL [30] in the commissioning phase in Holland and Mario Schenberg [31], under construction in Brasil. The speed of sound is 5400 m/s for Al 5056 at low temperature, and 4700 m/s for CuAl. The masses considered range from 1 ton (1 m diameter Al 5056) up to 100 tons (3 m diameter CuAl).

Considering that, in the TIGA configurations, the six transducers are all placed on the same hemisphere, it is in principle possible to put six resonant transducer in the TIGA configuration on one hemisphere, to monitor the fundamental quadrupolar mode $n = 1$ (at a frequency f of about 1 kHz for a CuAl sphere with a diameter of 2 meters, as we see from Table 2) and six more on the other hemisphere to monitor its harmonic $n = 2$ (at a frequency f of about 2 kHz for a CuAl sphere with a diameter of 2 meters).

Many typical astrophysical bursts are expected to have Fourier components extending over the $1 - 2$ kHz range. For such a signal, a sphere with two TIGA systems of transducers would be an extraordinarily clean detector. The first system of transducer provides, as discussed above, a veto (checking the transversality of the excitation) and a determination of the direction of arrival of the signal. The second system of transducers would provide another veto (checking again the transversality of the excitation) as well as a second independent determination of the direction, obtained from

	ϕ (m)	f_1 (Hz)	f_2 (Hz)
Al 5056	1.0	2850	5478
	1.5	1900	3652
	2.0	1425	2739
	2.5	1140	2191
	3.0	950	1826
CuAl	1.0	2175	4185
	1.5	1450	2790
	2.0	1087	2092
	2.5	870	1647
	3.0	725	1395

Table 2: Values of the first and second quadrupole resonance frequencies of a sphere, as a function of the diameter ϕ of the sphere.

the spherical components $\tilde{h}_m(f)$ measured at the first harmonics, and the latter determination of the direction must be consistent with the former. Such a system would therefore provide a remarkable background rejection rate. This is of great importance, given that all GW detectors have false alarms.

The implementation of a full second TIGA system of transducers, tuned to the second harmonics, is a developement that could only be implemented at an advanced stage of the project, after we have mastered the experimental complications due to the introduction of the first TIGA system. [4] However, considering that the first system of transducers, tuned to the fundamental $l = 2$ mode, already provides all the informations on the direction of the GW, the addition of a single transducer tuned the the first harmonics will be sufficient to measure the intensity of the signal in a second frequency window, expanding considerable the capabilities of the detector.

2.6.5 Testing different metric theories of gravity

Until now General Relativity has passed all the test experiments in the Solar System, as well as pulsar timing tests, with high accuracy. However, General Relativity is not the only theory of gravity that passes such tests [33]. There are alternative theories that pass the present weak field gravitational tests, and that may deviate very widely from General Relativity in the strong

---

[4] As we see from Fig 1, the radial function $a_{nl}(r)$ for $l = 2, n = 2$ happens to be numerically small on the surface of the sphere (which luckly is not the case for the $l = 2, n = 1$ mode). Therefore, for the $n = 2$ harmonics, it is not convenient to use transducers sensitive to the radial motion placed on the surface of the sphere. Since however the amplitude of the motion in the transverse direction is large at the sphere surface, as we see from the function $b_{nl}(r)$ with $n = 2, l = 2$ in Fig. 2, the first harmonics can be monitored through its tangential displacement. This could be done placing a transducer in a slot perpendicular to the sphere surface.

field regime (one example of a phenomenon in the strong field regime is the gravitational collapse of a star). Among these alternative theories, scalar-tensor theories (such as Brans-Dicke theory), predicting also a scalar, or spin-0, component of the wave, have been actively studied. Scalar-tensor extensions of general relativity emerge also naturally as the low-energy limit of string theory. In this case the scalars are the dilaton and the moduli of compactification.

In general, all these scalar-tensor theories must have a built-in mechanism that suppresses the interaction of the scalars with matter at large distances, in order not to be in conflict with the experimental confirmation of General Relativity, for instance at the Solar System scale. This can be achieved suppressing the scalar-matter interaction; for instance, in Brans-Dicke theory the scalar interaction is suppressed, with respect to the interaction of the tensor component, by a parameter ω_{BD}, and recent bounds put by the Cassini experiment constrain $\omega_{BD} > 20000$; a more subtle mechanism, the Damour-Polyakov mechanism [34], based on a specific form of loop corrections, could be at work in string theory for suppressing the dilaton coupling. Alternatively, one must give a mass to these scalar particles, so that their static large-distance interaction is governed by a Yukawa potential.

Because of these suppression mechanisms, the observation of a scalar component of GWs is even more difficult than the observation of a standard (tensorial) GW of the same amplitude. On the other hand, it has been observed that in a number of situations scalar waves could be produced with much stronger intensity than tensor waves; for instance, in a stellar collapse which preserves spherical symmetry, little or no tensor waves are emitted, while scalar waves are radiated.

It is also interesting to observe that, in an experimentally allowed range of masses, dilatons produced in the early Universe could form a relatively intense stochastic background of scalar GWs.

Therefore, even if it is not the main motivation of our investigation, the fact that a spherical detector, through its scalar mode, has the capability of detecting a hypothetical scalar components of gravitational radiation is an additional welcomed feature.

3 Experimental results

3.1 Introduction

This section summarizes what has already been achieved towards the complete design of a gravitational wave observatory based on massive resonant spherical detectors.

In the last few years significant advancements have been made to realize a spherical antenna. The barriers already overcome are:

- Practicality of the truncated icosahedral symmetry for the positioning of the transducers was demonstrated and the coupling of 6 resonant transducers with the 5 quadrupole modes of a spherical mass is well understood [25].
- Cooling large masses to ultra-low temperatures for long periods of time is possible and was demonstrated by the operation of the 2.5 ton NAUTILUS antenna at 100 mK since December 1995 [6], of the AURIGA detector at 200 mK [8] and by the initial operation of MiniGRAIL [96].
- The 5 quadrupole modes of a real spherical mass are independent and have the required high mechanical Q at ultra-low temperatures [92].
- The possibility of obtaining large pieces of material suitable for a spherical detector has been investigated. Large pieces of CuAl alloys, with high quality factors [18, 31], can be built.
- The results obtained with the MiniGRAIL detector allowed us to test techniques useful for a large spherical antenna. MiniGRAIL is large enough to develop techniques applicable to a large antenna, but is of a sufficiently manageable size to allow for rapid measurements and design changes. MiniGRAIL has been important to address the following issues:
    - Design and construct a complete cryogenic system, mechanically decoupled from the suspension system and the detector, for a sphere of about 1 meter diameter, based as much as possible on state-of-the-art, commercially available items.
    - Demonstrate the operation of the cryogenic system at a very low acoustic noise level, and show that it is capable of rapidly cooling a 1 meter diameter sphere to low temperatures.
    - Design and construct a suspension system with at least -350 dB of attenuation, without appreciable upconversion mechanisms.
    - Investigate the problems of data acquisition and processing by observing the 5 quadrupole modes of a sphere.

  - Investigate methods of attaching a resonant transducer to a sphere while maintaining a high mechanical Q.
  - Prove the quality of the solutions adopted by measuring the Brownian motion of one of the quadrupole modes of the sphere, at 4 K, with a state-of-the-art resonant transducer and SQUID amplifier to achieve highest possible sensitivity.

In the following we will describe in more detail these topics.

3.2 TIGA experiments

To verify the mechanical behavior of a spherical antenna Merkowitz and Johnson constructed a room temperature prototype in the shape of a truncated icosahedron [90, 25]. In the course of testing the mode channel theory, they successfully verified the *in situ* measurement technique that dealt with any deviations from perfect symmetry in the actual detector [27]. They tested the direction finding algorithm using an impulse excitation and found good agreement between the measured and the expected results [91].

A practical application of the direction finding technique was performed on the LSU prototype TIGA. An impulsive excitation was applied to the surface of the prototype and the response of the 6 resonant transducer mounted on the surface was measured. The amplitude and phase information of the 5 quadrupole modes of the sphere were successfully extracted from the transducer data. The strain tensor was then computed from this information. The impulse location was estimated by proper interpretation eigenvalues and eigenvectors of the strain tensor for an impulsive excitation. As shown in Fig. 7, Merkowitz and Johnson found the calculated location of the impulses to be consistent with those measured geometrically, thus verifying their technique [25, 91].

3.3 Ultra-low temperature experiments

An experimental study of the eigenfrequencies and quality factors of aluminum alloy 5056 spherical resonators at ultra-low temperatures were performed in Leiden by the Frossati team in collaboration with the ROG group [92]. Three important points were investigated:

1. The quality factor of the vibrational modes of a solid sphere at very low temperatures. Previous measurements had in fact investigated the Q of flexural modes of disks, longitudinal modes of bars and torsional modes of resonators.
2. The independence of the 5 degenerate quadrupole modes. The transfer of energy at an appreciable level between these modes could have made a potential detector useless.

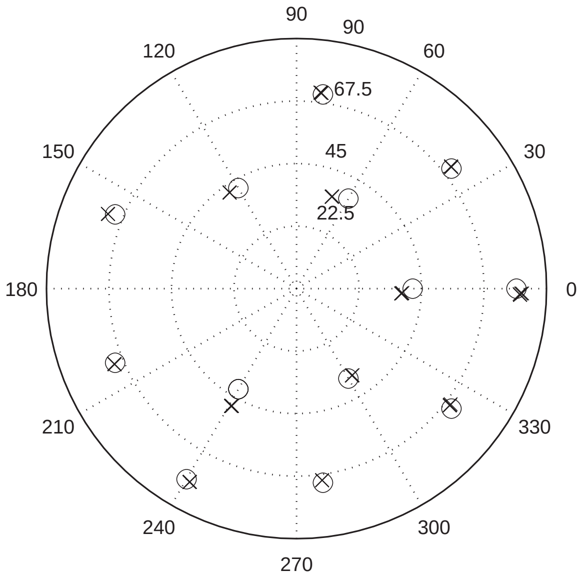

Figure 7: Location of several impulses applied to the LSU prototype spherical antenna, calculated using the TIGA technique. The x's mark the locations calculated from the motion sensor data, and the o's mark the location of the center of the shaker measured geometrically.

3. The fabrication technique to produce a large sample while preserving the high inherent Q of the material. It has been proposed [17] to use an explosive welding method to produce large-diameter spheres out of explosively-bonded plates. This technique produces high-strength bonds between similar and dissimilar metals and appears capable of preserving the inherent attributes of each parent metal.

The experimental study on several 15 cm diameter Al5056 spheres, suspended at the center of mass, answered these questions [92]. Q-values of spheroidal modes ranging from 3×10^6 to 2×10^7 in a bulk sample and from 1.7×10^6 to 8×10^6 in an explosively-bonded sample were measured. Independence of the quadrupole modes was measured within one part in 10^5 in amplitude. The influence of the suspension on the splitting of the 5 modes was understood.

After these experiments, other materials were tested in Leiden by the Frossati team; in particular copper alloys [93]. It was found that CuAl is a promising material for use as a large spherical antenna. The Lips company, in the Netherlands, is capable of casting large, high quality, pieces of this material in a spherical shape. Tests on small pieces have demonstrated that high mechanical quality factors are possible with the casting technique. The ability to cast in large pieces, along with the high thermal conductivity (lower thermal gradients, thus lower surface temperature) and relatively high

Young's modulus (high gravitational wave cross section) makes a copper alloy an appealing material for a large detector.

3.4 MiniGRAIL

MiniGRAIL is a spherical gravitational wave detector, developed in the Kamerlingh Onnes Laboratory at Leiden University in the Netherlands [94]. The antenna, made of CuAl6%, has a diameter of 68 cm, a mass of 1300 kg and a resonant frequency of about 2.9 kHz. MiniGRAIL is the first of two (the second is under construction in Brazil [95]) similar spherical gravitational wave detectors that will operate in coincidence.

The engineering runs performed by MiniGRAIL up to now have been useful to define many experimental issues relevant for the development of a large spherical detector:

1. Suspension The suspension system of MiniGRAIL consists of four CuAl6% masses and three copper masses. The upper CuAl mass is suspended from the top flange of the cryostat with three stainless steel cables, hanging from three stacks of rubber and aluminum plates. The rest of the CuAl masses are connected with three steel rods with a ring in the middle that works as a double c-spring and rounded conical nuts, 60 degrees shifted for each mass. The copper masses are suspended from three goldplated copper rods. The sphere is suspended from the centre with a copper rod of 20 mm diameter and 48 cm long. The attenuation between the last two copper masses at room temperature, in air, was about 20 dB around the resonant frequency of the sphere.

The attenuation between masses 3 and 4 was measured in a separate room temperature test facility and the diameter was adjusted to increase the attenuation around 3 kHz. The result is plotted in Fig. 8. The combination of the lower resonant frequency of the new sphere and the increased frequency of the flexural modes of the masses of the attenuation system, provides an open window of about 1 kHz around the sphere's resonances with an attenuation of about 50 dB. A similar result was achieved for the Cu masses.

2. Cooling techniques

2.1. Cooling down to 4 K with a forced helium flow. To cool the sphere down to 80 K, helium gas is circulated using two Roots pumps in series, see figure 9.

The gas is pre-cooled using a flexible tube, immersed in liquid nitrogen, as a heat exchanger. The gas flows along the sphere up through the neck of the dewar thus cooling the seven masses (each about 150 kg) of the suspension.

A temperature of about 90 K was reached within 20 hours. Below 90 K, liquid helium was transferred directly into the IVC (Inner Vacuum Can). It took another 7 h to reach 4.2K. The cool-down of MiniGRAIL using a

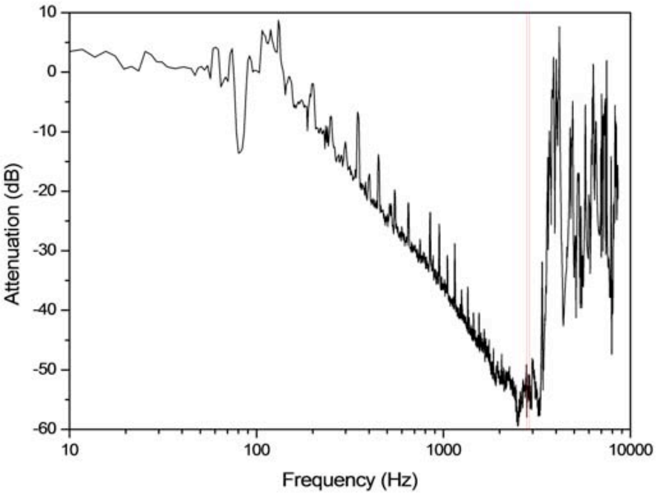

Figure 8: The attenuation between mass 3 and 4 of the vibration isolation system after modification. The gray area indicates the frequency range of the five spheroidal quadrupole modes of the bare sphere. All measurements were done at room temperature in vacuum.

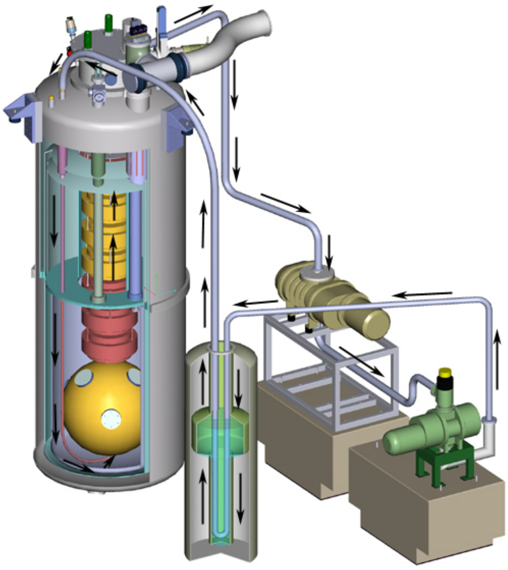

Figure 9: Experimental set-up for forced helium flow used to cool the sphere to 80 K.

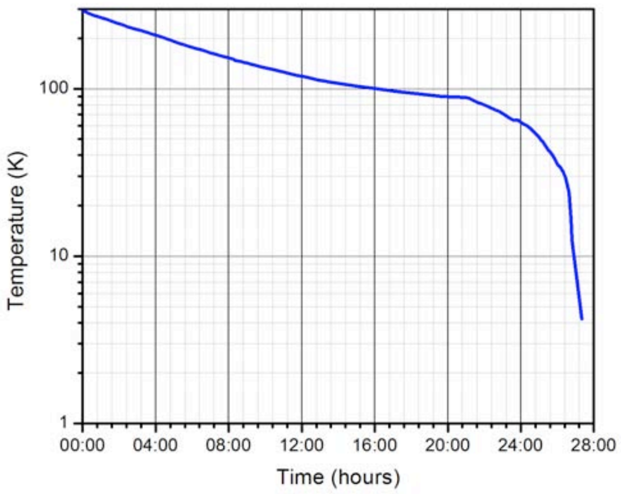

Figure 10: Cooldown of MiniGRAIL using a forced helium flow. From room temperature down to 90K, the gas was pumped around in a closed circuit, pre-cooled in a separate nitrogen dewar and injected below the sphere. From 90K down to 4K, liquid helium was directly transferred into the IVC. The total cool-down time to 4 K was 27 h.

forced flow is about a factor of 25 faster with respect to the cooling of a bar antenna using the exchange gas (figure 11).

2.2. Cooling down to milliKelvin temperature. The sphere is cooled by conduction through the last three stages of the suspension. The first copper mass is thermally anchored to the mixing chamber of the dilution refrigerator. Several cryogenics runs were made to test different thermal anchorings [96], and the best results were obtained using the Jellyfish design. The sphere reached 65 mK already 1 week after starting the dilution refrigerator (see figure 12).

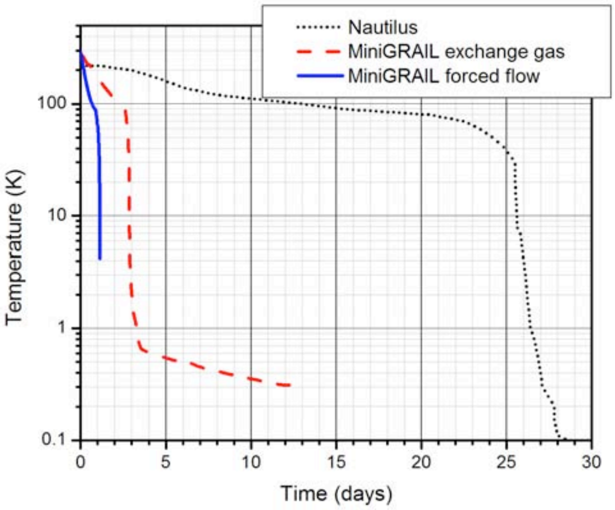

Figure 11: Cooldown of MiniGRAIL compared with a typical cooldown of NAUTILUS, the Al bar antenna in the Frascati INFN Laboratories.

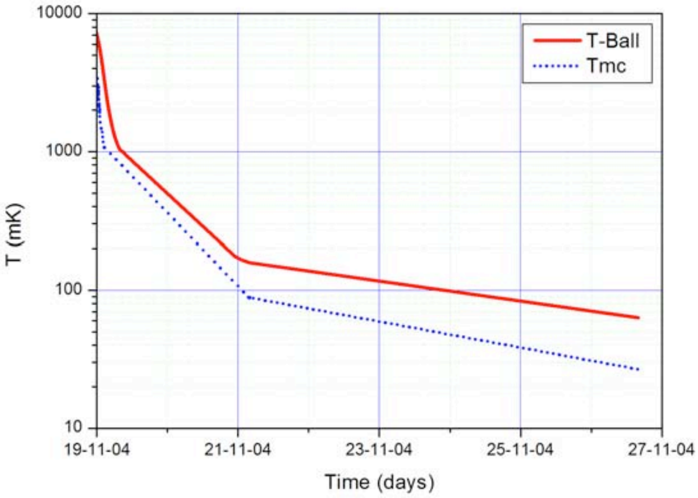

Figure 12: The temperature of the surface of the sphere compared to the temperature of the mixing chamber of the dilution refrigerator are plotted versus the time during run 7. The minimum temperatures that were achieved during this run are 65 mK on the sphere and 26 mK on the mixing chamber.

4 The SFERA detector

In this section we specify the characteristics of the detector that we propose, we investigate its noise sources and we establish what is our target sensitivity, both for a first stage and for an advanced stage of operation.

The study of the cosmic rays as a source of background for the SFERA detector is in progress. Its aim is to understand if at the final sensitivity an underground location is necessary to reduce the rate of false alarm events, or if an opportune shielding combined with a cosmic ray veto system can be effectively implemented. In any case, our plan is to install the detector for assembling and commissioning at surface, and to move it underground if eventually needed.

4.1 Specification of the detector

We propose to build a resonant-mass spherical detector with radius $R = 1$ meter, made of a CuAl6% alloy. The mass of such a sphere will be 33 ton. We will monitor its first quadrupolar spheroidal mode (i.e. the spheroidal mode $l = 2, n = 1$ in the notation introduced in chapter 2), which is at a frequency of about 1 kHz (see Table 2), using six transducers in the TIGA configuration. At an advanced stage, we will also monitor its first harmonics (i.e. the spheroidal mode $l = 2, n = 2$), which is at a frequency of about 2 kHz. The elements that guided these choices are the followings.

Radius. Increasing the radius, for a fixed choice of material, has two effects: the mass of the sphere increases as R^3 (and therefore we increase correspondingly the cross-section for absorption of GWs), and the resonance frequency decreases as $1/R$. Increasing R up to, say, 1.5 m, would bring the mass to about 100 ton, increasing by approximately one order of magnitude the financial cost (especially because of the increase in the cost of the cryostat), and would sensibly increase the experimental complexity. Furthermore, it is not evident that the increase in sensitivity due to a larger mass would make such a detector more competitive. In fact, the resonance frequency of the detector would shift toward lower values (around 660 Hz for a radius $R = 1.5$ m). In this region interferometers have a better sensitivity than they have at 1 kHz, which raises the bar for what can be considered a competitive sensitivity.

On the other hand, taking a smaller value of R decreases the sensitivity and increases the resonance frequency, gradually moving it outside the region $f <$ a few kHz, which is considered the most intersting for astrophysical reasons.

The choice $R = 1$ meter, which for our choice of material gives a resonance frequency $f \simeq 1$ kHz, is therefore the best compromise, which allows us to explore a region of frequency considered among the most interesting for GW astrophysics, while keeping under control the financial cost and the experimental complexity.

Material. CuAl6% is chosen because of its high quality factor ($Q \simeq 10^7$ at cryogenic temperatures), high sound velocity ($v_s = 4700$ m/s) and a large thermal conductivity. It is the material already used for MiniGRAIL.

4.2 Noises

The sources of noises that affect a resonant-mass detector can be divided into two groups; noises intrinsic to the detector, such as the thermal noise and the noise in the readout, and external disturbances, such a seismic noises or cosmic rays.

Thanks to the large experience gained with resonant bars, as well as with MiniGRAIL, all intrinsic noise sources are very well understood. We have programs that simulate the response of these detectors to the noises, and which reproduce very satisfactorily the noise curve measured experimentally: *the intrinsic noises that affect resonant-mass detectors are very well understood.*

Concerning the external disturbances, the effect of cosmic rays on a 33 tons resonant detector is more important than on present resonant bars, and we will discuss it in detail in the following section.

4.3 Cosmic rays

The effects due to the cosmic ray interactions in the sphere set a limit to the sensitivity of a resonant detector running in a site not shielded from cosmic rays. This effect can be computed using the thermo-mechanical model; in this model the effect of the cosmic ray is a local heating exciting the detector's vibrational modes. There are several sources of uncertainty in estimating the event rate, the most important being:

1. the details of the hadronic core of the cosmic ray induced showers.
2. the validity of the thermo mechanical model for a superconducting material.

An important test of the calculations are the results of NAUTILUS and EXPLORER antennas that are equipped with a cosmic ray detector [110, 111, 112, 113].

4.3.1 Rate calculation

A cosmic ray crossing the sphere produces along its path in the medium a local overheating phenomenon which can be related to a local over pressure. Such perturbations propagate acoustically to the entire detector and finally excite vibrational eigenmodes. The relation between the particle energy loss dE along a path dX and the energy E_n in the n^{th} vibrational mode [114] is:

$$E_n = \frac{1}{2}\frac{l_0^2}{V}\frac{G_n^2}{\rho v^2}\gamma^2\left(\frac{dE}{dX}\right)^2 \tag{41}$$

where l_0 is the track length of the cosmic ray in the detector and V is the detector's volume. γ, ρ and v are the Gruneisen's dimensionless parameter, the mass density, and the speed of sound in the medium respectively. The "form factor"

$$G_n = \frac{v}{\omega_n}\frac{1}{l_0}\int_{l_0} div_{\perp} u_n dl \tag{42}$$

is related to the geometry of the detector through the eigenmode u_n, and it is expected to be of order unity for a large number of modes and paths. If we take $G_n = 1$ and assume that is constant along all the paths, the relation between the energy released by the cosmic ray (ΔE) and the vibrational energy in the mode E_n can be estimated for a sphere at low temperature:

$$E_n\,(Kelvin) = D \times (\Delta E\,(GeV))^2 \tag{43}$$

where $D = 3.2 \times 10^{-9}$ for a 2 m aluminum sphere and $D = 0.6 \times 10^{-9}$ for a CuAl sphere. Different types of particles can interact with a resonant detector at sea level: muons, electrons, hadrons. Montecarlo calculations of the effect due to single particles, muons and hadrons, is in reference [110]. Simulations were made using the GEANT package to estimate the energy absorbed in the sphere. The muon and hadron fluxes were taken from experimental data. The effect due to the interactions of Extended Air Showers (EAS) (electrons, muons or hadrons from the core of a cosmic ray cascade) is difficult to evaluate as cascades produced in the atmosphere from primary cosmic rays are complex processes not yet fully understood in details and there are technical problems due to the large number of particles involved. We have done a rough estimation of the rate for extensive air showers and multiple hadrons using simplified hypotheses. In table 3 we summarize the results obtained in [115] for an aluminum sphere 3 meters in diameter. To give an idea of the importance of the cosmic ray effect the last columns reports the signals/day of an antenna close to the quantum limit with an effective temperature of 2×10^{-7} K and a resolution time of 5 ms. A 2 m CuAl sphere shall have an event rate/day higher by a factor 3.5 - 4. A study of how the energy of a cosmic ray particle interacting with a spherical antenna is distributed over its eigenmodes can be found in ref. [116].

To have a more precise estimate of the effect of cosmic rays, a full simulation for the case in which multiple particles are interacting with the sphere is necessary.

Mode energy threshold (K)	ev./day muons	ev./day hadrons	ev./day (EAS)	ev./day multi had.	ev./day total
10^{-7}	126150	63770	2870	–	192800
10^{-6}	10870	8200	535	–	19600
10^{-5}	940	1110	100	22	2180
10^{-4}	84	120	19	20	245
10^{-3}	10	12	4	17	43
10^{-2}	0.5	1.3	0.6	2	4.4

Table 3: The number of cosmic ray events per day calculated from a Monte Carlo simulation for a 3 m diameter aluminum sphere. A 2 m CuAl sphere shall have an event rate/day higher by a factor 3.5 - 4.

4.3.2 Cosmic ray rejection

There are basically two possibilities to cope with the cosmic ray background: the first is to install an active veto with a cosmic ray detector; the second is to put the antenna in an underground site. Both possibilities shall be considered as the detector's sensitivity improves. The rate of cosmic rays impinging on a 2 m sphere is of the order of 1 kHz. This means that is not possible to do a veto system with a simple layer of detectors signaling all the cosmic rays, the resolution time of the antenna being in the range of few milliseconds. The veto should therefore be capable to identify cosmic rays that may eventually loose a large fraction of energy in the antenna, i.e. identify energetic muons, hadrons and showers. This should be done mainly on the top of the antenna; in fact, due to the large mass of the sphere, in most of the cases with a single incident particle, no secondaries will come out from the sphere in case of interaction with a large energy loss. A very interesting application of this detector will be the possibility to compare the direction measured from the cosmic ray detector for single particles with the one measured from the sphere using the excitations in the different modes. In this way a continuous calibration of the sphere capability to measure the direction will be possible. Another possibility for the veto is to shield the antenna from the electromagnetic and hadronic components of the cosmic ray with absorber and use cosmic ray detectors only for energetic muons (for example a TRD). A fundamental assumption in the calculation of the cosmic ray event rate is the thermo-mechanical model. The thermo-mechanical model has been tested on a bar at room temperature[117, 118] . However, when a material becomes superconducting several parameters change, namely the specific heat decreases to zero with temperature and the Gruneisen coefficient might vary as well, the net effect of cosmic rays is expected to change. The material might become locally not superconducting at the passage of a ionizing particle; in this picture, the standard calculations are still valid.

Of course, the results obtained with NAUTILUS and EXPLORER are very important to check the validity of the overall picture. At present, the sensitivity of these detectors is such that only signals from cascades (extended air showers with hadrons and muons) are detected. We remind that the uncertainty in the rate calculation for this type of events is very large due to the complexity of the cosmic ray cascade. Single muons/hadrons have a larger effect on the noise of a spherical antenna operated near the quantum limit. For this kind of events the uncertainty due to the cosmic ray is small, the main uncertainty in the calculations comes from the thermo-mechanical model.

We observed in NAUTILUS deviations from the predictions of the thermo-mechanical model when the detector was operated at 0.1 K, in superconducting regime [112].

To clarify this problem, the RAP experiment is under way: it studies the interactions of the 0.6 GeV electron beam of the DAΦNE Beam Test Facility at INFN Frascati National Laboratory with a small bar made of the same Al alloy as NAUTILUS, both above and below the transition temperature [119, 120] as well as other normal conducting and superconducting materials. One can draw the following scenario: the sphere will be commissioned in a suitable facility, unshielded from CR's. The antenna will then require CR veto to detect both single muons and EAS (with multiplicity). With improved sensitivity the veto will be no longer sufficient and the antenna shall be installed underground, shielded from low energy secondaries.

4.3.3 Proposed Cosmic Ray veto

It has been pointed out that the rate and the energy lost by CR's in the antenna may spoil completely the antenna operation and that a CR veto is necessary. The veto shall be able to estimate EAS multiplicity as well as single particle direction. The NAUTILUS veto uses layers of streamer tubes above and below; at EXPLORER plastic scintillators with phototube readout, also above and below. They are both designed to detect single muons for CR detector calibration and EAS's multiplicity for antenna veto. They do not provide granularity sufficient to trace muons inside a sphere, however, it will be very useful to have a veto system similar to the Explorer one. During the first phase of operation of the sphere, when the best performances will not yet be reached, only cosmic ray showers will be able to produce detectable signals in the sphere. Later on, when the detection also of single particles will become important, the system could be integrated with other detectors. For example, the possibility to continuously calibrate the sphere read out in signal direction with single muons, could be achieved with a compact muon telescope movable around the cryostat. If the antenna is installed underground care shall be taken to veto high energy CR muons and muons due to in-the-earth neutrino interactions.

4.4 Cryogenics for SFERA

The minimum energy that can be detected with a resonant spherical gravitational wave antenna fitted with quantum limited SQUID amplifiers of noise temperature T_N is given, in terms of an effective temperature $T_{eff\,QL}$ by

$$T_{eff\,QL} = \frac{T}{\beta Q} + 2T_N \tag{44}$$

where T is the thermodynamic temperature of the sphere, Q is the mechanical quality factor and β is a parameter smaller than 1 that measures the ratio between the energy transferred to the transducer and that deposited in the sphere by the gravitational wave. A sphere of 2m diameter made of CuAl 6% will resonate at 1 kHz that is, at a frequency 2/0.68 =2.94 times lower than MiniGRAIL which resonates at frequencies between 2800 and 3050 Hz for the 5 fundamental spheroidal quadrupole modes (at low temperature). The minimum SQUID noise is hence

$$T_N = \frac{h\nu}{k_B} = 4.3 \cdot 10^{-8}\mathrm{K} \tag{45}$$

so that

$$\frac{T}{\beta Q} \leq 8.6 \cdot 10^{-8}\mathrm{K} \tag{46}$$

Values of Q of $2 \cdot 10^7$ have already been measured in the CuAl 6% alloy [97] and $\beta \sim 0.1 \div 0.2$ should be attainable, so if we take β=0.1 and $Q = 5 \cdot 10^6$ we require a thermodynamic temperature of 42 mK. The 1.3 ton MiniGRAIL sphere plus the suspension total about 2 ton and have already been cooled to 64 mK and progress is being made to reach lower temperatures so we are confident that the 2 m sphere will also be cooled to similar temperatures. We describe briefly how we plan to cool the large sphere and suspension from room temperature to the low mK region.

4.4.1 Cooling from 300K to 4K

The heat to be removed from the sphere and suspension system is shown in the following table.

Temperature range (K)	Enthalpy H (J/gm)	Energy (J)
300 - 160	37.0	$2.0 \cdot 10^9$
160 - 80	22.5	$9.0 \cdot 10^8$
80 - 4	6.0	$2.4 \cdot 10^9$

If we would upgrade the MiniGRAIL method, 20000 liters of liquid nitrogen would be needed to cool down to 80K and another 12000 liters of liquid helium would be needed to cool down further to 4K. The costs would be about 130000 euros per cool down, which is clearly not feasible. Our suggestion is to use GM-cryocoolers that would only be used for the pre-cooling and then turned off. Model UGM 600 from Cryomech has a cooling power of 600W at 77K and about 1200 at 250K so we would use 4 of them for a cooling power of 4800W and a cool-down time of 8 days to 60K. This would decrease the pre-cooling time to below 12 days.

4.4.2 Cooling to mK temperatures

Since this antenna could be eventually operated in an underground site, we decided to avoid liquid cryogens for the normal operation of the antenna, also in view of the maintenance costs and to increase the detector duty cycle. The antenna and suspension will hence be cooled during normal operation, by pulsed tube refrigerators (PTR) of the type PT410 of Cryomech and by a dilution refrigerator without 1K pot. PTR coolers produce less vibrational noise than a liquid nitrogen bath plus a helium bath and can now be found with separated valve head to further reduce vibrations. We chose the PT410 because of the cooling power of 1W at 4.2K which is higher than that of other products in the market. The absence of liquid helium precludes the use of a 1K pot for the dilution refrigerator. A Joule Thompson heat exchanger (JTHE) is hence used to pre-cool the incoming 3He mixture that enters the JTHE at ∼4K. A PTR dilution refrigerator of this type has recently been built for the SCUBA telescope that has the highest cooling power available at present for this type of refrigerator with 650 μW at 120 mK and can circulate 1.5 mmol/s. This refrigerator, shown below uses one PT410. For the present

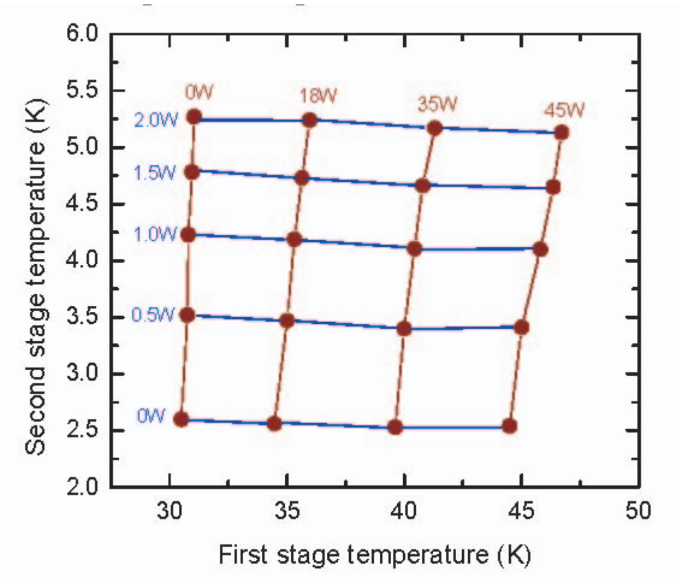

Figure 13: Low temperature part of the cooling power diagram of a PT410

project a PTRDR (Pulse Tube Refrigerator Dilution Refrigerator) with a cooling power of ∼2 mW at 120 mK which should be enough to cool the 2 m sphere to below 80 mK if the heat leak from the sphere/suspension is lower than 200 μW. We cannot say much about what to expect from the 33 ton sphere since we do not know how it scales with size but we know it will decrease in time. It could start at 1 mW and after a few weeks decrease to 0.2 mW if we scale the MiniGRAIL values by a factor 10 up, but it could also be less, depending on the solidification and annealing of the sphere after casting. Based on the SCUBA experience we will build a PTR-DR with larger cooling power and with characteristics that will further decrease the vibrational noise transfer to the antenna. This will be done by having the still, the intermediate stage and the mixing chamber to be very massive and coupled with each-other by flexible heat exchangers so that vibration attenuation will occur, as for the suspension of the antenna itself. Each of the three stages will be coupled to a damping mass by means of very soft yet high thermal conductivity "jelly-fish" type of conductors successfully tested with the MiniGRAIL antenna.

4.4.3 Suspension

In order to maximize the attenuation of external vibrations the sphere will be suspended from a stack of 7 masses, each one of about 1000 kg. The masses will be linked to each other by means of hard steel springs that should damp the motion above 10-20Hz. The coiled type of spring also helps in decreasing the thermal conduction from one mass to the other for the first 4 masses, (made of the same alloy as the sphere CuAl6%) that will be between 4K and 50-100 mK. The last 3 masses will be made of pure copper. The first of the 3 (see drawing below) will be connected to the mixing chamber of the dilution refrigerator. The 3 masses will be connected using the same springs as the upper ones and thermally anchored using thin copper foils similar to the jelly fishes used to link the DR to the masses. The center rod will be made of copper. Traction tests will be done on all parts subject to possible rupture to ensure a good safety margin.

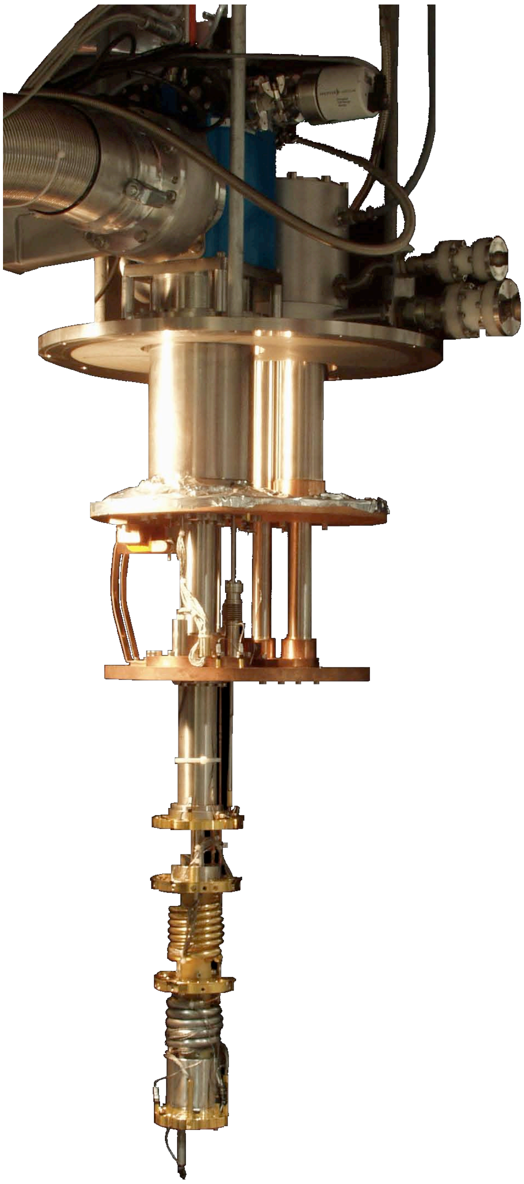

Figure 14: PTR-DR with a cooling power of 650 μW at 120 mK and a circulate rate of 1.5 mmol/s.

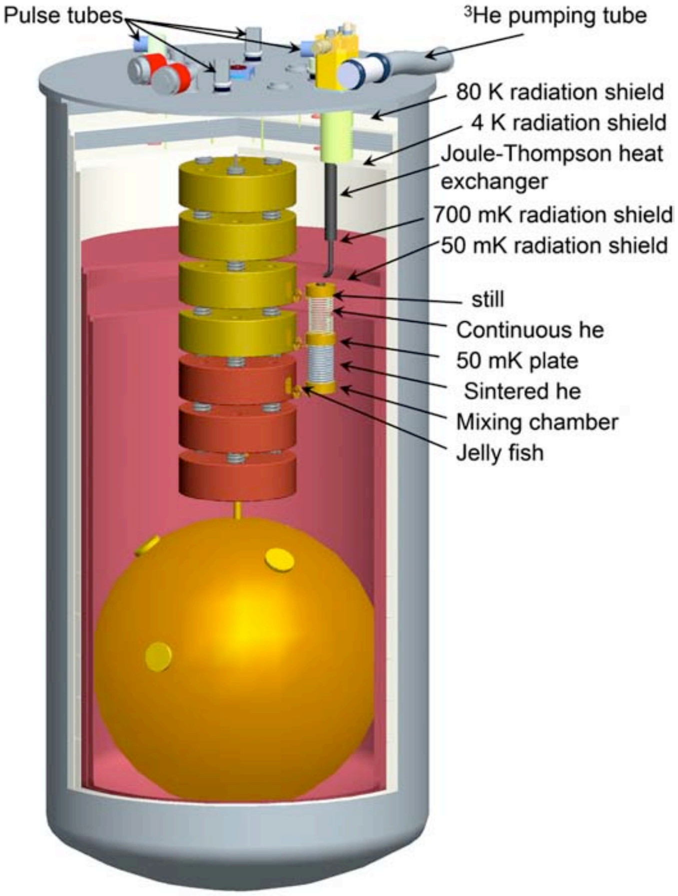

Figure 15: A schematic view of the large sphere, cooled by a PTR-DR.

4.5 Read-out

After a signal has been picked up by the antenna, it must be amplified and recorded for analysis. The transduction of extremely small vibrations is still an open challenge of technology: the aim is to reach, and possibly overcome, the standard quantum limit (SQL) of the detection of a single quantum of oscillation. For frequencies around 1 kHz, we have $\hbar\omega \sim 10^{-30}$J $\sim 10^{-7}$K. The only viable way to achieve this is to transform the signal into electromagnetic energy, and then use state-of-the-art techniques for electromagnetic amplification and readout.

Transducers for resonant–mass gravitational wave antennas fall into two categories: *passive* transducers and *parametric* transducers. Passive transducers have no external power source, and their power gain is less than unity. They must always be used with a high–gain, low–noise amplifier at the frequency of the antenna. Parametric transducers, on the other hand, have an external power source (a pump oscillator at frequency ω_p) which is modulated by the antenna motion. They have intrinsic power gain associated with the transfer from the antenna frequency ω_a to the higher frequency ω_p.

The ROG Collaboration is developing both parametric and capacitive transducers. Parametric transducers in the r.f. to microwave region look promising. An intense R&D is underway to develop parametric devices.

On the other hand capacitive transducers have been developed in the ROG group for a very long time and brought to a very good level of reliability. The facts that they can be fabricated from the same material of the antenna and can be extensively tested at room temperature are definite advantages of these devices.

The proposed strategy for the SFERA project is to continue the development of both passive and parametric transducers, and to use the best device available at the moment. A more detailed description of the capacitive and parametric read-out is given in the following sections.

4.5.1 Capacitive read-out

Let us briefly recall some of the terms and concepts that will be used in this section:

Transducer An electromechanical transducer is characterized by its transduction coefficient α [V/m], that depends on the strength of the stored e.m. field and on circuit parameters. For a capacitive transducer, e.g., it is simply the electric field E in the gap, up to negligible corrections. Other relevant parameters are its electrical output Impedance Z_{22} and its mechanical input impedance, function of the resonator mass and frequency. Following the usual Giffard's notation we can write, for linear (non parametric) transducers:

$$f(t) = Z_{11}\dot{x}(t) + Z_{12}i(t) \tag{47}$$

$$v(t) = Z_{21}\dot{x}(t) + Z_{22}i(t) \tag{48}$$

where the reverse transducer action,called *back action* (current in the circuit producing force on the resonator) is also shown. Clearly, $\alpha \equiv j\omega Z_{12}$. The Z_{ij} matrix connects the input variables (force $f(t)$ acting on the transducer and velocity $\dot{x}(t)$ of the transducer mechanical parts) with the output variables (voltage $v(t)$ and current $i(t)$). In important cases the Z_{ij} components satisfy the relationships $Z_{11}Z_{22} = Z_{12}Z_{21}$ and $Z_{12} = Z_{21}$.

The *energy coupling coefficient* β is constructed from these parameters and is a good figure of merit of a transducer:

$$\beta = \frac{1}{m\omega}\frac{|Z_{21}|^2}{Z_{el}} \tag{49}$$

Usually the total electric impedance $Z_{el} = Z_{22} + Z_{circuit} + Z_{ampl}$ of the whole output circuit is considered in β

Resonant transducers are invariably used in modern antennas, because the use od a light mass auxiliary resonator allows us to substitute the value $m_t \sim 1kg$ for $m_a \sim 1000kg$ in the denominator of β. We can consider the second oscillator of mass m_t as an impedance matching device between the stiff antenna and the low input impedance of the mechanical amplifier. In this case, also the Q of the auxiliary resonator is a relevant parameter.

Amplifier A real linear amplifier can usefully be schematized as an ideal amplifier (with zero or infinite input impedance) plus an input impedance and two noise sources: voltage noise e_n and current noise i_n. One of these (depending on whether we use a ideal current or voltage noise) appears as a white additive noise, the other produces circulating currents in the transducer output circuit that give rise, via reverse transduction, to the so called back-action.

To model a SQUID (that is properly a flux to voltage transducer) a current amplifier model is appropriate: we then need specify the input impedance (the mutual inductance M of the input transformer) and flux noise ϕ_n so that $i_n = \phi_n/M$ as the additive noise, and voltage noise e_n, responsible for circulating currents that produce a (hardly detectable) back-action.

Matching circuit Often the transducer output impedance is poorly matched to the amplifier input; such is the case of a capacitive transducer ($Z_{22} = 1/\omega_a$ C$\sim 10^5\Omega$) coupled to a SQUID ($Z_{ampl} = \omega L_{in} \sim 10^{-2}\Omega$. A matching circuit is then needed to couple the two devices. In simpler cases it can be a very simple one (just an inductor, or a capacitor), but in the above mentioned instance a superconducting transformer is needed. This implies two consequences: a) the circuit impedance seen by the amplifier Z_{tot} can

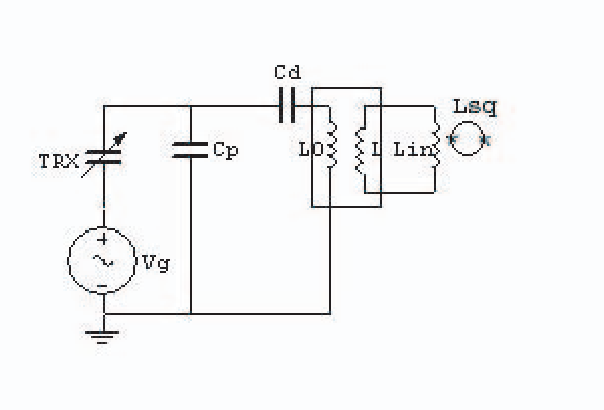

Figure 16: Scheme of the readout electronics.

no longer be considered constant or slowly varying with frequency and b) a third, electrical resonator (transducer capacitor + transformer inductor) is added to the detector. If the resonant frequency of this circuit is close to the mechanical resonances (as it should be, for efficient matching) then a full three mode detector modeling is needed.

Mechanical Amplifier These blocks (transducer, circuit, amplifier) are often lumped together by defining a *mechanical amplifier* i.e. a "virtual" device that contains in itself both the transduction and the amplification process. In this case the two noise sources become, by properly scaling the electrical sources by the parameter α, a displacement noise x_n and a force noise f_n.

Influence of the readout chain on the noise temperature of the detector An important parameter to describe the sensitivity of a resonant detector is the so called effective temperature kT_{eff}, that represents the minimum detectable energy innovation. It can be written in a convenient way in terms of the noise temperature of the amplifier T_n, the thermodynamic temperature of the detector T, the energy coupling coefficient β and the quality factor Q [51]

$$kT_{eff} \simeq 2\sqrt{2}kT_n \left(1 + \frac{2T}{\beta Q T_n}\right)^{1/2} \tag{50}$$

and characterizes the overall noise in the detector. The purpouse of this section is to describe the role of the electronic components on the value of T_{eff}, which has to be as low as possible.

From figure (16) we see that the capacitive transducer (C_t and its parasitic capacitance C_p) is coupled to the d.c. SQUID via a superconducting high-Q transformer. The effect of the transduction can be represented by an equivalent voltage generator

$$v_g = E(y - x) \tag{51}$$

where E is the electric field stored in the transducer and $y - x$ is the relative motion of the transducer with respect to the face of the antenna. We can neglect the losses of the superconducting transformer [52] because of the high Q and as long as the resonance frequency of the electrical mode is far from mechanical modes. Using Thevenin's Theorem, the voltage across the transducer is

$$v_g' = v_g \frac{C_t}{C_t + C_p} \tag{52}$$

By defining the following parameters:

- $M_1 = k_1 \sqrt{L_0 L}$ is the mutual inductance of the transformer and k_1 is its coupling coefficient;
- $M_2 = k_2 \sqrt{L_{in} L_{SQ}}$ and k_2 are the mutual inductance and the coupling coefficient between the d.c. SQUID and its input coil respectively;
- C_d is the decoupling capacitor, needed to charge the transducer;
- L_0 and L are the inductances of the primary and secondary coil of the transformer respectively;
- L_{in} is the inductance of the input coil of the SQUID and L_{SQ} that of the SQUID itself;
- $\gamma_s = \frac{L}{L+L_{in}}$.

It is possible to see that, neglecting the effect of the SQUID, the current flowing in the secondary coil is

$$i = v_g \left(\frac{C_t}{C_t + C_p} \right) \left(\frac{\sqrt{\frac{L_0}{L}}}{j\omega L_0 k_1 - \frac{1}{\gamma_s k_1} (\frac{1}{j\omega C} + j\omega L_0)} \right) \tag{53}$$

where

$$C = \frac{C_d (C_p + C_t)}{C_p + C_t + C_d} \approx C_p + C_t \tag{54}$$

is the equivalent capacitance as seen from L_0, while the second equality is true only if $C_d \gg C_p + C_t$. By introducing the effective transformer ratio $N_e = \sqrt{\frac{L_0}{L}} k_1 \gamma_s$ we obtain

$$i = v_g \frac{C_t}{C_t + C_p} \frac{N_e}{Z_0(\omega)} \tag{55}$$

where the total impedance has been introduced

$$Z_0(\omega) = \frac{1}{j\omega C} + j\omega L_0(1-\gamma_s k_1^2) = \frac{1}{j\omega C}\left(1-\frac{\omega^2}{\omega_{el}^2}\right) \tag{56}$$

with the resonance frequency of the electrical mode

$$\omega_{el}^2 = \frac{1}{CL_0(1-\gamma_s k_1^2)} \tag{57}$$

Now we can relate the magnetic flux in the SQUID, $\Phi = M_2 i$, with the mechanical signal

$$\Phi = M_2 i = \alpha_\phi (y-x) \tag{58}$$

and

$$\alpha_\phi = \frac{C_t}{C_t + C_p}\frac{N_e M_2}{Z_0(\omega)} = j\omega C_t \frac{N_e M_2}{\left(1-\frac{\omega^2}{\omega_{el}^2}\right)} \tag{59}$$

We get the unexpected result that, as long as $\omega_{el} > \omega_\pm$, ($\omega_\pm$ are the frequencies of the mechanical normal modes) α_ϕ does not depend on C_p.

Besides, it is clear that to maximize the signal fed to the SQUID it is necessary a transformer with a high coupling constant and a high effective transformer ratio.

The signal on the SQUID due to the brownian noise is [52]

$$\Phi_{Br} = \alpha_\phi \sqrt{\frac{k_b T_e}{2 m_y \omega_\pm^2}} \tag{60}$$

Inserting equations (59) and (60) in equation (50), for T_{eff} one has

$$kT_{eff} = \frac{4\phi_n}{M_2 C_t E}\left[\frac{1}{N_e}\left(1-\frac{\omega^2}{\omega_{el}^2}\right)\right]\sqrt{\frac{kT_e m_y}{\tau}} \tag{61}$$

Where ϕ_n is the intrinsic noise of the SQUID, m_y the mass of the transducer and τ is the common amplitude decay time of the modes.

From equation (61) it is clear that to minimize T_{eff} it is necessary to have a low noise (ϕ_n) and high coupling (M_2) d.c. SQUID, C_t as high as possible and a high τ. Since τ is related to the Q by the well known formula

$$Q = \pi\nu\tau \tag{62}$$

the last condition corresponds to a high Q. Both the bar and the transducer have Qs of the order of 10^6 and the overall Q of each mode of the detector is, roughly speaking, given by

$$Q_{tot}^{-1} \propto Q_{bar}^{-1} + Q_{trasd}^{-1} + Q_{el}^{-1} \tag{63}$$

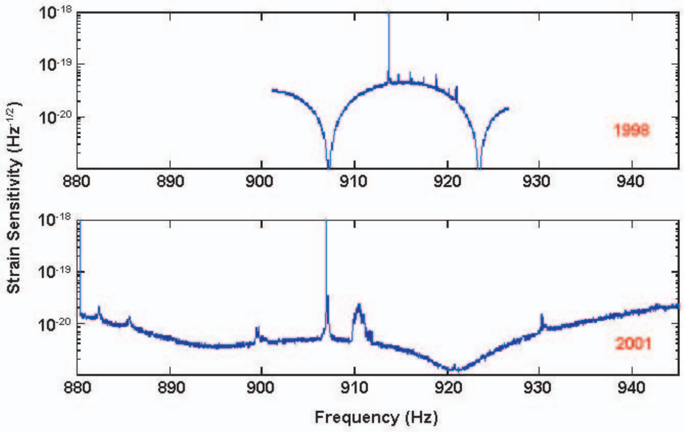

Figure 17: Experimental strain sensitivity of EXPLORER in 1998 (upper figure) and 2001 (lower figure), after the upgrade of the readout.

So the need to have Q_{el} of the same order of magnitude as those of the bar and transducer.

Present status of capacitive readout Both EXPLORER and NAUTILUS are now equipped with new “rosette” single-gap capacitive transducers [53], with a gap of the order of 10μm, and commercial single-stage d.c. SQUIDs, with energy resolutions of a few thousand $\hbar$s. These readout have been installed in 1999 and 2002 respectively, achieving a considerable increase of the useful signal bandwidth [54] (see fig. (17)) and, thus, in an increase of sensitivity.

At present EXPLORER is cooled to 2.6 K and NAUTILUS to 3.5 K, both reach peak sensitivities of about $1 \div 2 \cdot 10^{-21}\mathrm{Hz}^{-1/2}$ and a bandwidth, at the level of $10^{-20}\mathrm{Hz}^{-1/2}$, of about 45 Hz for EXPLORER and 35 Hz for NAUTILUS. The noise temperature of the detectors is about 2 mK, corresponding to a sensitivity to burst $h = 3 \cdot 10^{-19}$. The duty-cycle is of the order of 90%, only limited by cryogenic operations.

Future capacitive readout

Double-gap transducer The transduction efficiency β is given by the ratio between the mechanical energy of the transducer and the electromagnetic energy stored in the gap, and for a capacitve transducer equation (49) becomes

$$\beta = \frac{CE^2}{m\omega_0^2} \tag{64}$$

where C is the total capacitance of the transducer, E the biasing field, m the resonator mass and ω_0 its resonance frequency. It turns out from eq.

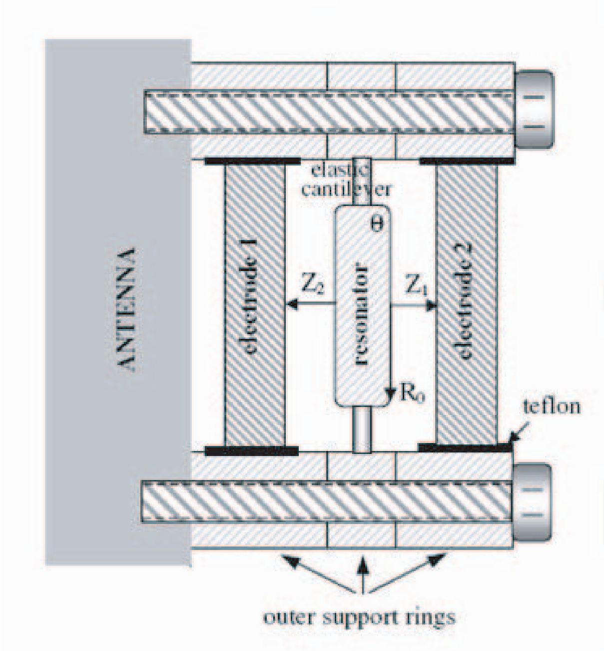

Figure 18: A schematic view of the double-gap transducer.

(64), that a way to increase β is to increase the capacitance C.

The idea followed by the ROG Collaboration is the double-gap trasducer (fig. (18) shows a scheme of the device). A "rosette" resonator is enclosed between two identically spaced electrodes, i.e. two identical gaps. The circuital scheme of the transducer, the matching transformer and d.c. SQUID amplifier is showed in fig. (19). This setup has the net effect to double the total capacitance C of the transducer, thus to increase the transduction efficiency β.

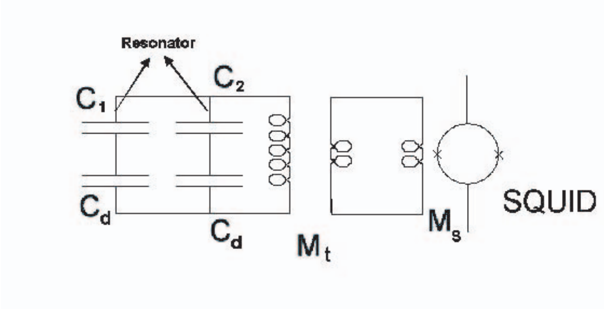

Figure 19: The circuital scheme of the double-gap transducer, connected to the matching transformer and d.c. SQUID amplifier.

Moreover, by properly biasing the two gaps, one with a positive voltage and the other with a negative voltage with respect to the resonator, it is straightforward to see that the signal current flowing in the primary coil of the transformer is twice that in the case of a single gap transducer.

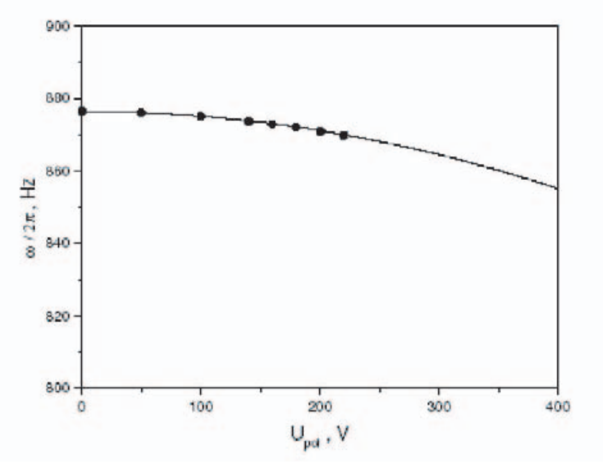

Figure 20: Comparison of the theoretical values of ω_0 with experimental values for the two-gap transducer: the full curve represents theoretical results and the circles are experimental points.

A double-gap transducer has already been designed, assembled and tested at liquid helium temperatures. The value for both gaps was of the order of 15μm and the mechanical quality factor was found to be $1.0 \cdot 10^6$ when the transducer was biased with field of about 20 MV/m. Moreover the dependence of ω_0 on E_{bias} has been fully investigated finding a good agreement between the measured and calculated [55] values (see fig. (20)).

On a sphere 2m in diameter we can straightforwardly export current technology as we use it today. The two main design criteria are indeed the physical dimensions (mainly its diameter D), that should be negligible or small with respect to the sphere curvature radius (a transducer should in principle sense the motion of one point on the sphere surface), and the resonant frequency. A 2m sphere of CuAl will resonate around 1 kHz, just like our present bars, and will have linear dimensions that can well tolerate D=230 mm transducers as we use now. So the present design can be exported as is, with the unique difference of the material, that will obviously be CuAl and not Al5056.

Double SQUID amplifier

Gravitational wave detectors require the highest possible sensitivity of a d.c. SQUID. In this case the standard readout may not be the best solution, because the overall sensitivity can be limited by the room-temperature preamplifier noise. With this setup an energy resolution of about $3000\hbar$ has been measured [56] .

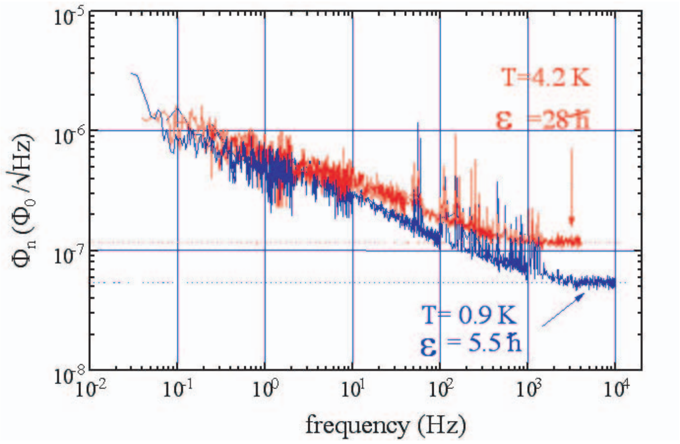

Figure 21: Noise spectra of the ROG double-SQUID amplifier expressed in $\Phi_0/\sqrt{\text{Hz}}$ at 0.9 K and 4.2K. We also show in the figure the corresponding energy resolutions.

In the last years, it has been shown [57, 58, 59] that a double-SQUID system can reach quantum limit energy resolution and that a double-SQUID system can be arranged in a stable configuration when connected to a high-Q resonant circuit [60].

The double-SQUID amplifier of the ROG Collaboration is made of a sensor d.c. SQUID, developed by the Institute of Photonic and Nanotechnologies of CNR, while the preamplifier SQUID is a commercial Quantum Design d.c. SQUID. The performances of the device are very good: with open input and open loop it exhibited [57] energy resolutions equal to $28\hbar$ at 4.2 K and $5.5\hbar$ at 0.9 K.

To avoid the instabilities that arise in d.c. SQUID devices connected to high-Q resonant input loads, it has been necessary to install a cold damping network [61].

The system has been succesfully tested with a high-Q^5 resonant input load in the temperature range 2 K-4.2 K. The device showed very good stability and it was possible to measure an energy resolution of about $70\hbar$ at 2 K, corresponding to a noise temperature $T_n \approx 6\mu$K to be compared to that of a single stage SQUID amplifier $T_n \approx 250\mu$K.

4.5.2 Parametric transducer

Most parametric transducers use a high–frequency resonator combined with a low–noise high–frequency amplifier. Figure 23 illustrates their basic structure. The parametric transducer illustrated uses a capacitor in a resonant circuit. The capacitance is modulated by the gap spacing between the ca-

---

[5] The parameters of the circuit are L_0=96 mH, Q_0=$0.7 \cdot 10^6$, k=0.38 and f_0= 1740 Hz

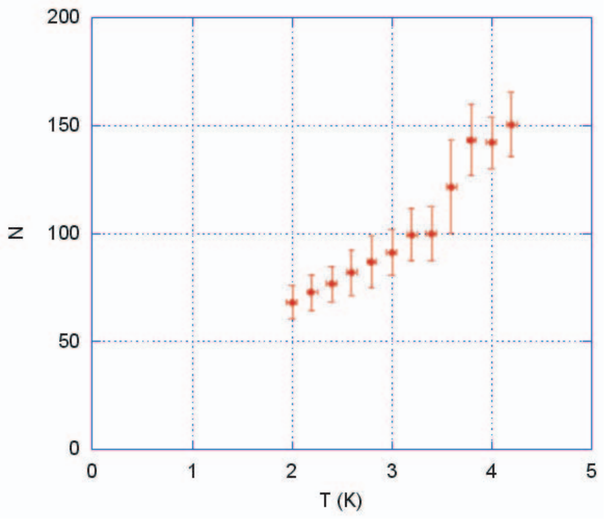

Figure 22: Energy resolution (expressed as number of $\hbar$) vs temperature.

pacitor and the antenna. The change in capacitance due to the motion modulates the resonant frequency of the circuit, creating modulation sidebands in the output signal.

One widely used form of high–frequency resonator is the capacity–loaded coaxial–line resonator or re–entrant cavity resonator. The re–entrant cavity is basically a lumped elements LC resonator, where the capacitance is determined by the spacing between the central post and the end wall of the antenna, and the inductance is mainly due to the central section of the cavity. Any change in the distance between the central post and the antenna modulates the capacitance of the cavity and, as a consequence, its resonant frequency, $\omega_a^2 = 1/(LC)$, producing sidebands in the pump signal which are displaced from the pump by the antenna frequency. These sidebands contain in their amplitude, phase and frequency the information about the external perturbation causing the vibration of the antenna.

One important difference between passive and parametric transducers is in the transducer impedance mismatch ratio or coupling factor β. For the parametric transducer

$$\beta_{para} = \frac{1}{2}\frac{CV_p^2 Q_e}{m\omega_a^2 x^2} \tag{65}$$

In the limit $Q_e > \omega_p/\omega_a$, the electrical quality factor of the resonator Q_e, is replaced by the ratio ω_p/ω_a.

For the passive capacitive transducer

$$\beta_{pass} = \frac{1}{2}\frac{CV^2}{m\omega_a^2 x^2} \tag{66}$$

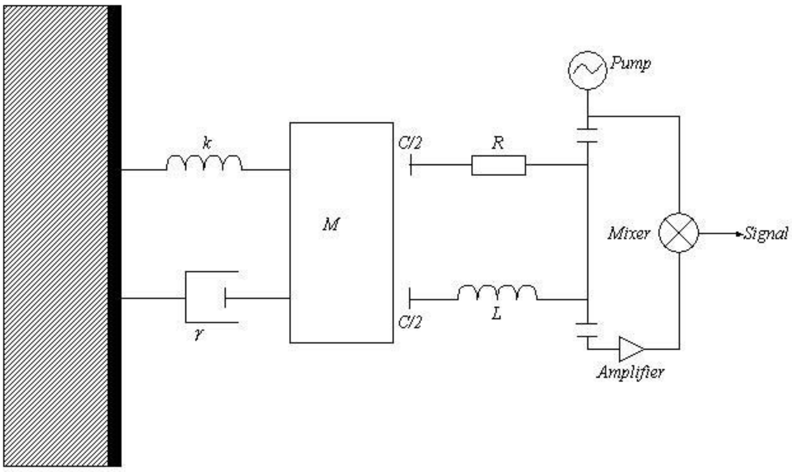

Figure 23: Schematic model of a resonant mass antenna with a parametric transducer. M is the effective mass of the antenna, $k = M\omega_a^2$ and $\gamma = M\omega_a/Q$ are respectively the elastic constant and the damping factor. C, L and R represent the lumped–elements resonant circuit.

Note that the passive transducer coupling factor is not enhanced by a Q–factor term.

Parametric transducer noise performance depends on the mechanical and electrical quality factor of the transducer structure. All types of transducers, both active and passive, are limited in noise performance by the noise of the amplifier with which they are used. In terms of noise number at 1 kHz a noise number of 1 corresponds to a noise temperature of about 50 nK, whereas at 5 GHz the same performance correspond to $T_n \simeq 0.3$ K. Amplifiers for microwave parametric transducers are available with $T_n \simeq 2$ K. Critical to achieving excellent amplifier noise is very low signal levels, requiring excellent carrier suppression, since otherwise pump power reflected from the cavity greatly exceeds the signal sidebands. Finally, a critical problem is phase noise in the pump oscillator.

Re-entrant cavity design

A first–generation re–entrant cavity transducer was designed, constructed and extensively tested at the University of Western Australia in Perth [62, 63, 64, 65, 66]. Another device of this kind is now being developed for the Brazilian spherical gravitational wave detector SCHEMBERG [67, 68].

Figure 24: A prototype of the re–entrant cavity transducer ready for testing. Note the clamps that keep the cavity tight onto the reference plane and the rf connectors that deliver the power and extract the signal. The cavity can be tested both in two–port configuration (transmission) and in one–port configuration (reflection).

In our design (see fig. 25) the cavity has a length $\ell = 5$ mm and radius $r_1 = 3$ mm. The central post has a conical section with end radius $r_0 = 0.5$ mm. High transducer sensitivity is obtained by usign a small value of the capacitance gap d. We choose $d \simeq 15$ μm. Finite element calculations gave the following values for the cavity operating parameters: resonant frequency (TEM mode) $\omega_a/(2\pi) = 5.5$ GHz, sensitivity $\Delta f/\Delta d \simeq 1.4 \times 10^{14}$ Hz/m. The cavity is pumped by an external ultralow phase noise source at its resonant frequency ω_a.

For a parametric transducer the sensitivity is proportional to $P_i Q_e^2$, where P_i is the input power and Q_e is the unloaded electromagnetic quality factor of the cavity. Since high values of the quality factor are desirable the cavity is made of niobium.

The quality factor is defined as

$$Q = \omega_a \frac{U}{P_d} \tag{67}$$

where U is the energy stored in the cavity and P_d is the overall dissipated power. Losses in the re–entrant cavity transducer are mainly due to niobium surface losses, to radiative losses and to losses in the external circuit.

Surface losses are given by the ratio between a geometric factor and the cavity surface resistance. The surface resistance is an intrinsic property of the cavity surface material dependent on frequency and temperature. It is

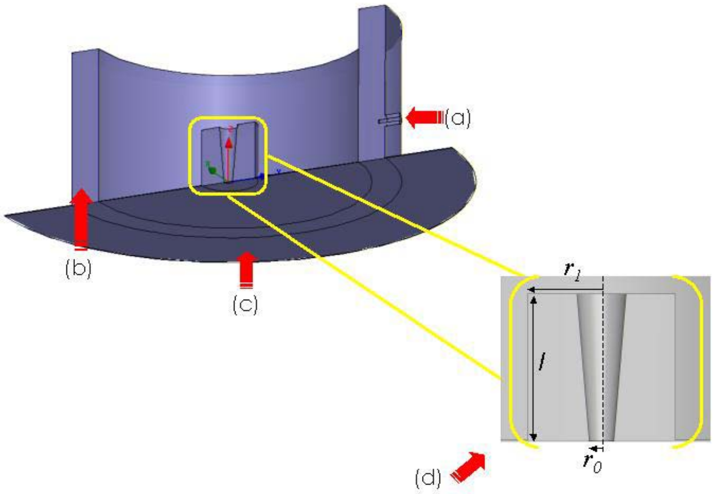

Figure 25: Schematic view of the re–entrant cavity. (a) The rf power is coupled through the choke, so that the effect of the coupling on the frequency and on the sensitive spot can be minimized. (b) Since the cavity is open, the chokes' shape and dimension are designed to minimize the radiated field, thereby preserving the electromagnetic quality factor. (c) The transducer oscillating mass will be made of niobium. The plate is *not* in contact with the cavity. (d) The cavity is designed to operate at $\omega_a/(2\pi) \simeq 5.5$ GHz. With an electromagnetic quality factor $Q_e \sim 10^8$ and an input power of 1 μW the electric field strength in the gap is $E_g \simeq 8$ MV/m.

given by the sum of two contributions: $R_s = R_{BCS} + R_{res}$. The intrinsic BCS term, strongly temperature dependent, may be calculated numerically from the general theory. At $f \simeq 5$ GHz and $T \simeq 0.1$ K, $R_{BCS} \ll 0.1$ nOhm. The residual losses depend on surface preparation and cleanliness. With standard surface preparation techniques residual resistance values $R_{res} \simeq 1$ nOhm have been obtained, which would give $Q_e \simeq 10^{10}$.

The external losses are usually parameterized defining a (coupling) coefficient $\zeta = Q_e/Q_{ext}$, so that

$$\frac{1}{Q} = \frac{1}{Q_e} + \frac{1}{Q_{ext}} = \frac{1+\zeta}{Q_e} \tag{68}$$

or

$$Q = \frac{Q_e}{1+\zeta} \tag{69}$$

When $\zeta = 1$ (critical coupling) the external losses equal the intrinsic losses. In this case the cavity input impedance is exactly matched with the input line impedance and no power is reflected back in the input line.

Radiation losses will also be present due to the small gap between the transducer and the antenna. In order to minimize them an rf choke was designed (see fig. 25). The choke consists in a short–circuited half–wavelength transmission line, tuned to the cavity operating frequency. The first quarter wavelength is a radial waveguide while the second quarter wavelength is a coaxial transmission line that is short–circuited at the bottom.

Read–out electronics The transducer is complemented with a feedback loop, which keeps the local oscillator on track with the cavity. As shown in fig. 26, the loop components are arranged in a phase comparator configuration, so that the output of the mixer is proportional to the phase difference between the rf generator signal (at angular frequency ω_{rf}) and the cavity output.

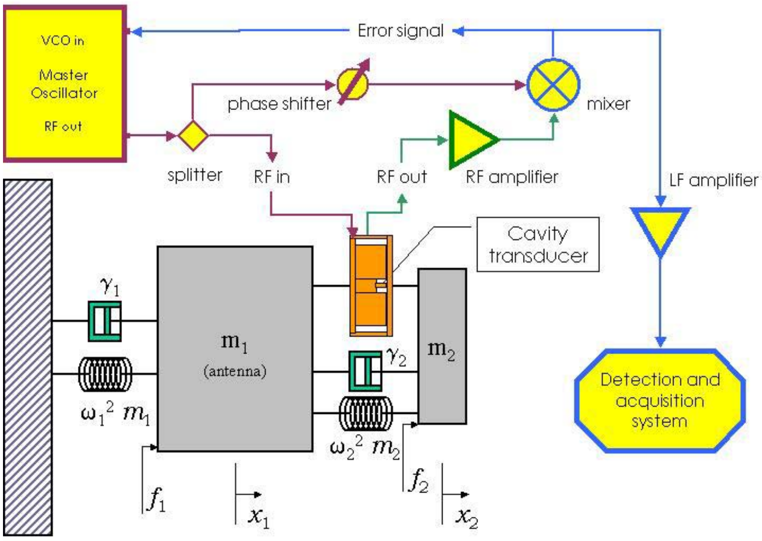

Figure 26: Detector conceptual layout. In the picture the resonant antenna, the secondary oscillator, the parametric transducer and the read–out circuit are represented.

The cavity output has the same instantaneous frequency as the rf generator signal, but it is phase-shifted of an amount which, near the cavity resonance, is linearly proportional to $\omega_{rf} - \omega_{cav}$, where ω_{cav} is the instantaneous resonator angular frequency[6] given by

$$\omega_{cav} = \omega_a \left(1 + \frac{1}{2}\, C\, \delta\right) \tag{70}$$

In this equation C represents the sensitivity of the cavity resonant frequency to a change in the gap dimension. It is given by

$$C = \frac{2}{\omega_a} \frac{\Delta\omega}{\Delta\delta} \tag{71}$$

and δ is the time–varying gap, which oscillates at the same angular frequency of the incoming gravitational wave (see eq. 127). ω_a is the unperturbed ($\delta = 0$) cavity resonant frequency. ω_{cav} strongly depends on the geometry of the cavity and is, by design, maximally sensitive to the gap distance.

The feedback circuit allows to keep the rf generator frequency tuned with the cavity instantaneous frequency by looping back the error signal coming from the mixer into the Voltage Controlled Oscillator (VCO). This error signal, properly amplified, carries the useful information on the GW. In the first order approximation, near the cavity resonant frequency, the error signal is given by

$$V_{err} = -2\, G_{rf}\, K_{mix}\, \tau\, K_{cav} \frac{\zeta}{(\zeta + 1)^2} \left(\omega_{rf} - \omega_{cav}\right) \tag{72}$$

where G_{rf} is the gain of the rf low–noise aplifier, K_{mix} is the mixer conversion loss, τ is the energy decay time of the superconducting cavity (see eq. 129), and ζ is the cavity coupling coefficient, given by the ratio between the the cavity input impedance and the circuit impedance. K_{cav} is a low–pass filter with cut–off frequency $1/(2\tau) = \omega_a/(2Q)$, which takes into account that the cavity filters out frequency components outside its bandwidth. For a stationary (linearized) solution, where $\delta(t) \propto e^{j\Omega t}$, sidebands appear in the field solution at frequencies $\omega_{rf} + \Omega$ and $\omega_{rf} - \Omega$. K_{cav} is therefore a function of the modulating frequency Ω.

Finally the VCO instantaneous frequency is given by

$$\omega_{rf} = \omega_{free} + K_{VCO}\, V_{err} \tag{73}$$

where ω_{free} is the generator free–running angular frequency (usually chosen to be $\omega_{free} = \omega_a$), and K_{VCO} is the VCO voltage–to–frequency conversion characteristic.

The feedback implementation is prone to two main noise sources, namely: the rf oscillator phase and amplitude noise and the amplifiers (rf and if) input

---

[6] It should be remarked that ω_{cav} is only the natural oscillation frequency of the resonator and, in general, it is different from ω_{rf}, which is frequency of the rf signal passing through the cavity. The unperturbed cavity is designed to have the natural oscillation frequency equal to ω_a.

noise. The rf amplifier is one of the most critical component in the loop, as its noise input level ultimately sets a limit on the sidebands amplitude detection. In few words, the cavity instantaneous frequency is modulated by the moving gap and therefore sidebands arise from the rf signal, with an amplitude roughly proportional to the frequency displacement causing the modulation $\Delta\omega$ divided by the modulating frequency: $A_{band} \propto \frac{\Delta\omega}{\Omega}$. To be detected, this amplitude must be greater than the rf amplifier input noise. We should note however that state–of–the–art, commercially available amplifiers can already provide near quantum–limited, cryogenic–operated devices ($T_n \simeq 2$ K, that is $\simeq 8\,\hbar$ @ 5 GHz).

The cavity is pumped through one port and read through the same port, that is through the reflected signal. If the electromagnetic coupling ζ to the cavity resonant mode is $\zeta \simeq 1$, then the reflected signal amplitude near resonance is nearly zero. In a real experimental condition, when ζ can be far from 1, one might need to provide a more complicated circuitry to suppress the strong reflected signal from the cavity entering the rf amplifier (carrier suppression interferometer [69]).

The feedback equations couple the rf oscillator frequency ω_{rf} with the masses position δ through the cavity instantaneous frequency ω_{cav}. For very high open-loop gain, the rf generator instantaneous frequency closely follows the cavity one. To extract the GW information one can use either the feedback error signal (whose typical frequencies are $\sim 10^3$ Hz) or the rf generator output ($\sim 10^9$ Hz). Both techniques are theoretically valid and the choice between them is a matter of experimental feasibility.

4.6 Data Acquisition System

4.6.1 Requirements

The aim of the Data Acquisition System (DAQ) is to provide a hardware/software environment basically dedicated to:

1. the digitization of the data collected from the transducer readout channels, the precise time determination of the sampled data and the organization of data into structures;
2. the logging of the data structures on permanent mass storage;
3. the sequencing of the operations related to data collection (run);
4. the collection and the execution of directives originated by remotely located users;
5. the notification of the working conditions, including the abnormal ones;

6. the execution of programs for monitoring the detector performances and the quality of data.

4.6.2 Architecture

The previuos tasks fit into a distributed computing system since time critical processes associated to them (e.g. task 1) cannot be interrupted by external conditions. This requirement leads to the assignment of time critical processes to a dedicated processor. The DAQ architecture (Fig. 27) includes a board computer (Host A) that performs time critical tasks, namely the the readout of the digitization electronics via VMEbus, the organization of data into structures and the transmission of data on the network. A second computer (Host B) receives data and logs them on disks. Information related to user directives, to the synchronization and status of operations and to abnormal conditions are shared among Host A and Host B by message exchange on the network. Host B provides also the collection of user directives and the display of control information via remote graphical user interface (GUI). The monitoring of the detector performances based on the online data preanalysis is performed on Host B.

The designated operating system for the implementation of the architecture is Linux, which is supported on a wide range of platforms, insuring processor cross-operability in a distributed environment. Moreover, a consequence of this choice is that the extensive availability of archived and supported freeware/shareware software can be helpful in the realization of the architecture.

4.6.3 Hardware components

The first choice for Host A is an Intel Pentium III processor-based VME single board (SBC) belonging to the General Electric (GE) VMIVME-7750 family (1.26 GHz, 512 MB), which is equipped with a high-performance PCI-to-VME interface and has the capability of operating as a VME crate controller. SBC is complemented by a VMEbus IDE hard disk drive module (GE VMIVME-7459) connected via the VMEbus P2 lines.

The digitization of the transducer readout channels is performed by a GE VMIVME-3123 analog input board, which provides the analog-to-digital conversion of up to 16 input channels with conversion rates of up to 1.6 Msample/s (100kHz/channel). Each input is equipped with a dedicated sample-and-hold amplifier and a 16-bit A/D converter. Digitized samples are accumulated in a data buffer until retrieved by SBC on the VMEbus. Buffer size is software controlled from one sample to 4 Msample.

The sampling clock for the 3123 module is provided externally by an Elsat GPS2000 receiver and time/frequency source. This module is equipped with an internal quartz oscillator generating a 10 MHz waveform. The

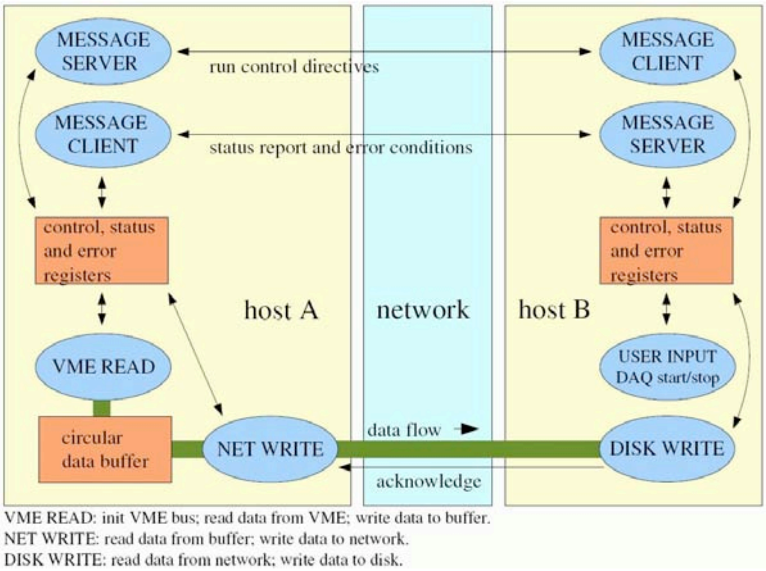

Figure 27: *DAQ general architecture*

frequency is down scaled to the region of $\sim$ 10 kHz by an external frequency divider module housed in the VME crate. The reference time is given by the GPS2000 module via the internal GPS receiver, insuring a frequency stability of the 10 MHz waveform less then 1 10^{-12}. The module provides a reference output for the standard time in form of one pulse per second with an accuracy of the front edge of $<$ 200 ns against UTC. The front edge of the pulse is sensed by a Caen VME-V977 Input/Output Register, which gives the general synchronization of the readout channel sampling activity with the standard time.

The collection of environmental data (e.g. seismic data, thermometry, etc.) is performed by a GE VMIVME-3125 module, which provides a 12-bit analog-to-digital conversion for 32 analog voltage input channels. Measurement data for each channel is constantly available to the VMEbus through a dual-ported Data Register.

Host B is a standard dual CPU Pentium processor.

The data logging throughput is dominated by the digitization of the readout channels: about 120 kB/s are generated for a sampling frequency of 10 kHz per channel. This corresponds to about 4 TB/year of uncompressed data to be logged on disk and leads to the inclusion of a (redundant) disk server in the acquisition system network.

4.6.4 Software components

The data acquisition software is written using the C programming language and compiled with the freely distributed GNU compiler. Besides standard libraries included in the compiler software, a set of additional libraries, provided by the VMEbus hardware vendor, are used to interface the experiment electronics with the acquisition software itself. The data and message exchange between Host A and Host B is performed through network sockets. On both computers the main acquisition program tasks are distributed between concurrent threads, each carrying on an independent job asynchronously but always sharing information with the other threads via a common control and status register. A circular buffer for temporary storage of acquired data is implemented on Host A in order to cope with CPU, network and disk latency times.

We chose to use the ROOT data analysis framework for data presentation and preanalysis. This software is largely used in the HEP community and offers great flexibility for a wide range of applications. One of the features we plan to use is the possibility of having a histogram server (on Host B in our case) capable of creating histograms and distributing them on the network.

Data acquisition control also is requested to be performed from remote stations. A web based GUI, allowing remote interaction with the DAQ, will be implemented together with an authentication system and a locking mechanism preventing uncontrolled interaction with the DAQ system.

4.7 Expected sensitivity

The expected sensitivity for a 2 meter sphere is shown in Fig. 28 and 29. The two curves represent the sensitivities that can be achieved with a read-out at $20\hbar$ and at the quantum limit respectively.

In conclusion, a spherical resonant-mass detector with the specification proposed, will reach, in a first stage of operation, a sensitivity about equal to that of a large scale interferometer such as VIRGO or LIGO, in their initial configuration, over the frequency range $900\,\mathrm{Hz} < f < 1100\,\mathrm{Hz}$. In the final configuration, it will reach over the same frequency window a sensitivity $S_h^{1/2}(f) = 3 \times 10^{-23}\,\mathrm{Hz}^{-1/2}$, approximately equal to the projected sensitivity of Advanced LIGO or Advanced VIRGO.

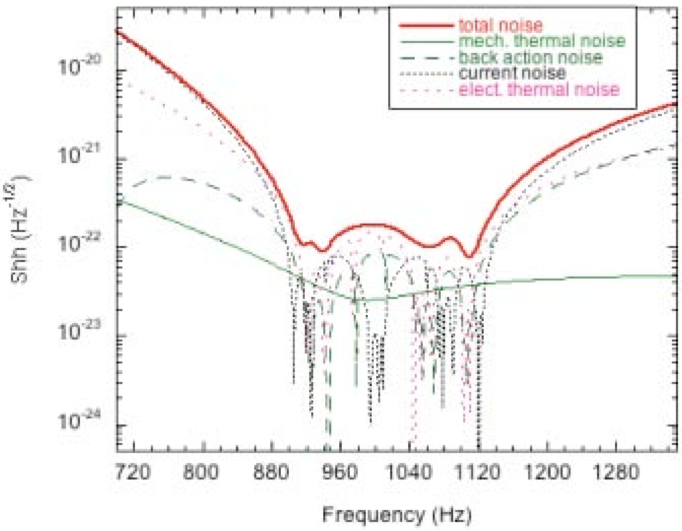

Figure 28: Calculated strain noise spectrum for a 2 meter diameter CuAl sphere. The sphere is equipped with six transduction chains in the TIGA configuration, with a read-out at $20\hbar$.

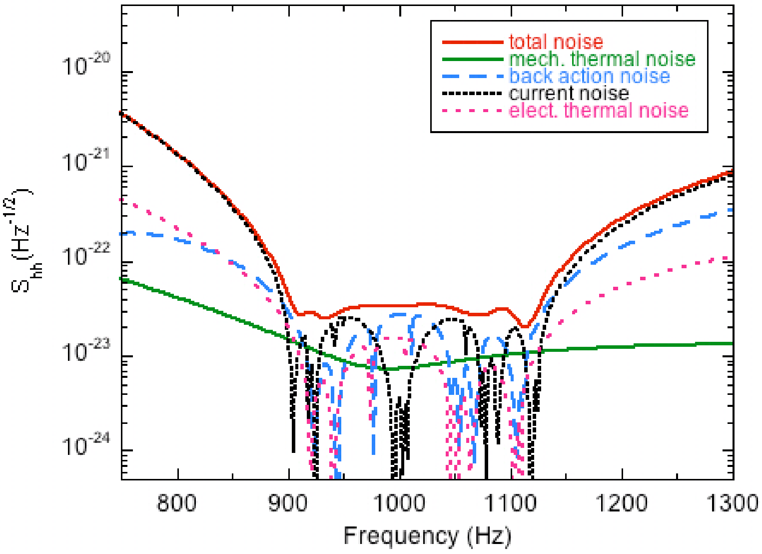

Figure 29: Calculated strain noise spectrum for a 2 meter diameter CuAl sphere. The sphere is equipped with six transduction chains in the TIGA configuration, with noise at quantum limit.

5 Astrophysics with a spherical gravitational wave detector

The existence of GWs is demonstrated by 20 years of observation of the binary pulsar PSR 1913 + 16 [74]. Today, the interest of GW research is to use them as a probe of astrophysics and possibly cosmology. In this section we discuss some of the most interesting sources that can be searched, using a resonant spherical detector, with the characteristic specified in Sect. 4. We will discuss both the results that can be obtained at an initial stage, taking as reference value a strain sensitivity $S_h(f) \simeq 3 \times 10^{-22}\,\mathrm{Hz}^{-1/2}$ over a frequency range $900\,\mathrm{Hz} < f < 1100\,\mathrm{Hz}$, and our final target,

$$S_h(f) \simeq 3 \times 10^{-23}\,\mathrm{Hz}^{-1/2}\,, \tag{74}$$

again over the range

$$900\,\mathrm{Hz} < f < 1100\,\mathrm{Hz}\,. \tag{75}$$

Throughout this discussion we make use of the fact that the energy signal-to-noise ratio (SNR) of the output, after optimal filtering, is given by the well-known formula

$$\mathrm{SNR} = 4\int_0^\infty \frac{|\tilde{h}(f)|^2}{S_h(f)}df, \tag{76}$$

where $\tilde{h}(f)$ is the Fourier transform of $h(t)$ and $S_h(f)$ the (single-sided) spectral density of the signal.[7] We now discuss the SNR of this spherical resonant detector for various gravitational wave signals.

5.1 Burst sources

A number of astrophysical phenomena, like supernova explosions or the final merging of a neutron star-neutron star binary system, can liberate a large amount of energy in GWs in a very short time, typically less than a second, and sometimes as small as a millisecond. We will refer to such signals as GW bursts, and we denote their duration by τ_g. In Fourier space, a GW burst therefore has a continuum spectrum of frequency over a broad range, up to a maximum frequency $f_{\max} \sim 1/\tau_g$.

In principle, if we know the form of $\tilde{h}(f)$, we can just plug it into eq. (76) to obtain the SNR for a given noise spectral density of the detector. However, bursts come from explosive and complicated phenomena, and it is very difficult to predict accurately their waveform. We can however make some simple order-of-magnitude estimates, observing that, with a bandwidth $\Delta f \sim 200$ Hz and a central frequency $f_0 \simeq 1$ kHz, we have $\Delta f/f_0 \simeq 0.2$, so the Fourier components of $\tilde{h}(f)$ are not expected to change much, while

---

[7] An equivalent form is $\mathrm{SNR} = \int_{-\infty}^{\infty} \frac{|\tilde{h}(f)|^2}{S_h(f)}df$, where $S_h(f)$ is the *single-sided* spectral density.

$S_h(f)$ is also quite flat in this window, see Fig. 29. Then in the integrand in eq. (76) we can approximate $\tilde{h}(f)$ with $\tilde{h}(f_0)$ and $S_h(f) \simeq S_h(f_0)$, and eq. (76) becomes

$$\mathrm{SNR} \simeq 4|\tilde{h}(f_0)|^2 \, \frac{\Delta f}{S_h(f_0)} \,, \tag{77}$$

The energy radiated in GWs during a burst can be estimated in terms of $\tilde{h}(f_0)$, assuming a flat spectrum up to a maximum frequency $f_{\rm max}$, and is given by

$$\Delta E_{\rm rad} \simeq \frac{4\pi^2 r^2 c^3}{3G} |\tilde{h}(f_0)|^2 \, f_{\rm max}^3 \,, \tag{78}$$

where r is the distance to the source. Combining eqs. (77) and (78) we get, at SNR=1,

$$r \simeq 18\,\mathrm{Mpc} \left(\frac{3 \times 10^{-23}\,\mathrm{Hz}^{-1/2}}{S_h^{1/2}(f_0)} \right) \left(\frac{\Delta E_{\rm rad}}{10^{-2} M_{\odot} c^2} \right)^{1/2} \left(\frac{\Delta f}{200\,\mathrm{Hz}} \right)^{1/2} \left(\frac{1\,\mathrm{kHz}}{f_{\rm max}} \right)^{3/2} . \tag{79}$$

This equation gives an estimate of the maximum distance r at which we can detect a burst source which radiates and energy $\Delta E_{\rm rad}$ in gravitational waves, with a detector having a strain sensitivity $S_h(f)$ over a bandwidth Δf, and is the basic equation that allows us to estimate our sensitivity to GW bursts. We now apply it to discuss the detectability of various possible burst sources.

Binary Coalescence. Binary systems made by two neutron stars (NS-NS), or by two black holes (BH-BH) or by a neutron star and a black hole (NS-BH) are among the most interesting sources that can be searched in GW experiments.

The gravitational radiation emitted by these systems sweeps up in frequency, until the two objects coalesce. In the Newtonian approximation the relation between the frequency f of the GWs emitted and the time to coalescence, τ, is

$$f(\tau) \simeq 134\,\mathrm{Hz} \left(\frac{1.21 M_{\odot}}{M_c} \right)^{5/8} \left(\frac{1\,s}{\tau} \right)^{3/8} , \tag{80}$$

where $M_c = (m_1 m_2)^{3/5} (m_1 + m_2)^{-1/5}$ is the so-called chirp mass of a binary system with masses m_1, m_2. The reference value $M_c = 1.21 M_{\odot}$ corresponds to a binary system of two stars with $m_1 = m_2 = 1.4 M_{\odot}$, typical of neutron stars. Formally eq. (80) states that the GW signal enters in our frequency band, $f > 900$ Hz, when the time to coalescence is $\tau = 6$ ms. At this stage, the Newtonian and pointlike approximation used to derive eq. (80) becomes invalid, so the precise number cannot be trusted. In any case, the conclusion is that the inspiral phase is not accessible to our detector, and we are instead sensible to the final plunging and merging phase. Therefore, in our detector, the binary inspiral is seen as a burst signal.

The energy radiated during the final merging phase of a NS-NS system is rather reliably estimated to be of order

$$\Delta E_{\rm rad} \sim 10^{-2} M_{\odot} c^2 \,. \tag{81}$$

On the other hand, the coalescence rates are more uncertain. Before the recent discovery of a new NS-NS binary [36], the rate of NS-NS coalescences in the Galaxy was estimated to be in the range 10^{-6} to 5×10^{-4} mergings per year [35]. This estimate depends strongly on the shortest-lived systems known, and the recent discovery of a new NS-NS binary, with the shortest known merging time (85 Myr), brings this estimate up by one order of magnitude [36].

Equation (79) indicates that, given the value (81) for $\Delta E_{\rm rad}$, and using our final target sensitivity, we can detect a NS-NS coalescence up to a distance of order

$$r \sim 18\,{\rm Mpc}\,. \tag{82}$$

In particular, we can detect a NS-NS coalescence in the Virgo cluster, $r \sim 15 - 20$ Mpc; given that in the Virgo cluster there are over 2000 galaxies (including giant galaxies), the expected rate at this distance can be estimated between 2×10^{-2} and $O(1)$ events per year.

These numbers are however quite uncertain, since they depend strongly on the lifetime of the system with the shortest known merging time. As we have already seen, the discovery of just one system with the shortest known merging time can bring these estimates to substantially higher values.

The final stage of the coalescence of BH-BH and BH-NS binary system will produce a signal in our bandwidth if the BH is of the order of $1 - 2M_{\odot}$ (for higher-mass BHs, the maximum frequency radiated in the merging phase becomes lower than 900 Hz), and its intensity is of the same order as for NS-NS. The rates of BH-BH and BH-NS coalescence are very uncertain, since, contrarily to NS-NS binary, no such system has yet been observed. Estimates based on population synthesis suggest that their rate should be comparable, or somewhat lower, than NS-NS coalescences.

Black hole formation. It has been shown that a spherical detector is a very interesting instrument for observing the formation of black holes [76]. When a binary whose total mass M is greater than the maximum neutron star mass coalesces the likely outcome is a mass M black hole. The excitation of fundamental quadrupole mode of the resulting black hole generates gravitational waves with a typical frequency of

$$f \simeq 12\,{\rm kHz} \left(\frac{{\rm M}_{\odot}}{M} \right) , \tag{83}$$

lasting for a few cycles. For Schwarzschild black holes, a typical spherical antenna is sensitive to formation of black holes with mass of the order of 10 $M_\odot$, which are known to exist. For instance the estimated mass of Cygnus X-1 and LMC X-3 are in that range. Assuming an energy conversion efficiency of the black hole mass into gravitational waves of 10^{-4}, the signal-to-noise ratio of Schwarzschild black hole formation in the typical detector is thus given by[82]

$$\mathrm{SNR} \simeq \left(\frac{50\,\mathrm{Mpc}}{r}\right)^2 \left(\frac{M}{15\,\mathrm{M}_\odot}\right)^3 \left(\frac{3\times 10^{-23}\,\mathrm{Hz}^{-1/2}}{S_h^{1/2}(f)}\right)^2 . \qquad (84)$$

Even under the pessimistic assumption that there is no increase in efficiency for the coalescence of orbiting black holes, our reference antenna is expected to observe a typical $15\,\mathrm{M}_\odot$ black hole formation event out to tens of Mpc, and in particular in the Virgo cluster.

There is one additional reason why a spherical detector is very interesting for observing sources such as a gravitational collapse. Since in General Relativity no gravitational wave is radiated from a spherically symmetric collapse, we cannot obtain any information if collapses are spherically symmetric. However, in scalar-tensor theories scalar waves are radiated even from a spherically symmetric collapse. These scalar gravitational waves can be detected very naturally by observing the excitation of the monopole and the $\ell = 2, m = 0$ quadrupole modes of a sphere, which are not excited by the tensor waves of General Relativity. It is also expected that the scalar waves reflect directly the stellar initial radius, mass, and density [83].

Supernova explosions. Current estimates of the energy radiated in GWs in a type II supernova explosion range between $10^{-2}M_\odot c^2$ and $10^{-6}M_\odot c^2$, depending mainly on the deviation from sphericity of the collapse. From eq. (79) we see that, at the initial sensitivity, we can detect a SN explosion out to a distance of 1.8 Mpc for the optimistic case $\Delta E_{\rm rad} = 10^{-2}M_\odot c^2$ and 18 kpc for $\Delta E_{\rm rad} = 10^{-6}M_\odot c^2$.

At the advanced level we get 18 Mpc for $\Delta E_{\rm rad} = 10^{-2}M_\odot c^2$ and 180 kpc for $\Delta E_{\rm rad} = 10^{-6}M_\odot c^2$. A collapse taking place in the Virgo cluster of galaxies, at $r \sim 15 - 20$ Mpc (where the expected rate is of order of several events per year) will be detected if it radiates about 2×10^{-2} solar masses.

A supernova in our Galaxy (say at $r = 10$ kpc, expected rates of orders one every $\sim$ 40 yr) would be seen with a signal-to-noise ratio (in energy) SNR $\sim 10^7$ for $\Delta E_{\rm rad} = 10^{-2}M_\odot c^2$ and SNR $\sim 10^3$ for $\Delta E_{\rm rad} = 10^{-6}M_\odot c^2$. In the Local Group of galaxies (say, $r < 600$ kpc, rates or order 1 every 10-20 yr) an event with $\Delta E_{\rm rad} = 10^{-2}M_\odot c^2$ would be seen with SNR ~ 25.

Starquakes, Soft Gamma Repeaters, and Magnetars. Our target sensitivity allows us to explore extragalactic distances in search of rare events, such as supernova explosion or NS-NS coalescence, that liberate huge amounts of energy. On the other hand, this sensitivity also allows us to explore our Galaxy, in search of events which are less dramatic, but hopefully much more common on the galactic scale.

In particular, neutron stars (as well as hypothetical compact objects such as quark stars, or neutron stars with a core of deconfined quark matter), can produce GW bursts as a consequence of sudden rearrangements of their structure, either in the crust or in the core. Crustquakes can liberate in GW an energy

$$\Delta E_{\rm rad} \sim (10^{-10} - 10^{-8})\, M_{\odot} c^2\,, \tag{85}$$

while even larger values can be obtained in corequakes (see [37] and references therein).

A very interesting example of this phenomenon is provided by magnetars, which are neutron stars with huge magnetic fields, of order $10^{14} - 10^{15}$G [38, 39], i.e. 100 to 1000 times stronger than in ordinary pulsars. It is believed that magnetars provide an explanation for the phenomenon of soft gamma repeaters (SGR), x-ray sources with a persistent luminosity of order $10^{35} - 10^{36}$ erg/s, that occasionally emit huge bursts of soft γ-rays, with a power up to 10^{42} erg/s, for a duration of order 0.1 s. The mechanism invoked to explain the burst activity is that the magnetic field lines in magnetars drift through the liquid interior of the NS, stressing the crust from below and generating strong shear strains. For magnetic fields stronger than about 10^{14} G, these stresses are so large that they cause the breaking of the 1 km thick NS crust, whose elastic energy is suddenly released in a large starquake, which generates a burst of soft gamma rays. Such starquakes can radiate in GWs an energy $\Delta E_{\rm rad} \sim 10^{-10} - 10^{-9} M_{\odot} c^2$ [40, 41, 37]. Occasionally SGRs emit truly giant flares, and in this case the estimate for the energy radiated can be $10^{-8} M_{\odot} c^2$ or even larger [42].

Magnetars are just one example of objects which could emit GW bursts at this level, and a number of variants have been considered [37]. For instance the rearrangement in the internal structure of the star could be triggered by accretion, rather than by the magnetic field, or the emission could be related to phase transition in the core of a hybrid quark-hadron star [43]. While the rigidity of the crust is determined by the Coulomb interaction between nuclei, in the core the relevant energy scale is determined by hadronic physics, so corequakes could be a much more powerful source of GWs than crustquakes (see also Ref. [41]).

At our initial sensitivity, eq. (79) indicates that a GW burst that liberates in GWs an energy $\Delta E_{\rm rad} = 10^{-8} M_{\odot} c^2$ can detected up to a distance $r \sim$ 3 kpc. At our final target sensitivity, for $\Delta E_{\rm rad} = 10^{-8} M_{\odot} c^2$ we reach $r \sim 33$ kpc, that is, we can explore all the Galaxy. A burst taking place at the distance $r = 100$ pc, corresponding to the distance to the closest observed neutron stars, will be detectable if it radiates $\Delta E_{\rm rad} = 10^{-11} M_{\odot} c^2$

for our initial sensitivity and $\Delta E_{\rm rad} = 10^{-13} M_{\odot} c^2$ for our final sensitivity. Observe that, while the closed *observed* NS is at about 100 pc, population synthesis calculation indicates that the NS closest to us should be at just 5-10 pc, and that in a sphere of radius 100 pc around the Sun, there should be $O(10^4)$ neutron stars [44].

Finally, it is interesting to observe that these "small" bursts do not destroy the source, but leave it in the condition of flaring again. As observed experimentally in the bursts of soft γ-rays in magnetars, the events coming from such sources have a very characteristic distribution in energy spectrum and in waiting time (the time between one outburst and the next), that would provide a clear experimental signature [48].

5.2 Periodic sources

Neutron stars have in general deviation from spherical symmetry, which are typically generated when they cool down and their crust solidifes. In a rotating NS these deviations from spherical symmetry produce a time-varying quadrupole moment and therefore generate a periodic GW signal, at a frequency f_0 equal to twice the rotational frequency $f_{\rm rot}$.[8] The resulting GW amplitudes, for the + and × polarizations, are

$$\begin{aligned} h_+ &= h_0 \, \frac{1+\cos^2\iota}{2} \, \cos\left[2\pi f_0 t\right] && (86) \\ h_\times &= h_0 \, \cos\iota \, \sin\left[2\pi f_0 t\right] && (87) \end{aligned}$$

where ι is the inclination of the rotation axis with respect to the line of sight and

$$\begin{aligned} h_0 &= \frac{4\pi^2 G}{c^4} \, \frac{I_{zz} f_0^2}{r} \, \epsilon \\ &\simeq 1.06 \times 10^{-25} \left(\frac{\epsilon}{10^{-6}}\right) \left(\frac{I_{zz}}{10^{38}\,{\rm kg\,m}^2}\right) \left(\frac{10\,{\rm kpc}}{r}\right) \left(\frac{f_0}{1\,{\rm kHz}}\right)^2 . \quad (88) \end{aligned}$$

Here G is Newton's constant, I_{zz} the zz component of the moment of inertia tensor, and ϵ is the ellipticity of the star, which measures its deviation from sphericity.

The equilibrium values of the mass and of the radius of NS are fixed by the equation of state and, with all realistic equations of state, I_{zz} cannot differ much by the reference value used in eq. (88). The main source of uncertainty is instead due to the ellipticity ϵ. Plausible theoretical values are $\epsilon \lesssim 10^{-6}$, although values as large as $\epsilon \simeq 10^{-5}$ can be obtained.

---

[8] If the angular momentum of the NS is not aligned with a principal axis of the crust, there is also a precession motion at frequency $f_{\rm prec}$, and GWs are emitted, besides at $f_0 = 2 f_{\rm rot}$, also at $f_0 = f_{\rm rot} + f_{\rm prec}$. Since $f_{\rm prec} \ll f_{\rm rot}$, we basically have two lines at $f_0 = f_{\rm rot}$ and at $f_0 = 2 f_{\rm rot}$.

The fastest spinning NS are millisecond pulsar. In particular, a pulsar with a period of about $\tau \simeq 2$ ms, and therefore $f_{\rm rot} \simeq 500$ Hz, emits GWs at $f_0 \simeq 1$ kHz, in our bandwidth. Equation (88) shows that the GW amplitude h_0 increases as f_0^2, and therefore the signal from fast spinning pulsars is strongest, and the kHz region is a particularly interesting region for detection.

To extract the small GW signal from the background, one must integrate it for a time as long as possible. The Fourier transform of such a long stretch of data should then show a monochromatic line emerging from the background, in correspondence to the GW frequency. Ideally, if one had a stretch of data of length T (e.g. $T = 1$ yr), one could perform a single FFT on the data and search for monochromatic lines. Then, using the explicit form of the signal given in eqs. (86)-(88) and plugging it into the general formula (76) for the signal-to-noise ratio, one can show that, at SNR $= 1$, we can detect a pulsar with ellipticity ϵ, in an observation time T, up to a distance r given by

$$r = 2.5\,{\rm kpc}\left(\frac{3\times 10^{-23}\,{\rm Hz}^{-1/2}}{S_h^{1/2}(f_0)}\right)\left(\frac{T}{3\times 10^{7}\,{\rm s}}\right)^{1/2}\left(\frac{\epsilon}{10^{-8}}\right)\,, \qquad (89)$$

where we used the standard value $I_{zz} = 10^{38}\,{\rm kg\,m}^2$ and we set the GW frequency $f_0 = 1$ kHz. The reference value chosen for T corresponds to 1 yr of data.

Unfortunately, the above result only holds for *coherent searches*, i.e. if we have a single continuous stretch of data of length T, on which we apply a single Fast Fourier Transform (FFT). More generally, our data will be divided into shorter continuous stretches of data. In each stretch we can perform an FFT, and the result of the different FFTs can then be added incoherently. In particular, if the total integration time T is divided into $\mathcal{N}$ observation period of length Δt, with $T = \mathcal{N}\Delta t$, one finds that the sensitivity to the GW amplitude is reduced by a factor $\mathcal{N}^{1/4}$ with respect to the sensitivity of coherent searches, and eq. (89) becomes

$$r = \frac{2{\rm kpc}}{\mathcal{N}^{1/4}}\left(\frac{3\times 10^{-23}\,{\rm Hz}^{-1/2}}{S_n^{1/2}(f_0)}\right)\left(\frac{T}{3\times 10^{7}\,{\rm s}}\right)^{1/2}\left(\frac{\epsilon}{10^{-8}}\right)\,. \qquad (90)$$

The reasons that force us to divide the integration time into $\mathcal{N}$ shorter stretches are both of practical and of fundamental nature.

(1) From the practical point of view, data taking is interrupted periodically, either because of period of higher noise or, at the latest, because of cryogenic maintenance operations.

(2) At a more fundamental level, there is a relative motion of the detector and the star, due to the Earth rotation and revolution around the Sun, which produces a Doppler broadening of the spectral line, and also the signal is

not perfectly monochromatic, because of intrinsic changes in the frequency of the source, such as those due to pulsar spindown. Unless one corrects for these effects, it becomes useless to integrate for long times. In particular, the Doppler correction depends on the position of the source and therefore the data analysis and, as we will see, the sensitivity, differs depending on whether we are targeting a known pulsar, for which we know the position and the spindown parameters with good accuracy, or whether we are performing a blind all-sky survey. We examine the two cases separately.

Search for known fast-spinning pulsars. In this case, we usually know with a sufficient accuracy the position, as well as a number of parameters that describe the intrinsic spin drift of the source, and we can simply apply the appropriate corrections for Doppler shift and spindown. In this case the main limitation on continuos data taking will be due to practical factors such as maintenance operations. Assuming that one year worth of data are split into $O(50)$ continuos data taking period of one week, we only lose a factor $\sim 50^{1/4} \sim 2.6$ compared to the estimate for coherent searches and, assuming a total integration time $T \sim 3 \times 10^7\,$s, eq. (90) gives

$$r \simeq 1\,\mathrm{kpc} \left(\frac{3 \times 10^{-23}\,\mathrm{Hz}^{-1/2}}{S_h^{1/2}(f_0)} \right) \left(\frac{\epsilon}{10^{-8}} \right) . \tag{91}$$

This means that, at our final target sensitivity, we can detect a known millisecond pulsar at $r = 1$ kpc as long as its ellipticity ϵ is larger than 10^{-8}, and a known millisecond pulsar at $r = 10$ kpc as long as $\epsilon > 10^{-7}$. [9]

Blind all-sky searches. A blind search for pulsars all over the sky is in principle of the greatest interest. Electromagnetic observations only allow us to detect a tiny fraction of the existing neutron stars. As already mentioned above, the closed observed NS is at about 100 pc, while it is estimated that the actual closest NS should be at just 5-10 pc, and that in a sphere of radius 100 pc around us, there should be $O(10^4)$ neutron stars. In the Galaxy, it is estimated that there are $O(10^7)$ neutron stars, while only about 2000 are detected electromagnetically, as pulsars beamed toward us.

The difficulty of such a blind search is that the Doppler correction depends on the unknown position of the star in the sky, and on its unknown spin-down parameters. We therefore have a multidimensional parameter space (for fast pulsar, three spindown parameters are usually required, plus the position in the sky). We must discretize it, and apply the correction

---

[9] This is approximately a factor of 2 better than what could be achived with one interferometer having the same value of $S_h^{1/2}(f_0)$. The reason is that at an interferometer there is also an amplitude modulation due to the fact that, following the Earth rotation and revolution, the orientation of the interferometer with respect to the source changes, and the detector will be at times oriented unfavorably with respect to the source. Instead we have seen that the sphere, combining its five output channels, is an omnidirectional detector, so it is always well oriented with respect to the source.

separately for each point of this discretized parameter space, which means that we must perform a different FFT for each point in parameter space. If we increase the integration time T, we need also a finer mesh in this parameter space, in order to take advantage of the longer integration time. As a result, a coherent blind all-sky search quickly exceeds any present and forseeable computer capability, if T becomes too large. For fast pulsars it is estimated that, even on a Teraflop computer, a blind coherent all-sky search cannot be performed on a stretch of data longer than $T \simeq 18$ days [45].

The solution is then to split the data into $\mathcal{N}$ stretches and to add them incoherently, paying a factor $\mathcal{N}^{1/4}$ in sensitivity. The simplest (although not optimal) strategy is to divide the data in stretches of length ~ 30 min, since in this case no correction needs to be applied (the Doppler effect due to the Earth spin is the first effect to become important and, for $f_0 = 1$ kHz, it becomes important after an integration time $T \simeq 80$ min). One year worth of data will then be split in $\mathcal{N} = 1$ yr/(30min) $\simeq 1.7 \times 10^4$ stretches, and $\mathcal{N}^{1/4} \sim 11$. We therefore lose about one order of magnitude in sensitivity, compared to the search for known pulsars.

This means that, at our final target sensitivity, we can detect, in a blind all-sky search, a pulsar at $r = 1$ kpc as long as its ellipticity ϵ is larger than 10^{-7}, and at $r = 10$ kpc as long as $\epsilon > 10^{-6}$.

With this sensitivity, assuming a reasonable neutron star distribution in space and in frequency, we can expect to detect several sources in one year observation time [76].

5.3 Stochastic backgrounds

Stochastic backgrounds of GWs can result either from the incoherent superposition of many astrophysical sources which are not resolved individually, or from processes taking place in the early Universe. Examples of the latter phenomenon is provided by the amplification of vacuum fluctuations during transitions between different cosmological epochs (e.g. a transition between an inflationary phase and the radiation dominated era) or first order phase transitions taking place in the early Universe.

The intensity of a stochastic background of GWs can be characterized by its energy density per unit logarithmic interval of frequency, $d\rho_{\rm gw}/d\log f$, normalized to the critical density for closing the Universe, ρ_c,

$$\Omega_{\rm gw}(f) \equiv \frac{1}{\rho_c}\,\frac{d\rho_{\rm gw}}{d\log f}\,. \qquad (92)$$

The critical density is $\rho_c = 3H_0^2/(8\pi G)$, where $H_0 = h_0 100\,{\rm km}/({\rm sec\,Mpc})$ is the Hubble expansion rate and $h_0 \simeq 0.7$ parametrizes the experimental uncertainty on H_0. Actually, it is conventional to use the quantity $h_0^2\Omega_{\rm gw}$ rather than $\Omega_{\rm gw}$, in order to get rid of the uncertainty in h_0.

Various upper limits are known on $\Omega_{\rm gw}$, from different type of observations. In our frequency window (and in general in the whole frequency window accessible to ground based detectors) the strongest bound comes from primordial nucleosynthesis, and gives [2]

$$h_0^2 \Omega_{\rm gw}(f) < 10^{-5} \,. \tag{93}$$

Observe however that this bounds applies only to GWs produced before nucleosynthesis, i.e. in the early Universe, and not to backgrounds of astrophysical origin. Using a single detector, whether a bar or an interferometer, the minimum detectable value of $h_0^2 \Omega_{\rm gw}$ is [2]

$$h_0^2 \Omega_{\rm gw}^{\rm min}(f) \simeq \frac{1}{F} \cdot 10^{-2} \left(\frac{f}{100 {\rm Hz}} \right)^3 \left(\frac{S_h^{1/2}(f)}{10^{-22} {\rm Hz}^{-1/2}} \right)^2 \,, \tag{94}$$

where F is an angular efficiency factor which depends on the detector geometry. One has $F = 2/5$ for an interferometer, and $F = 2/5$ also for each of the five quadrupolar modes of a resonant sphere.

From this we see that both our resonant sphere, at its target sensitivity, and advanced VIRGO (or advanced LIGO), used as single detectors, are far from a really interesting sensitivity to stochastic backgrounds. In the kHz region, both the sphere and advanced VIRGO (or advanced LIGO), used as single detectors, can reach at most $h_0^2 \Omega_{\rm gw} = O(1)$. Advanced VIRGO or Advanced LIGO have their best sensitivity around $f = 200$ Hz, where anyway they cannot go below $h_0^2 \Omega_{\rm gw} = O(10^{-3} - 10^{-4})$. [10]

The situation however changes drastically if we correlate the outputs of two detectors. In this case, if the two detectors are sufficiently close (that is, their separation is not large with respect to the wavelength of the GWs that one is searching), the stochastic backgrounds at the two detector locations will be the same, while the noise are uncorrelated. Then, integrating the products of the signal for a sufficiently long time,[11] one can extract even a very small correlated signal from a much larger, but uncorrelated, noise. In can be shown that in this case the optimal signal-to-noise ratio is given by

$${\rm SNR} = \frac{3 H_0^2}{10 \pi^2} \left[2T \int_0^\infty df \, \gamma^2(f) \frac{\Omega_{\rm gw}^2(f)}{f^6 S_{h,1}(f) S_{h,2}(f)} \right]^{1/2} \,, \tag{95}$$

where $S_{h,1}(f)$ and $S_{h,2}(f)$ are the strain sensitivities of the detectors that we are correlating, and $\gamma(f)$, known as the overlap reduction function, is a

---

[10] Furthermore, in a single detector, a stochastic background manifest itself as just another source of noise, and, if one observe a noise curve higher than expected, it will be extremely difficult to tell whether one has observed a stochastic background of GW or a noise which has not been properly accounted for in the modelization of the detector.

[11] More precisely, we must also multiply the two signals by a filter function, whose optimal form depends on the frequency spectrum of the stochastic background that one is searching, so in practice a family of filters will be applied. For full details and derivations of the results of this section, see ref. [2].

function that suppresses the correlation at frequencies such that $2\pi f d \gg 1$, where d is the distance between the two detectors; its form is known esplicitly for a sphere-interferometer correlation.

At $f = 1$ kHz, two detectors within a few hundreds kms, such as VIRGO near Pisa and a sphere in the Gran Sasso laboratories, are still reasonably well correlated, and $\gamma(f) \sim 1$. Over the useful bandwidth $\Delta f \sim 200$ Hz of the sphere, eq. (95) can be approximated as

$$\mathrm{SNR} \simeq \frac{3H_0^2}{10\pi^2}\,(2T\Delta f)^{1/2}\,\frac{\Omega_{\rm gw}(f)}{f^3 S_{h,1}^{1/2}(f) S_{h,2}^{1/2}(f)}\,, \tag{96}$$

and, at $SNR = 1$, the minimum value of $h_0^2\Omega_{\rm gw}$ that can be detected, in a window Δf around a frequency f_0, correlating the outputs of the two detectors for a time T, is

$$\begin{aligned} h_0^2\Omega_{\rm gw}(f_0) \;\sim\; & 10^{-5}\left(\frac{f_0}{1\,\mathrm{kHz}}\right)^3 \left(\frac{S_{h,1}^{1/2}(f_0)}{3\times 10^{-23}\,\mathrm{Hz}^{-1/2}}\right)\left(\frac{S_{h,2}^{1/2}(f_0)}{3\times 10^{-23}\,\mathrm{Hz}^{-1/2}}\right) \\ & \times\left(\frac{200\,\mathrm{Hz}}{\Delta f}\right)^{1/2}\left(\frac{1\,\mathrm{yr}}{T}\right)^{1/2}. \end{aligned} \tag{97}$$

The conclusion that we can draw is the following:

> *both VIRGO and the sphere, used separately, in the 1 kHz region can reach only an uniteresting sensitivity to stochastic backgrounds, $h_0^2\Omega_{\rm gw} = O(1)$. Instead, a VIRGO-sphere correlation can reach a sensitivity $h_0^2\Omega_{\rm gw} = O(10^{-5})$.*

Such a sensitivity is quite interesting. First of all, it is about five orders of magnitude better then the present best direct measurement of stochastic backgrounds of GWs at $f = 1$ kHz [46], and three order of magnitude better than the best limit presently put by LIGO around 200 Hz [47]. Second, it starts to penetrate in the region allowed by the nucleosynthesis bound; at this level signals from early Universe cosmology can in principle be found. Firm predictions about cosmological backgrounds are at present possible only in rare cases (e.g., the stochastic background from standard inflationary model, which however is too low for our sensitivity), because they typically involve speculations about early Universe cosmology and/or the corresponding high-energy physics. Still, there are models that predict stochastic backgrounds of GWs that can saturate the nucelosynthesis bound, in the frequency range of interest for us (see ref. [2] for review). A sensitivity such as that given in eq. (97) will therefore allow us to penetrate into a region experimentally unknown and potentially very interesting.

6 Project Costs

The SFERA costs excluding infrastructure.

Item	Cost (kEURO)
Cryogenics	
Cryostat design	70
Cryostat construction	640
Pumps and vacuum	270
Dilution refrigerator unit	650
Gauges and sensors	60
Transfer tubes	50
Pre-cooling system	40
Consumables	40
Subtotal	1820
Suspension System	
Electronics	40
Mechanics	290
Subtotal	330
Read-out	
Electronics and transducers	140
Subtotal	140
Data Acquisition	
Acquisition hardware	100
Analysis software	30
Subtotal	130
Sphere	
Sphere CuAl 33 tons	350
Subtotal	350
Travel	
Travel 2006	20
Travel 2007	50
Travel 2008	50
Subtotal	120
Total	2890

7 Schedule

The SFERA schedule assuming initial funding starting in Janury 2006.The first science run is scheduled at the end of 2008.

Item	End date
Cryogenics	June 2007
Cryostat design	March 2006
Refrigerator design	May 2006
Construct cryostat	January 2007
Construct refrigerator	March 2007
Test Cryostat	April 2007
Test Refrigerator	April 2007
Final Assembling and test	June 2007
Suspension System	July 2007
Finite element modeling	April 2006
Suspension design	June 2006
Construction	January 2007
Room temperature tests	May 2007
Final assembling in the cryostat	July 2007
Data Acquisition	July 2007
Purchase and assemble hardware	February 2007
Acquisition software	January 2007
Assemble electronics	February 2007
Analysis software	June 2007
Sphere	October 2007
Construction and final machining	March 2007
Tests with PZTs at room-temp	May 2007
Mounting in the cryostat	July 2007
Test circulated cooling	August 2007
Cooling at 4K and tests with PZTs	September 2007
Cooling at ultralow temperature and tests	October 2007
Read-out	December 2007
Definition of the read-out	June 2007
Installation of a single read-out channel	December 2007
Commissioning	October 2008
Engineering run with one read-out channel	March 2008
Engineering run with six read-out channel	October 2008

8 The collaboration

The SFERA collaboration is open to the partecipation of all the interested people. The present collaboration includes:

- INFN: D. Babusci, R. Ballantini, M. Bassan, Z. Berezhiani, P. Carelli, G. Cavallari, F. Cavanna, A. Chincarini, E. Coccia, C. Cosmelli, S. D'Antonio, V. Fafone, G. Gemme, G. Giordano, A. Ianni, A. Marini, Y. Minenkov, I. Modena, A. Moleti, G.P. Murtas, O. Palamara, G.V. Pallottino, R. Parodi, G. Piano Mortari, G. Pagliaroli, G. Pizzella, L. Quintieri, A. Rocchi, F. Ronga, A. Scaramelli, R. Terenzi, G. Torrioli, R. Vaccarone, G. Vandoni, M. Visco
- University of Geneva: M. Maggiore, F. Dubath, S. Foffa, H. Sanctuary, R. Sturani
- University of Leiden: A. de Waard, G. Frossati, O. Usenko

A The TIGA configuration

In this appendix we give the relevant equations that describe the system of five quadrupolar modes of the sphere plus the six secondary resonators representing the resonant transducers in the TIGA configuration.

We begin by considering the five quadrupolar modes of the sphere, labeled by m, coupled to N resonant transducers, labeled by $j = 1, \ldots, N$, and for the moment we keep N arbitrary. It is convenient to use the real spherical harmonics $Y_m(\theta, \phi)$, defined by $Y_0 = Y_{20}$ and

$$\begin{aligned} Y_{1c} &= \frac{1}{\sqrt{2}}(Y_{2,-1} - Y_{2,+1})\,, \qquad Y_{1s} = \frac{i}{\sqrt{2}}(Y_{2,-1} + Y_{2,+1})\,, \\ Y_{2c} &= \frac{1}{\sqrt{2}}(Y_{2,-2} + Y_{2,+2})\,, \qquad Y_{2s} = \frac{i}{\sqrt{2}}(Y_{2,-2} - Y_{2,+2})\,. \end{aligned} \tag{98}$$

To keep the notation lighter, we denote by $\xi_m(t)$ the spheroidal modes $\xi_{nlm}(t)$ with $l = 2$ and n given (we are typically interested in the fundamental mode $n = 1$), in the real basis for the spherical harmonics. Similarly we denote simply by $a(r)$ and $b(r)$ the functions $a_{nl}(r)$ and $b_{nl}(r)$ with $l = 2$ and the given value of n. Then, using eqs. (7) and (13), the contribution to the displacement $\mathbf{u}(\mathbf{x}\,, t)$ due to the spheroidal modes with $l = 2$ and n given can be written as

$$\mathbf{u}(\mathbf{x}\,, t) = \sum_m \xi_m(t)\, [a(r)\hat{\mathbf{r}} + b(r)R\boldsymbol{\nabla}]\, Y_m(\theta, \phi)\,, \tag{99}$$

where m runs over the values $0, 1c, 1s, 2c, 2s$. We also denote the frequency ω^S_{n2} with the given value of n simply by ω_0. Finally, the amplitude of the transducers' oscillations in the radial direction are denoted by $\xi_{\mathrm{t},j}$ and their frequency by ω_{t} (we will then tune $\omega_{\mathrm{t}} = \omega_0$, for resonant transducers).

The Lagrangian describing this system of coupled oscillators is

$$L = \sum_m \left[\frac{1}{2}M\dot{\xi}_m^2 - \frac{1}{2}M\omega_0^2\xi_m^2\right] + \sum_j \left[\frac{1}{2}m_{\mathrm{t}}\dot{\xi}_{\mathrm{t},j}^2 - V(\xi_{\mathrm{t},j};\xi_m)\right]\,, \tag{100}$$

where $V(\xi_{\mathrm{t},j};\xi_m)$ is the interaction potential between the j-th transducer and the sphere. If the transducers are built so to sense the radial displacement of the sphere, the interaction potential is

$$V(\xi_{\mathrm{t},j};\xi_m) = \frac{1}{2}m_{\mathrm{t}}\omega_{\mathrm{t}}^2 q_j^2\,, \tag{101}$$

where q_j is the relative displacement between the j-th transducer and the surface of the sphere, in the radial direction. We denote by $\mathbf{x}_j$ the location of the j-th transducer. In spherical coordinates $\mathbf{x}_j$ has polar angles θ_j, ϕ_j, and we denote by $\hat{\mathbf{r}}_j$ the radial unit vector at $\mathbf{x}_j$. The relative displacement

q_j can be written using eq. (99),

$$\begin{aligned} q_j(t) &= \xi_{\mathrm{t},j}(t) - \hat{\mathbf{r}}_j \cdot \mathbf{u}(\mathbf{x}_j, t) \\ &= \xi_{\mathrm{t},j}(t) - a(R) \sum_m \xi_m(t) Y_m(\theta_j, \phi_j)\,, \end{aligned} \tag{102}$$

It is useful to introduce the notation $a(R) = a_{n2}(R) \equiv \alpha$, as well as

$$B_{mj} \equiv Y_m(\theta_j, \phi_j)\,. \tag{103}$$

Then

$$q_j(t) = \xi_{\mathrm{t},j}(t) - \alpha \sum_m B_{mj} \xi_m(t)\,. \tag{104}$$

In conclusion, the Lagrangian describing the interaction of the five modes ξ_m with the N transducers $\xi_{\mathrm{t},j}$ is

$$\begin{aligned} L &= \sum_m \left[\frac{1}{2} M \dot{\xi}_m^2 - \frac{1}{2} M \omega_0^2 \xi_m^2 \right] \qquad (105) \\ &+ \sum_j \left[\frac{1}{2} m_{\mathrm{t}} \dot{\xi}_{\mathrm{t},j}^2 - \frac{1}{2} m_{\mathrm{t}} \omega_{\mathrm{t}}^2 \left(\xi_{\mathrm{t},j} - \alpha \sum_m B_{mj} \xi_m \right)^2 \right], \end{aligned}$$

and from this we get immediately the equations of motion. We include external forces F_m acting on the ξ_m (which describe, e.g. the GW force or the Nyquist thermal force on the sphere) and external forces F_j acting on the transducer $\xi_{\mathrm{t},j}$. Then (making use of eq. (104) to eliminate $\xi_{\mathrm{t},j}$ in favor of q_j) the equations of motion are

$$\ddot{\xi}_m + \omega_0^2 \xi_m - \mu \omega_{\mathrm{t}}^2 \alpha \sum_j B_{mj} q_j = \frac{F_m}{M}\,, \tag{106}$$

$$\ddot{q}_j + \omega_{\mathrm{t}}^2 q_j + \alpha \sum_{m'} B_{m'j} \ddot{\xi}_{m'} = \frac{F_j}{m_{\mathrm{t}}}\,, \tag{107}$$

where $\mu = m_{\mathrm{t}}/M$. Actually, some sources of noise (e.g. fluctuations in the electric field of the capacitor made by the sphere and the transducer) are rather described by forces acting *between* the sphere and the transducer. To take them into account observe that, in the above equations, $-m_{\mathrm{t}}\omega_{\mathrm{t}}^2 q_j = -k_{\mathrm{t}} q_j$ is the elastic force between the transducer and the sphere, so the forces f_j that act between the sphere and the transducer can be included replacing $-k_{\mathrm{t}} q_j$ with $-k_{\mathrm{t}} q_j + f_j$. Therefore eqs. (106) and (107) become

$$\ddot{\xi}_m + \omega_0^2 \xi_m - \mu \omega_{\mathrm{t}}^2 \alpha \sum_j B_{mj} q_j = \frac{1}{M}(F_m - \alpha \sum_j B_{mj} f_j)\,, \tag{108}$$

$$\ddot{q}_j + \omega_{\mathrm{t}}^2 q_j + \alpha \sum_{m'} B_{m'j} \ddot{\xi}_{m'} = \frac{F_j + f_j}{m_{\mathrm{t}}}\,, \tag{109}$$

Dissipation can be introduced with the replacements $F_m \to F_m - \gamma_m \dot{\xi}_m$ and $f_j \to f_j - \gamma_j \dot{q}_j$. Experimentally, we measure the relative displacements q_j, for instance using capacitive transducers. With these outputs, we can form the five combinations

$$g_m(t) = \sum_j B_{mj} q_j(t) \,, \tag{110}$$

which are independent, if we have at least five transducers. Multiplying both sides of eq. (109) by B_{mj} and summing over j, we get

$$\ddot{g}_m + \omega_{\rm t}^2 g_m + \alpha \sum_{m'} \sum_j B_{mj} B_{m'j} \ddot{\xi}_{m'} = \frac{1}{m_{\rm t}} \sum_j B_{mj} (F_j + f_j) \,. \tag{111}$$

For a generic configuration of transducers, i.e. for B_{mj} generic, each $g_m(t)$ is therefore coupled to all five variables $\xi_{m'}(t)$. The advantage of the TIGA configuration is that it satisfies

$$\sum_j B_{mj} B_{m'j} = \frac{3}{2\pi} \delta_{mm'} \,, \tag{112}$$

and eqs. (108) and (111) become

$$\ddot{\xi}_m + \omega_0^2 \xi_m - (\mu \omega_{\rm t}^2 \alpha) g_m = \frac{1}{M} (F_m - \alpha \sum_j B_{mj} f_j) \,, \tag{113}$$

$$\ddot{g}_m + \omega_{\rm t}^2 g_m + \frac{3\alpha}{2\pi} \ddot{\xi}_m = \frac{1}{m_{\rm t}} \sum_j B_{mj} (F_j + f_j) \,. \tag{114}$$

The crucial point is that in this configuration each g_m couples only to the mode ξ_m with the same value of m. Therefore, our original system with ten coupled harmonic oscillators splits into five systems, each with only two coupled oscillators, (ξ_m, g_m). The variables g_m are called the "mode channels". The inclusion of all forces, such as Nyquist forces, acting on the system is necessary in order to compute the effect of noises on the system. If instead we want to compute the response of the system to GWs, we can simply set

$$\frac{F_m}{M} = \frac{1}{2} \chi R \ddot{h}_m \,, \tag{115}$$

as in eq. (35) (again, we suppress the label n in χ_n), and take $F_j = f_j = 0$. Equations (113) and (114) are then easily solved in Fourier space. Setting $\omega_{\rm t} = \omega_0$, we have

$$(-\omega^2 + \omega_0^2) \tilde{\xi}_m(\omega) - (\mu \omega_{\rm t}^2 \alpha) \tilde{g}_m(\omega) = -\frac{1}{2} \chi R \omega^2 \tilde{h}_m(\omega) \,, \tag{116}$$

$$(-\omega^2 + \omega_0^2) \tilde{g}_m(\omega) - \frac{3\alpha}{2\pi} \omega^2 \tilde{\xi}_m(\omega) = 0 \,, \tag{117}$$

which gives

$$\tilde{g}_m(\omega) = T(\omega)\tilde{h}_m(\omega)\,, \tag{118}$$

where the transfer function $T(\omega)$ is

$$\begin{aligned} T(\omega) &= -\left(\frac{3\alpha}{4\pi}\chi R\right)\frac{\omega^4}{(\omega^2-\omega_0^2)^2-\frac{3\alpha^2}{2\pi}\,\mu\,\omega_0^2\omega^2} \\ &\equiv -\left(\frac{3\alpha}{4\pi}\chi R\right)\frac{\omega^4}{(\omega^2-\omega_+^2)(\omega^2-\omega_-^2)}\,, \end{aligned} \tag{119}$$

In the limit $\mu = m_{\rm t}/M \ll 1$, we get

$$\omega_\pm^2 \simeq \omega_0^2\left[1 \pm \left(\frac{3\alpha^2\mu}{2\pi}\right)^{1/2}\right]. \tag{120}$$

Observe that this transfer function is the same for all g_m, independently of m. The five modes of the sphere ξ_m combine with the five mode channels g_m to produce two quintuplets, degenerate in frequency, at $\omega = \omega_\pm$, and the value of h_m is determined by the value of g_m with the same m. For each m, the relation between h_m and g_m is very similar to the relation between the variables ξ_0 and $\xi_{\rm t}$ of the system made by a cylindrical bar and its transducer. The simplicity of this result makes the TIGA arrangement particularly attractive.

Finally, observe that with the six transducer outputs we formed the five mode channels given by eq. (110). We still have the possibility of forming one more independent combination, that monitors the monopole mode $l = 0$ of the sphere. Recalling that the spherical harmonics Y_{00} is a constant, we see that the matrix $B_j \equiv Y_{00}(\theta_j, \phi_j)$, analogous to the matrices B_{mj} defined in eq. (103), is actually independent of j, so the monopole mode is simply

$$g_{00}(t) = \sum_j q_j(t)\,. \tag{121}$$

The monitoring of this mode can be used as a further veto that distinguishes GWs from noise. More ambitiously, the monopole mode is excited by scalar fields, such as those predicted in scalar-tensor generalizations of general relativity, and therefore the monopole mode can be used to search for scalar GWs.

B Equations of motion

The resonant antenna (mass m_1) and the secondary mass m_2 (with $m_2 \ll m_1$) form a system of two coupled harmonic oscillators (see fig. 26). The oscillators are designed to have (when *uncoupled*) almost equal resonant frequencies $\omega_1 \simeq \omega_2$. Mechanical dissipation is included in the model through a dissipation constant γ_i ($i = 1, 2$) from which the energy decay time constant $\tau_i = m_i/\gamma_i$, and mechanical quality factor $Q_i = \omega_i \tau_i$ can be derived.

The equations that describe the dynamics of the mechanical system alone can be derived from the Lagrangian function:

$$\mathcal{L}_m = \frac{1}{2} m_1 \dot{x}_1^2 + \frac{1}{2} m_2 \dot{x}_2^2 - \frac{1}{2} m_1 \omega_1^2 x_1^2 - \frac{1}{2} m_2 \omega_2^2 \left(x_2 - x_1\right)^2 \tag{122}$$

together with a Dissipative function [70]:

$$\mathcal{D}_m = \frac{1}{2} \frac{m_1 \dot{x}_1^2}{\tau_1} + \frac{1}{2} \frac{m_2 \left(\dot{x}_2 - \dot{x}_1\right)^2}{\tau_2} \tag{123}$$

To include in the model the dynamical interaction between the mechanical resonators and the transducer, while still keeping the equations as simple as possible, we shall make use of the fact that any configuration of the field inside the resonator can be expressed as the superposition of the electromagnetic normal modes [71]: $\vec{E}(\vec{r}, t) = (\epsilon_0)^{-1/2} \sum \mathcal{E}_n(t) \, \vec{E}_n(\vec{r})$, $\vec{H}(\vec{r}, t) = (\mu_0)^{-1/2} \sum \mathcal{H}_n(t) \, \vec{H}_n(\vec{r})$, with the time–dependendent amplitudes[12] $\mathcal{E}_n(t) \equiv (\epsilon_0)^{1/2} \int \vec{E} \cdot \vec{E}_n \, \mathrm{d}V$, $\mathcal{H}_n(t) \equiv (\mu_0)^{1/2} \int \vec{H} \cdot \vec{H}_n \, \mathrm{d}V$, and the orthonormality conditions $\int \vec{E}_n \cdot \vec{E}_m \, \mathrm{d}V = \int \vec{H}_n \cdot \vec{H}_m \, \mathrm{d}V = \delta_{nm}$.

We shall consider an experimental situation in which an external source at angular frequency ω excites the field in the cavity near one of its eigenfrequencies ω_a. In this case the field stored in the cavity essentially coincides with the eigenmode at frequency ω_a and we shall write: $\vec{E}(\vec{r}, t) \simeq (\epsilon_0)^{-1/2} \mathcal{E}(t) \, \vec{E}_0(\vec{r})$ and $\vec{H}(\vec{r}, t) \simeq (\mu_0)^{-1/2} \mathcal{H}(t) \, \vec{H}_0(\vec{r})$.

The time–dependent amplitudes of the electromagnetic field stored in the re–entrant cavity behave like a simple harmonic oscillator with resonant frequency ω_a and energy decay time τ. This harmonic oscillator can be described by e.m. terms in the Lagrangian and in the Dissipative function:

$$\mathcal{L}_{em} = \frac{1}{2\omega_a^2} \dot{\mathcal{H}}^2 - \frac{1}{2} \mathcal{H}^2 \tag{124}$$

$$\mathcal{D}_{em} = \frac{1}{2\tau\omega_a^2} \dot{\mathcal{H}}^2 \tag{125}$$

The *dynamical interaction* between the e.m. oscillator and the mechanical oscillators has to be included. In our model the transducer is coupled

---

[12] The choice of the normalization constants is such that $\mathcal{H}(t)$ and $\mathcal{E}(t)$ have the same dimension. The total energy of the field is given by $U = 1/2(\mathcal{H}^2 + \mathcal{E}^2)$.

to the secondary mass, so the interaction term will have the form [72, 73]:

$$\mathcal{L}_{int} = -\frac{1}{2} C \, (x_2 - x_1) \, \mathcal{H}^2 \tag{126}$$

The coupling constant C has dimensions [length]$^{-1}$.

The equations of motion of the three–coupled–oscillators system are easily derived as

$$\ddot{x}_1 + \frac{\dot{x}_1}{\tau_1} + \omega_1^2 x_1 - \frac{m_2}{m_1}\frac{\dot{\delta}}{\tau_2} - \frac{m_2}{m_1}\omega_2^2 \delta - \frac{1}{2m_1} C \, \mathcal{H}^2 = \frac{f_1}{m_1} \tag{127}$$

$$\ddot{\delta} + \frac{\dot{\delta}}{\tau_2} + \omega_2^2 \delta + \ddot{x}_1 + \frac{1}{2m_2} C \, \mathcal{H}^2 = \frac{f_2}{m_2} \tag{128}$$

$$\ddot{\mathcal{H}} + \frac{\dot{\mathcal{H}}}{\tau} + \omega_a^2 \mathcal{H} \, (1 + C \, \delta) = \omega_a^2 f_s \tag{129}$$

where $\delta = x_2 - x_1$.

The r.h.s. of the above equations account for possible external interactions (f_1 might describe the gravitational interaction coupled to the primary oscillator, f_2 might describe the gravitational interaction coupled to the secondary oscillator and f_s describes the external rf source at angular frequency ω_{rf}). For vanishing coupling constant, $C = 0$, we recover the equations of motion of the two coupled mechanical oscillators.

It is worth stressing again that whenever an interaction term is present in the third (e.m.) equation (the interaction term *must* be present if we want to have a signal from the transducer), terms of the same order of magnitude $\simeq C$ are present in the mechanical equations. From this we can conclude that the transducer plays an *active* role in determining the dynamics of the system. At least one dynamical variable, describing the state of the transducer, has to be coupled to some degree of freedom of the monitored system (in this case the e.m. field amplitude $\mathcal{H}$ is coupled to the positions $x_2 - x_1$ of the vibrating masses). The same variable appears in the equations of motion of the monitored system, and its contribution cannot, in general, be neglected.

The explicit form of the coupling coefficien C can be deduced from eq. (129). This equation describes a frequency modulated oscillator with time–varying resonant frequency $\omega^2(t) = \omega_a^2[1 + C \, \delta(t)]$. This term can be put in the following form:

$$\frac{\omega^2 - \omega_a^2}{\omega_a^2} \simeq 2\frac{\omega - \omega_a}{\omega_a} = C \, \delta \tag{130}$$

or

$$C = \frac{2}{\omega_a}\frac{\Delta \, \omega}{\Delta \, \delta} \tag{131}$$

The coupling coefficient depends only on the geometry of the transducer. In the present design $\omega_a/(2\pi) \simeq 5.5 \times 10^9$ Hz and $1/(2\pi) \, \Delta\omega/\Delta\delta \simeq -1.4 \times 10^{14}$ Hz/m, so that $C \simeq 5 \times 10^4$.

References

[1] K. S. Thorne, in *Three Hundred Years of Gravitation*, edited by S. W. Hawking and W. Israel (Cambridge University Press, Cambridge, 1987).

[2] M. Maggiore, Physics Reports **331** (2000) 283.

[3] *Fifth Edoardo Amaldi Conference on Gravitational Wave Experiments*, Classical Quant. Grav. **21** (5), (2004).

[4] P. Astone *et al.*, Europhysics Letters **16**, 231 (1991).

[5] `www.lnf.infn.it/esperimenti/rog`

[6] P. Astone *et al.*, Astropart. Phys. **7**, 231-243 (1997).

[7] `www.auriga.lnl.infn.it`

[8] M. Cerdonio *et al.*, Classical Quant. Grav. **14**, 1491 (1997).

[9] P. Falferi *et al.*, Appl. Phys. Lett. **82**, 931 (2003).

[10] AURIGA Collaboration, private communications.

[11] R. Forward, General Relativity Gravitation **2**, 149 (1971).

[12] N. Ashby and J. Dreitlein, Physical Review D **12**, 336 (1975).

[13] R. V. Wagoner and H. J. Paik, in *Proceedings of International Symposium on Experimental Gravitation, Pavia* (Roma Accademia Nazionale dei Lincei, Roma, 1976), pp. 257–265.

[14] C. Zhou and P. F. Michelson, Physical Review D **51**, 2517 (1995).

[15] E. Coccia, J. A. Lobo, and J. A. Ortega, Physical Review D **52**, 3735 (1995).

[16] J. A. Lobo, Physical Review D **52**, 591 (1995).

[17] E. Coccia, V. Fafone, and G. Frossati, in *First Edoardo Amaldi Conference on Gravitational Wave Experiments*, edited by E. Coccia, G. Pizzella, and F. Ronga (World Scientific Publishing Co., Singapore, 1995).

[18] G. Frossati, in *Proceedings of the International Conference on Gravitational Waves: Sources and Detectors* (World Scientific Publishing Co., Singapore, 1997).

[19] M. Bianchi *et al.*, Class. Quantum Grav. **13**, 2865 (1996).

[20] Stevenson, T. R. (1997). Physical Review D **56**, 564.

[21] M. Maggiore, *Gravitational Waves. Vol. I: Theory and Experiments.* Oxford University Press, to appear in 2006.

[22] Misner, C. W., Thorne, K. S. and Wheeler, J. A. (1973). *Gravitation*, Freeman, New York.

[23] W. W. Johnson and S. M. Merkowitz, Physical Review Letters **70**, 2367 (1993).

[24] S. M. Merkowitz and W. W. Johnson, Physical Review D **51**, 2546 (1995).

[25] S. M. Merkowitz and W. W. Johnson, Physical Review D **53**, 5377 (1996).

[26] J. A. Lobo and M. A. Serrano, Nuclear Physics B **S48**, 116 (1996).

[27] S. M. Merkowitz and W. W. Johnson, in *Proceedings of the OMNI-1 workshop* (World Scientific Publishing Co., Singapore, 1998).

[28] M. Cerdonio *et al.*, Physical Review Letters **71**, 4107 (1993).

[29] Y. Guersel and M. Tinto, Phys. Rev. D **40** (1989) 3884.

[30] A. de Waard, G. Frossati, in *Third Edoardo Amaldi Conference on Gravitational Wave Experiments*, edited by S. Meshkov (1999).

[31] O.D. Aguiar *et al.*, Classical Quant. Grav. **21** (5), S457-S463 (2004).

[32] A. Abramovici *et al.*, Science **256**, 325 (1992).

[33] C. M. Will, *Theory and Experiment in Gravitational Physics* (Cambridge University Press, Cambridge, 1993).

[34] T. Damour and A. M. Polyakov, Nuclear Physics B **423**, 532 (1994).

[35] V. Kalogera, R. Narayan, D.N. Spergel and J.H. Taylor, ApJ 556 (2001) 340.

[36] M. Burgay *et al.*, Nature 426 (2003) 531.

[37] Coccia, E., Dubath, F. and Maggiore, M. (2004). *Phys. Rev. D* **70**, 084010.

[38] R. C. Duncan and C. Thompson, Astrophys. J. **392** (1992) L9.

[39] C. Thompson and R. C. Duncan, Astrophys. J. **408** (1993) 194; *ibid.* **473** (1996) 322; Mon. Not. R. Astron. Soc. **275** (1995) 255.

[40] M. Ruderman, Nature **223** (1969) 597.

[41] G. F. Marranghello, C. A. Z. Vasconcellos and J. A. de Freitas Pacheco, Phys. Rev. D **66** (2002) 064027.

[42] K. Ioka, Mon. Not. R. Astron. Soc. **327** (2001) 639.

[43] A. Drago, G. Pagliara and Z. Berezhiani, arXiv:gr-qc/0405145.

[44] S.L. Shapiro and S.A. Teukolsky, "Black Holes, White Dwarfs and Neutron Stars", Wiley 1983. p. 12.

[45] Brady, P. R., Creighton, T., Cutler, C. and Schutz, B. F. (1998). *Phys. Rev. D* **57**, 2101.

[46] P. Astone et al., Astron. Astrophys. **351**, 811-814 (1999).

[47] Abbott et al., Phys. Rev. D **69** (2004) 122004.

[48] F. Dubath, M. A. Gasparini, S. Foffa, M. Maggiore and R. Sturani, Phys. Rev. D **???** (2005).

[49] An european company fabricating large propellers is LIPS, Drunen (The Netherlands).

[50] E. Coccia, V. Fafone, G. Frossati, J.A. Lobo and J.A. Ortega, Phys. Rev. D **57**, 2051-2060 (1998).

[51] G. Pizzella, Nuovo Cimento **2C**, 209 (1979).

[52] M. Bassan and G. Pizzella, Internal Report LNF-95/064(P).

[53] M. Bassan, Y. Minenkov, R. Simonetti, "*Proceedings of the VIRGO Conference*", F. Fidecaro and I. Ciufolini editors (World Scientific, Singapore, 1997).

[54] P. Astone *et al.*, Phys. Rev. Lett. **91**, 11 (2003)

[55] Y. Minenkov, J. Phys. D: Appl. Phys. **33**, 1134 (2000).

[56] P. Falferi, M. Bonaldi, M. Cerdonio, M. Mück, A. Vinante, G. A. Prodi and S. Vitale, J. Low Temp. Phys. **123**, 275 (2001)

[57] P. Carelli *et al.*, Appl. Phys. Lett. **72**, 115 (1998)

[58] M. Podt, M. J. van Duuren, A. W. Hamster, J. Flokstra and H. Rogalla, Appl. Phys. Lett. **75** 2316, (1999)

[59] P. Falferi *et al.*, Appl. Phys. Lett. **82**, 931 (2003)

[60] A. Vinante *et al.*, Appl. Phys. Lett. **79**, 2597 (2001)

[61] A. Vinante *et al.*, Physica C **368**, 176 (2002)

[62] N.P. Linthorne and D.G. Blair, Rev. Sci. Instrum. **63** (9) (1992) 4154.

[63] E.N. Ivanov, M.E. Tobar, P.J. Turner and D.G. Blair, Rev. Sci. Instrum. **64** (7) (1993) 1905.

[64] E.N. Ivanov, P.J. Turner and D.G. Blair, Rev. Sci. Instrum. **64** (11) (1993) 3191.

[65] M.E. Tobar and D.G. Blair, J. Phys. D: Appl. Phys. **26** (1993) 2276.

[66] M.E. Tobar and D.G. Blair, Rev. Sci. Instrum. **66** (4) (1995) 2751.

[67] J. J. Barroso et al., Class. Quant. Grav. **21** (2004) S1221.

[68] K. L. Ribeiro et al., Class. Quant. Grav. **21** (2004) S1225.

[69] E.N. Ivanov and M.E. Tobar, IEEE Trans. Freq. Contr. **45** (6) (1998) 1526.

[70] E.M. Lifshitz and L.P.Pitaevskii, *Statistical Physics* (Part I), 3^{rd} ed., Pergamon Press, (1980).

[71] J.C. Slater, *Microwave Electronics*, Van Nostrand, (1950).

[72] G. Goubau, *Electromagnetic waveguides and cavities*, Pergamon Press, (1961).

[73] R. Ballantini et al., Class. Quant. Grav. **20** (2003) 3505.

[74] J. H. Taylor, Rev. of Mod. Phys. **66**, 711 (1994).

[75] P. Astone, J. A. Lobo, and B. F. Schutz, Class. Quantum Grav. **11**, 2093 (1994).

[76] L. S. Finn, in *Proceedings of the OMNI-1 workshop* (World Scientific Publishing Co., Singapore, 1998).

[77] E. Coccia, in *Proceedings of the International Conference on Gravitational Waves: Sources and Detectors* (World Scientific Publishing Co., Singapore, 1998).

[78] E. Coccia and V. Fafone, Physics Letters A **213**, 16 (1996).

[79] G. M. Harry, T. R. Stevenson, and H. J. Paik, Physical Review D **54**, 2409 (1996).

[80] S. Vitale, M. Cerdonio, E. Coccia, and A. Ortolan, Physical Review D **55**, 1741 (1997).

[81] P. Astone, G. V. Pallottino, and G. Pizzella, Class. Quantum Grav. **14**, 2019-2030 (1997).

[82] L. S. Finn, Physical Review D **46**, 5236 (1992).

[83] T. Harada, T. Chiba, K. Nakao, and T. Nakamura, Physical Review D **55**, 2024 (1997).

[84] D. Dewey, Physical Review D **36**, 1577 (1987).

[85] B. F. Schutz, Nature **323**, 310 (1986).

[86] J. S. Bendat and A. G. Piersol, *Measurement and analysis of random data* (John Wiley & Sons, New York, 1966).

[87] P. F. Michelson, Monthly Notices of the Royal Astronomical Society **227**, 933 (1987).

[88] E. E. Flanagan, Physical Review D **48**, 2389 (1993).

[89] R. Brustein, M. Gasperini, M. Giovannini, and G. Veneziano, Physics Letters B **36**, 45 (1995).

[90] S. M. Merkowitz, Ph.D. thesis, Louisiana State University, 1995.

[91] S. M. Merkowitz (unpublished).

[92] E. Coccia *et al.*, Physics Letters A **219**, 263 (1996).

[93] G. Frossati, in *Proceedings of the OMNI-1 workshop* (World Scientific Publishing Co., Singapore, 1998).

[94] `www.minigrail.nl`

[95] `www.das.inpe.br/~graviton/`

[96] A. de Waard *et al.*, Classical Quant. Grav. **21** (5), S465S471 (2004).

[97] A. de Waard, Ph.D. thesis, Leiden University, 2003.

[98] L. Gottardi, Ph.D. thesis, Leiden University, 2004.

[99] J.P. Zendri, private communication.

[100] G. Frossati and E. Coccia, Cryogenics **35**, 9 (1994).

[101] E. Coccia, Rev. Sci. Instrum. **55**, 1980 (1984).

[102] S. Braccini *et al.*, Rev. Sci. Instrum. **67**, 2899 (1996).

[103] P. Astone *et al.*, Physical Review D **47**, 362 (1993).

[104] G. Pallottino and G. Pizzella, Nuovo Cimento **45 B**, 275 (1978).

[105] E. A. C. Cosmelli *et al.*, Nuovo Cimento **1 C**, 1979 (1978).

[106] S. Boughn *et al.*, Rev. Sci. Instrum. **61**, 1 (1990).

[107] C.A. Costa *et al.*, gr-qc/0312035.

[108] M. Cerdonio *et al.*, Phys. Rev. Lett. **87** , 031101 (2001).

[109] M. Bonaldi *et al.*, Physical Review D **68**, 102004 (2003).

[110] E. Coccia *et al.*, Nucl. Instr. and Meth. **A 355**, 624 (1995).

[111] P. Astone *et al.*, Phys. Rev. Lett. **84** , 1 (2000).

[112] P. Astone *et al.*, Phys. Lett. B **499** , 16-22 (2001).

[113] P. Astone *et al.*, Phys. Lett. B **540** , 179-184 (2002).

[114] C. Bernard *et al.*, Nuclear Physics B **93**, 242 (1984).

[115] G. Mazzitelli and M. A. Papa, in *Proceedings of the OMNI-1 workshop* (World Scientific Publishing Co., Singapore, 1998).

[116] R.M. Marinho Jr *et al.*, Class. Quantum Grav. **19**, 1955-1960 (2002).

[117] A. M. Grassi, G. Strini, and G. Tagliaferri, Journal of Applied Physics **51**, 948 (1980).

[118] G.D. van Albada *et al.*, Rev. Sci. Instrum. **71**, 1345 (2000).

[119] S. Bertolucci *et al.*, Nucl. Instrum. Meth. A **520**, 205-207 (2004).

[120] S. Bertolucci *et al.*, Classical Quant. Grav. **21** (5), S1197-S1202 (2004).